DYNAMIC 3D *IN VITRO* BONE METASTATIC TESTBEDS FOR PROSTATE AND BREAST CANCER

A Dissertation
Submitted to the Graduate Faculty
of the
North Dakota State University
of Agriculture and Applied Science

By

Haneesh Jasuja

In Partial Fulfillment of the Requirements
for the Degree of
DOCTOR OF PHILOSOPHY

Major Program:
Materials and Nanotechnology

January 2022

Fargo, North Dakota

North Dakota State University
Graduate School

Title

DYNAMIC 3D *IN VITRO* BONE METASTATIC TESTBEDS FOR PROSTATE AND BREAST CANCER

By

Haneesh Jasuja

The Supervisory Committee certifies that this ***disquisition*** complies with North Dakota State University's regulations and meets the accepted standards for the degree of

DOCTOR OF PHILOSOPHY

SUPERVISORY COMMITTEE:

Dr. Kalpana Katti
Chair

Dr. Dinesh Katti

Dr. Jiha Kim

Dr. Trung Le

Approved:

03/25/2022
Date

Dr. Erik Hobbie
Department Chair

ABSTRACT

Metastatic prostate cancer spreads preferentially to the bone, causing skeletal complications associated with significant morbidity and a poor prognosis, despite current therapeutic approaches. Increasing evidence suggests the synergistic role of biochemical and biophysical cues in cancer progression at metastases. However, the mechanism underlying the crosstalk between interstitial flow-induced mechanical stimuli and prostate cancer progression in the bone microenvironment remains poorly understood. To this end, we have developed 3D *in vitro* dynamic models of prostate cancer bone metastasis using perfusion bioreactor and horizontal flow bioreactor to delineate the role of flow-induced shear stress on prostate cancer progression and migration, respectively at metastases. Using a perfusion bioreactor, we observed changes in the expressions of MET biomarkers and the tumoroid morphologies of prostate cancer cells under dynamic culture. Evaluation of cell adhesion proteins indicated that the altered cancer cell morphologies resulted from the constant force pulling due to increased E-cadherin and FAK proteins under shear stress.

Using a horizontal flow bioreactor, we demonstrated that the percent cell migration rate of prostate cancer cells was increased in the presence of bone under dynamic conditions. The results showed that interstitial fluid flow did not alter the CXCR4 level, but bone upregulated CXCR4 levels, leading to increased MMP-9 levels. In addition, both $\alpha v\beta 3$ integrins and MMP-9 levels were upregulated by fluid flow conditions, contributing to an increased migration rate under dynamic conditions.

Breast cancer cells also tend to preferentially disseminate to bone and colonize within the remodeling bone site to cause bone metastases. We have previously developed a 3D *in vitro* breast cancer bone metastasis model using hMSCs and commercial breast cancer cells (MCF-7 and

MDAMB231), recapitulating late-stage breast cancer metastasis to bone. In the present study, we have validated our model using patient-derived breast cancer cell lines- NT013 and NT023, exhibiting hormone-positive and triple-negative characteristics, respectively that showed MET and formed tumors in the presence of bone. In addition, the results showed ET-1 (NT013) and DKK-1 (NT023) mediated stimulation and abrogation of the osteogenesis via Wnt/β catenin pathway, in line with our previous results with MCF-7 and MDAMB231 cell lines.

ACKNOWLEDGMENTS

There are many people who supported me through this journey. First and foremost, I want to thank my advisor, Dr. Kalpana Katti, and co-advisor, Dr. Dinesh Katti who continuously motivated me during my research work. I am thankful that they always gave me their precious feedback and advice. My Ph.D. journey would not have been possible without their endless support and inspiration. I want to express my sincere gratitude to my committee members – Dr. Jiha Kim, and Dr. Trung Bao Le for their valuable suggestions on my project. I also want to thank Dr. Anu Gaba for her contribution to my project. I am thankful to my previous year's senior Dr. Sumanta Kar for giving me a chance to help him in his research work. I also want to acknowledge my current lab mates and coworkers– Sibanwita, Sharad, Krishna, Faisal, Preetham, Shrinwanti, and Farid. I am thankful to our office staff – Milkha Singha and Ruth for helping graduate students like me.

I want to thank my mother who has taught me to be confident and fearless. I am grateful to my father who helped me to make wise choices and my brother who encouraged me to pursue my dreams. My wife has always been a support pillar to achieve the smallest and the biggest milestones in this journey. I am proud to have Arav as my son who already knows how to say 'Biofabrication' at the age of 2. I am grateful to all of you and the Almighty, without whom I couldn't have all the support and blessings. Thank you for being part of my wonderful journey, My Ph.D.

DEDICATION

Dedicated to the Almighty,

my loving parents, Arvind Jasuja and Indu Bala

my supportive parents-in-law, Subhash Taneja and Asha Taneja

my wife, Sakshi Taneja and

my son, Arav Jasuja.

TABLE OF CONTENTS

LIST OF TABLES

LIST OF FIGURES

LIST OF ABBREVIATIONS

2D.....Two-dimensional.

3D.....Three-dimensional.

ALP.....Alkaline Phosphate.

ARP2/3.....Actin-related Proteins-2/3.

ARS.....Alizarin Red S.

ATCC.....American Type Culture Collection.

BrCa.....Breast Cancer.

Chi/PgA.....Chitosan Polygalacturonic Acid.

CK1.....Casein Kinase 1.

CM.....Conditioned Medium.

COL I.....Collagen Type I.

DAPI.....4', 6-Diamidino-2-phenylindole.

DKK-1.....Dickkopf Homolog 1.

DMEM.....Dulbecco's Modified Eagle Medium.

ECM.....Extracellular Matrix.

ELISA.....Enzyme Linked Immunosorbent Assay.

EMEM.....Eagle's Minimum Essential Medium.

EMT.....Epithelial to Mesenchymal Transition.

ET-1.....Endothelin-1.

FBS.....Fetal Bovine Serum.

FGFR2.....Fibroblast Growth Factor Receptor 2.

FSG.....Fish Skin Gelatin.

FZD.....Frizzled.

GAPDH.....Glyceraldehyde 3-Phosphate Dehydrogenase.

GSK-3β .....Glycogen Synthase Kinase-3β.

HAP.....Hydroxyapatite.

HBCC.....Human Breast Cancer Cell.

HIF-1.....Hypoxia Inducible Factor 1.

LRP-5/6.....Low-density Lipoprotein Receptor-related Protein5/6.

M-CSF.....Macrophage Colony Stimulating Factor.

MET .....Mesenchymal to Epithelial Transition.

MMP-9.....Matrix Metalloproteinase 9.

MSCs.....Mesenchymal Stem Cells.

Na-MMT .....Sodium Montmorillonite.

OCN .....Osteocalcin.

OPG.....Osteoprotegerin.

PBS .....Phosphate Buffered Saline.

PCa.....Prostate Cancer.

PCL .....Polycaprolactone.

PCN.....Polymer-Clay Nanocomposite.

PCR.....Polymerase Chain Reaction.

PFA .....Paraformaldehyde.

PSA .....Prostate Specific Antigen.

RANKL.....Receptor Activator of Nuclear Factor Kappa B Ligand.

RUNX2 .....Runt Related Transcription Factor 2.

SC.....Sequential Culture.

SDF-1.....Stromal Cell Derived Factor-1.

SEM .....Scanning Electron Microscope.

STAT3.....Signal Transducer and Activator of Transcription 3.

TCPS.....Tissue Culture Polystyrene.

TGF-β.....Tumor Growth Factor- β.

UV.....Ultraviolet.

VEGF.....Vascular Endothelial Growth Factor.

1. GENERAL INTRODUCTION

Prostate and breast cancers are the most common bone metastasized cancers affecting mostly men and women, respectively. It is estimated that 248,530 cases of prostate cancer and 281,550 cases of invasive breast cancer diagnosed at the end of 2021 in the United States [1]. With the advancement in therapy for primary staged cancers, the overall 5-year survival rate has now improved. However, in the case of metastasis, where cancer cells migrate to distant organs, the overall survival rate is still poor, thus defined as the major cause of morbidity in patients with metastasized prostate and breast cancer cells. Both prostate and breast cancer cells have the propensity to metastasize to the liver, brain, lungs, and bone, however, bone metastasis occurs in about 80% of patients with advanced-stage prostate and breast cancers [2]. Once established in the bone, these cancer cells majorly affect the bone remodeling process and lead to severe skeletal-related defects such as bone fracture, spinal cord compression, hypercalcemia, and pain. Lesions caused by these cancer cells after bone metastasis can be categorized into osteoblastic (excess bone formation) and osteoclastic (excess bone resorption) [3].

1.1. Bone metastatic cascade

Paget's "seed and soil" theory suggested that the propensity of cancer cells (seeds) toward distant organs (soil) depends upon the tropism and molecular characteristics of cancer cells [4]. In addition, Ewing in 1928 suggested the metastasis of cancer cells depends upon interconnected vasculature between primary sites and distant organ [5]. In the case of prostate and breast cancer, the preferential site of metastasis is the bone [6]. Bone metastasis is a complex multistep cascade that requires metastasizing cancer cells to undergo a series of cytoskeletal and genetic variations. Thus, metastatic tumor cells often have high incidences of genetic mutations or epigenetic modifications.

The metastatic cascade initiates with cytoskeletal changes in cancer cells, where epithelial cancer cells expressing high E-cadherin protein levels undergo epithelial to mesenchymal transition (EMT) and acquire mesenchymal-like characteristics with increased expressions of vimentin, twist, snail, and snug proteins. Subsequently, angiogenesis at the primary site of the tumor due to increased expression of vascular endothelial growth factor (VEGF) allows motile cancer cells to leave their site of origin and enter the blood or lymphatic circulation, the process well-known as intravasation. Among the tumor cells that enter the bloodstream or lymphatic circulation, only 0.001-0.02% of cells manage to evade the immune system and combat fluid shear stress by continuous circulating fluid flows. The tumor cells that eventually survived in the vasculature, extravasate to the distant organ, where they again adapt themselves in a new microenvironment and create a compatible niche by initiating a reciprocal vicious cycle between themselves and the bone microenvironment. In addition, cancer cells undergo a series of genetic and morphological transformations and acquire epithelial characteristics by mesenchymal to epithelial transition (MET).

1.2. Current therapies for bone metastasized prostate and breast cancer

There are no current therapies available to cure prostate and breast cancer, metastasized to bone. The drug therapies available currently are utilized to reduce pain and improve bone stability. The drug therapeutics include bisphosphonates and Denosumab [7]. Bisphosphonates are inorganic pyrophosphate (PPi), a compound containing two phosphate groups linked by esterification that are capable of inhibiting bone calcification by binding to hydroxyapatite crystals, thus regulating bone mineralization by suppressing the bone resorption [8]. Previously, bisphosphonates were administered for the alleviation of bone-related side effects such as pain and treatment-related osteoporosis [7,8]. Afterward, bisphosphonates were used for late-stage breast

cancers to reduce the risk of breast cancer spreading to the bone [9,10]. However, there are some adverse effects commonly seen in breast cancer patients administrating bisphosphonates such as bone, joint, or muscle pain, nausea, vomiting, and diarrhea [9].

In September 2011, denosumab (Prolia) was approved by the Food and Drug Administration (FDA) which is a human monoclonal antibody, targeting the receptor activator of the nuclear factor-kappa-B ligand (RANKL). RANKL regulates osteoclast formation and binds with RANK receptors to stimulate osteoclastic bone resorption. Denosumab acts by inhibiting the differentiation and activation of osteoclasts, thus decreasing bone resorption and increasing bone density [10].

Similarly, for metastasized prostate cancer, bone-directed therapies such as bisphosphonates (zoledronic acid) or denosumab are the only drug therapeutics available currently. Androgen deprivation therapy (ADT) is also sometimes useful for treating late-stage prostate cancers. However, this treatment becomes less effective over time because of resistance developed by prostate cancer against ADT, resulting from conversion into a more aggressive form [11]. In addition, radiation therapy and chemotherapy are also useful as adjuvant therapies for prostate and breast cancer treatment [11-13]. Currently used chemotherapy drugs that are used to treat prostate cancer are Mitoxantrone, Cabazitaxel, Docetaxel, and Estramustine [14]. However, due to the lack of effective treatments available to treat prostate cancer and breast cancer patients in their advanced stage, there is a critical need for a better understanding of the prostate and breast cancer metastasis process in detail to develop effective treatments.

1.3. Bone metastatic *in vitro* models

The tissue engineering approach is widely used for developing bone metastatic models because of its ease of model and convenient manipulation characteristics. In addition, natural

materials or components employed for tissue-engineered constructs may possess properties similar to bone minerals such as hydroxyapatite, calcium, phosphorous, etc. However, natural materials have some limitations such as weak mechanical properties and early degradation. To overcome such limitations, synthetic materials are frequently used in combination with natural components.

Currently, monoculture/ 2D culture is widely used to grow cell populations and cell-based assays however, 2D culture fails to recapitulate the dynamic interactions between cancer cells and the bone microenvironment, due to a lack of realistic complexity. Hence, 3D *in vitro* models have gained considerable attention, owing to their crosstalk between cells and the surrounding milieu. There are considerable efforts have been made to recapitulate the bone metastatic behavior of prostate and breast cancer cells using 3D *in vitro* disease models. However, such models were developed using the co-culture technique. A study showed the co-culturing of osteoblasts and prostate cancer cells in a 3D model of collagen and hydroxyapatite to mimic the late stage of prostate cancer [15](. Another study showed encapsulation of prostate cancer cells and stromal cells in hydrogel microspheres to create a 3D co-culture model [16]. A chitosan-alginate-based model has also been developed to understand the interactions between lymphocytes and prostate cancer cells [17]. Silk-based models were also developed to mimic cell invasion of prostate cancer cells to the bone [18]. Similar models were developed for breast cancer, for instance, the 3D silk fibroin-based model was developed by Talukdar & Kundu to understand interactions between osteoblasts and breast cancer cells [19]. Similarly, silk fibroin scaffold models were developed to study the efficacy of cytotoxic drugs [20]. A 3D printed approach was also utilized to develop a co-culture model of breast cancer cells and osteoblasts to study drug resistance of cancer cells against 5-Fluorouracil [21].

1.4. Nanoclay-based scaffolds

Previously, nanoclays have been incorporated into tissue-engineered constructs for the enhancement of their mechanical properties [22]. Later, our research group utilized montmorillonite (MMT) clay for the enhancement of osteoconductivity of polymer-clay nanocomposites (PCN) by mixing hydroxyapatite (HAP) with modified MMT. Katti and the group have also explained the reason for the improved mechanical properties of PCN scaffolds by introducing a novel theory called "Altered Phase theory". The theory suggests that the volume of the polymer is significantly influenced by molecular-level interactions between the components of PCNs that lead to an alteration in the crystallinity of the polymer in the altered zone around the intercalated clay particles [23]. Initially, our research group modified MMT clay by intercalating unnatural amino acids (5-amino valeric acid) between clay nanosheets, resulting in increased d-spacing between clay sheets [24]. Further, these modifications were characterized by our research group using X-ray diffraction (XRD) and Fourier Transform Infrared (FTIR) spectroscopy experiments [25]. After introducing HAP in modified MMT clay, our research group has observed that hydroxyapatite was mineralized into biomineralized apatite molecules [26]. Next, our research group evaluated the biocompatibility of nanoclay containing scaffolds using bone marrow-derived human mesenchymal stem cells (hMSCs) and observed that hMSCs undergo osteoblastic differentiation in the absence of external osteogenic supplements. Our research group has confirmed the osteogenic differentiation of hMSCs by determining the calcium to phosphorous (Ca/P) ratio of small vesicles released by hMSCs into the extracellular matrix [27]. The results showed that the Ca/P ratio of these vesicles was nearly equivalent to the stoichiometric ratio of inorganic minerals of bone that indicates mature bone formation on the scaffold surface. In addition, our research group has also observed that the Ca/P ratio of some vesicles was lower than

the stoichiometric ratio, suggesting immature or new bone formation at the same time, which ultimately recapitulates the remodeling of bone. Later, our group examined bone-related biomarkers (RUNX2, ALP, and OCN) to further confirm the osteogenic differentiation of hMSCs on nanoclay-based scaffolds [28].

1.5. Role of body fluids in generating mechanical cues

Various body fluids such as blood, lymph, and interstitial fluid are attributed to the biophysical cues. These fluid types exhibit different flow rates and flow types inside the body. For instance, in lymph nodes, flow is mostly laminar and has low velocities due to high viscosity. In contrast, blood has higher flow velocities and even possesses much higher density due to the presence of blood cells and other factors. The reason is cardiac pumping which also provides pulsative behavior to the blood flow, resulting in generating high amplitude and turbulent flow in the arteries while in veins flow is mostly laminar. Thus, biophysical cues by body fluids may differ based on fluid viscosity, vessel type, and organ type. It is estimated that cancer cells experience a shear rate in the lymphatic system and large arteries equivalent to ~10/s and ~1,000/s, respectively. A study showed velocity, shear rate, and stress values in different vessel segments [29] (**Table 1.1**)

Table 1.1. Body fluid parameters across different blood vessels.

Vessel segments	**Velocity (mm/s)**	**Shear Rate (1/s)**	**Shear Stress (dyne/cm^2)**
Arterial vessel	1.95 ± 0.57	1921 ± 417	65.5 ± 16.0
Post-arterial capillaries	1.10 ± 0.31	1150 ± 409	34.6 ± 12.3
Intermediate capillaries	0.66 ± 0.18	484 ± 126	14.2 ± 4.7
Sinusoidal capillaries	0.23 ± 0.22	119 ± 114	2.9 ± 2.7

Interstitial fluid exists in the stroma of tissue, whose normal function is to carry nutrients and oxygen into the stromal space and transport waste metabolites away from cells. In a healthy person, the body maintains homeostasis of fluid in-flow and out-flow in the interstitial space

however, in the cancerous stage, the amount of fluid is significantly increased and poorly drained, resulting in increased interstitial pressure in the tumor [30]. The increased pressure generates a steep pressure gradient between the tumor and the surrounding healthy tissue, resulting in higher interstitial fluid flow into the healthy tissue and lymph nodes [31]. Several 2D and 3D *in vitro* models have been developed to study the effect of fluid flow on cancer progression. Table 1.2 summarizes the results of some *in vitro* dynamic models developed for various cancer types.

Table 1.2. *In vitro* dynamic cancer models for studying the role of interstitial fluid flow

Cell types	**Flow shear (dyne/cm^2)/velocity (μm/s) values**	**Experimental setup**	**Outcomes**	**References**
Epithelial ovarian cancer	0.5-1.5 dyne/cm^2	Microfluidic chamber	Fluid flow induces stress fibers, resulting in elongation of cells	[32]
Osteosarcoma cells, oral squamous carcinoma, chondrosarcoma	12 dyne/cm^2	Monolayer exposed to fluid flow	High shear stress induces cell arrest	[33]
Melanoma, Breast carcinoma	0.2 μm/s	Tissue culture inserts with radial flow chamber	Increased cell invasion under fluid flow	[34]
Melanoma	0.5 μm/s	Tissue culture inserts with radial flow chamber	Increased cell invasion under fluid flow	[35]
Rat astrocytoma, human glioma	0.7 μm/s	Tissue culture inserts with radial flow chamber	Flow increased glioma invasion mediated via CXCR4 activation	[36]

1.6. Organization of this dissertation

This dissertation is organized into different chapters as follows:

Chapter 1. In this chapter, we discussed a brief background of prostate and breast cancer bone metastasis cascade and current drug treatment for bone metastatic prostate and breast cancer. Then, we discussed the need for 3D *in vitro* models for understanding the late-stage bone metastasis of prostate and breast cancer. Next, we described a brief description of the nano-clay based 3D *in vitro* model developed by our group. At last, we discussed the role of fluid shear stress and physiological values of fluid velocities and shear stresses.

Chapter 2. This chapter describes the design of the perfusion bioreactor and the role of fluid flow in the progression of prostate cancer cells metastasis to bone.

Chapter 3. This chapter describes the design of the horizontal flow bioreactor and the role of fluid flow in the migration of prostate cancer cells at their extravasation step

Chapter 4. This chapter describes the validation of a 3D in vitro breast cancer metastatic model with patient-derived cells.

Chapter 5. This chapter describes the details of experimental work generated to correlate computational fluid dynamics (CFD) results

Chapter 6. This chapter summarizes the major conclusions of the research work presented in this dissertation.

Chapter 7. This chapter provides the future directions for the research in this field.

2. PERFUSION BIOREACTOR ENABLED FLUID-DERIVED SHEAR STRESS CONDITIONS FOR NOVEL BONE METASTATIC PROSTATE CANCER TESTBED[1]

This chapter describes the role of fluid flow in the progression of prostate cancer to bone. The contents of this chapter have been published in H Jasuja, S Kar, DR Katti, KS Katti; "Perfusion bioreactor enabled fluid-derived shear stress conditions for novel bone metastatic prostate cancer testbed", Biofabrication, Volume 13, Number 3, 035004

2.1. Introduction

Prostate cancer is the second foremost cause of cancer-associated morbidity among men in the United States, as reported by the National Cancer Institute (NCI). As per the NCI report, 90% of the deaths result from bone metastasis of prostate cancer resulting in pathological bone fracture or other skeletal-related cascades [37, 38]. Paget's "seed and soil" theory on cancer metastasis, first proposed in 1889, stated that cancer cells (seeds) have a high propensity toward specific microenvironments that act as soil for their growth [39]. It is evident that bone provides the most suitable microenvironment for prostate cancer metastasis than other metastatic sites such as the liver, distant lymph nodes, and the thorax [2, 3]. Current drug treatments for prostate cancer bone metastasis include denosumab and bisphosphonates to reduce bone fragility that ultimately delays metastasis and increase patients' survival rate [40]. However, there is no permanent curative treatment available after the colonization of the prostate tumor into a bone niche.

[1]This chapter was co-authored by Haneesh Jasuja, Sumanta Kar, D.R. Katti. And K.S. Katti. Haneesh Jasuja had primary responsibility for preparing samples, conducting all tests, and drafting this chapter. Kalpana Katti and Dinesh Katti directed the research orientation and revised this chapter.

It is understood that the cause of failure of novel drugs for bone metastatic cancer treatment is a poor understanding of the complex interactions between prostate cancer and bone microenvironment and the unavailability of appropriate drug testing models. In recent years, tissue-engineered three-dimensional (3D) models have gained immense interest over two-dimensional (2D) testing models due to their ability to mimic disease phenotype in regards to cell morphology, cell-cell, and cell-extracellular matrix (ECM) interactions [41], [42].

Several attempts have been made to develop 3D *in vitro* bone metastatic prostate cancer models [18, 43-46]. Although not duplicating the accurate bone niche at the metastasis condition, these attempts provide useful information. These studies include efforts that evaluate drug efficacies using co-cultures of prostate cancer cells and osteoblasts [47] and the role of substrate stiffness on cancer cells [48].

However, the studies mentioned above primarily focus on elucidating the critical role of biochemical factors that enhance bone metastasis of prostate cancer but do not accurately recapitulate the bone niche behavior. In our prior studies, we have developed a nanoclay based tissue-engineered scaffold [24, 49, 50] that mimics the remodeling bone niche [25, 27] to which cancer cells possess the propensity to migrate. We have studied the critical role of amino acid modified-biomineralized-hydroxyapatite-nanoclays or '*in-situ* hydroxyapatite clay' (*in-situ* HAPClay) onto our scaffold system that contributes potentially to enhancing the mechanical properties of the scaffold and induces hMSCs osteogenesis [25]. Besides enabling a vesicular delivery [27], the nanoclay-based scaffold possesses high compressible modulus (~2.5 MPa) with high porosity (~ 86.1%), as well as different pore sizes ranging from 10-30 μm to 100-300 μm, which are necessary for hard tissue growth. In previous studies, we have also shown that sequential seeding of prostate cancer cells to tissue-engineered bone results in tumor formation at the bone

site [51]. In addition, detailed gene expression analyses of the generated tumors elucidated that the prostate cancer tumors in bone are in the mesenchymal to epithelial transition stage [52, 53]. Similar studies were also conducted for breast cancer bone metastasis [54, 55]. The bone scaffold model can thus be used as a testbed to evaluate behaviors of phenotypically different prostate cancer cells at the bone site [56].

Numerous tissue engineering studies suggested the critical role of biomechanical cues in bone development and bone remodeling process [57]. Studies have also indicated the significant role of dynamic flow in the osteoblast phenotype expression [58]. Moreover, studies of various cancer cell types have shown modulation in cancer cell response due to shear stress. The role of drug efficacies is also influenced by shear stresses on the cancer cells [59]. Though it is well known that fluid-derived shear stress maintains bone homeostasis and its growth, its role in facilitating prostate cancer metastasis to bone is largely unknown.

Hence, in the present study, we decided to implement dynamic conditions in our existing *in vitro* 3D cell culturing system to investigate the influence of fluid-derived shear stress on bone metastasis of prostate cancer. In this study, we have fabricated a perfusion bioreactor system to understand the effect of fluid-derived shear stress on hMSCs proliferation, differentiation, and morphological changes during the first part of the study. Later, we focused our experiments on investigating changes in morphology and gene/protein expressions of sequentially cultured prostate cancer cells under dynamic conditions. We have also compared our results with static culturing of the prostate cancer bone metastasis tumoroids. Finally, our study emphasized delineating the underlying cause of morphological changes in prostate cancer cells.

2.2. Materials and methods

2.2.1. PCL *in situ* HAP scaffold fabrication

The scaffolds were fabricated according to the protocol described previously [24, 50, 60-62]. Briefly, sodium montmorillonite (Na-MMT) clay is modified with 5-aminovaleric acid to increase the d-spacing of Na-MMT clay. Further, hydroxyapatite (HAP), an essential component for biomineralization, is grown on nanoclay galleries of modified clay to make *in-situ* HAP Clay. Finally, polycaprolactone (PCL) is added to the 10 wt% *in-situ* HAP Clay to make a composite mixture, and employing the freeze-drying method, PCL/*in-situ* HAP Clay scaffolds were prepared. The dimensions of cylindrical scaffolds used during the experiments are 12 mm in diameter and 3 mm in thickness (figure 1(c)).

2.2.2. Perfusion bioreactor design

The bioreactor system consists of cylindrical chambers, separators, and chamber holders fabricated from crosslinked Polymethyl-methacrylate (PMMA) polymer using a Formlabs Form 2 3D Printer (figure 2.1(a)). Each chamber is designed with a dimension of 17 mm in diameter and 45 mm in height that supports four independent scaffold samples separated by double O-ring shaped separators (figure 2.1(b), 2.1(d)). During experiments, scaffolds in the bioreactor chambers are streamed continuously from bottom to top with the culture medium at a flow rate of 0.2 mL/min. The culture medium is kept in reservoir bottles made up of borosilicate glass. These reservoirs are coupled with chambers and a flow regulating pump (IPC Digital Peristaltic Pump, Ismatec) via a tubing system (Peroxide-Cured Silicone, ID 1.42 mm, Ismatec). The bioreactor chambers and culture medium reservoirs are placed inside the incubator (37°C, 5% CO_2, high moisture).

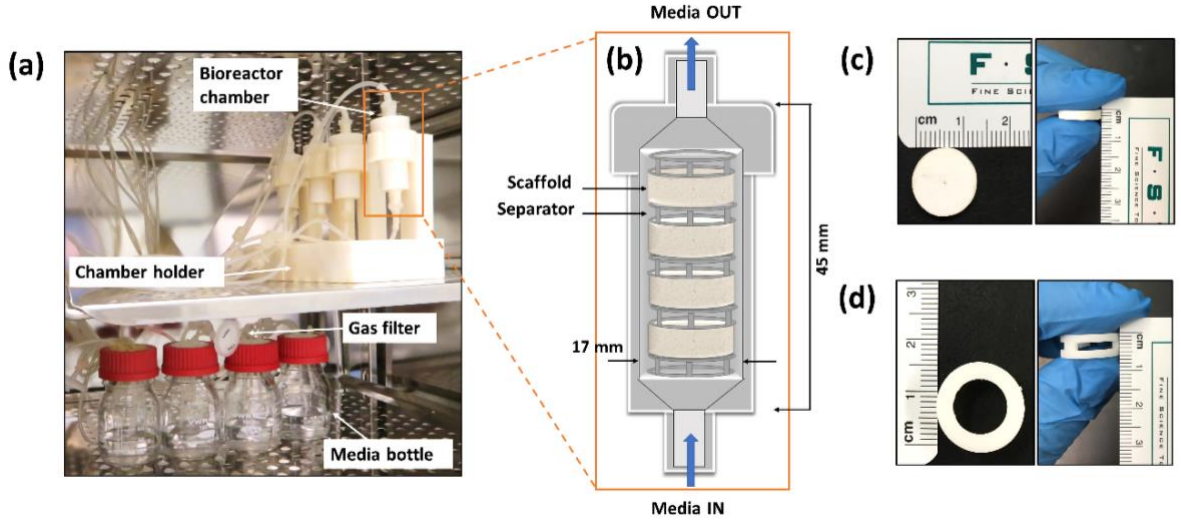

Figure 2.1. Perfusion bioreactor setup inside an incubator at 37°C, 5% CO_2, and high moisture content. (a) Bioreactor chambers at the top and media reservoir bottles at the bottom of the incubator. (b) Schematic representation of the bioreactor chamber accommodating four scaffolds separated by double O-ring separators. (c) Dimensions of PCL/*in situ* HAP clay scaffold (left) top view (right) side view (d) Double O-ring separator (left) top view (right) side view.

2.2.3. Fluid shear stress calculations

To estimate the fluid-induced shear stress at the wall of scaffold pores, we assumed a cylindrical pore model approximation for the scaffold pores [63] and calculated wall shear stress (τ_w) using the equation

$$\tau_w = \frac{8\mu\tilde{\vartheta}}{d}$$

where μ is the viscosity of media (DMEM), which is reported to be 0.78 mPa.s at 37°C [64], d is the diameter of scaffold pores, which is estimated to be a range of 10μm- 300μm based on previous studies [50], and $\tilde{\vartheta}$ is the average fluid velocity, calculated using the following equation

$$\tilde{\vartheta} = \frac{Q}{\emptyset\pi(D/2)^2}$$

where Q is the flow rate of medium, ∅ is scaffold porosity, which is estimated to be 0.86 based on previous studies [50], and D is a scaffold diameter of 12 mm.

Hence, the calculated average velocity is 34.3 µm/s, and wall shear stresses range between 0.7 mPa and 21.4 mPa.

2.2.4. Cells lines and media

Human mesenchymal stem cells (hMSCs) were purchased from Lonza (PT-2501) and grown in MSCGM Bulletkit medium (Lonza, PT-3001). Human prostate cancer cell (PCa) lines MDAPCa2b (ATCC® CRL-2422™) and PC3 (ATCC® CRL-1435™) were purchased from American Type Culture Collection (ATCC). MDAPCa2b cells were maintained in a medium comprised of 80% BRFF-HPC1 (AthenaES, 0403), 20% fetal bovine serum (FBS) (ATCC, 30-2020), and 1% Penicillin-Streptomycin (Pen-Strep) antibiotic (Gibco). PC3 cells were cultured in 90% F-12K Medium (Kaighn's Modification of Ham's F-12 Medium) containing 2 mM L-glutamine and 1500 mg/L sodium bicarbonate (ATCC, 30-2004), 10% FBS (ATCC, 30-2020), and 1% Pen-Strep antibiotic (Gibco) solution. The cell cultures were maintained at 37°C and 5% CO_2 in a humidified incubator.

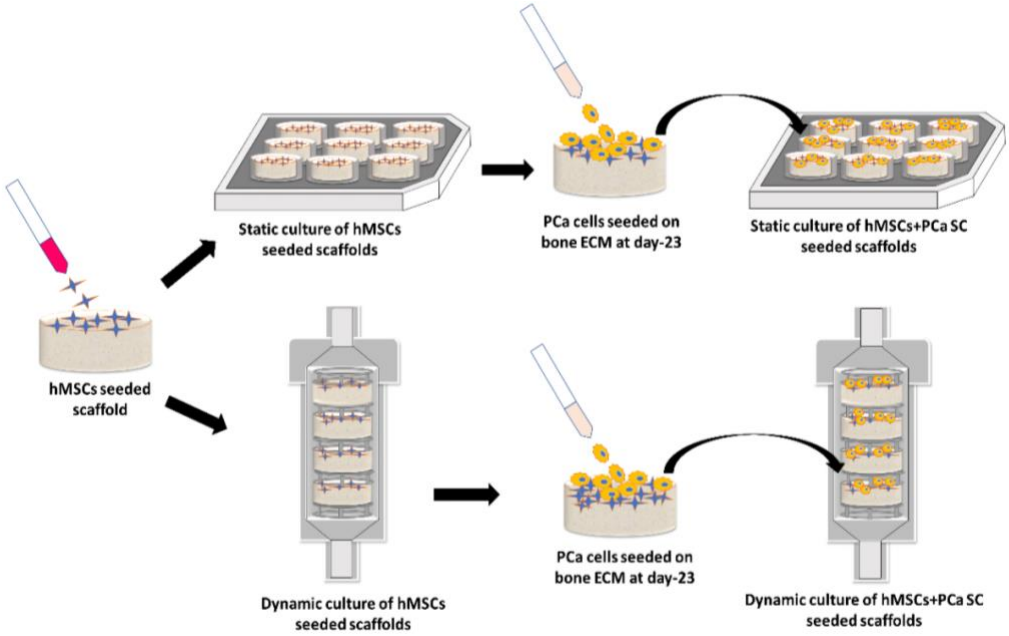

Figure 2.2. Schematic showing steps of cell seeding under static and dynamic culture conditions.

2.2.5. Cell seeding and culturing

PCL/HAP Clay scaffolds were sterilized under Ultraviolet (UV) light for 45 min and kept in 70% ethanol for 12 hr. Further, scaffolds were washed twice with phosphate-buffered saline (PBS) and immersed in the hMSCs culture medium for 4 hours before cell seeding. For both static and dynamic cultures, hMSCs and PCa cells were seeded on each scaffold at a density of $5x10^5$ cells and $1x10^5$ cells, respectively, in a sequential manner. A schematic describing the sequential culturing of cells in static and dynamic culture is shown in figure 2.2. Initially, hMSCs were seeded on each scaffold at a density of $5x10^5$ cells and were incubated at 37°C and 5% CO_2 for 24 hours. These samples were considered as day 0. Next, we transferred half of the hMSCs seeded scaffolds into the bioreactor followed by culturing for 23 days for osteogenic differentiation and mineralized bone formation. After 23 days, we took scaffolds out of the bioreactor and seeded the PCa cells on top of the osteogenically differentiated hMSCs at a density of $1x10^5$ cells. We utilized a 1:1 ratio of hMSCs and PCa media for sequential cultures. Similar steps were followed for seeding PCa on static scaffolds. The media was changed every 2 days for static culture and every 3 days for dynamic culture.

2.2.6. DNA quantification

Cell proliferation assay was performed by measuring DNA content according to the manufacturer's protocol (AccuBlue® Broad Range dsDNA Quantitation Kits). Briefly, the cell-seeded scaffolds were washed twice with PBS and were digested with the addition of 500 µl of cell lysis TE buffer (10mM Tris, 1mM EDTA, 0.1% Triton X-100, proteinase K) per scaffold followed by three freeze-thaw cycles at -80°C and 37°C. Further, the supernatants were drawn off after centrifugation at 12000x g. Finally, 10 µl of each diluted sample was mixed with 200 µl of working solution and incubated for 30 minutes at room temperature (RT) in the dark. The

fluorescence was measured at 350 nm excitation/ 460 nm emission using a fluorescence microplate reader (BioTek).

2.2.7. Cell cycle analysis by flow cytometry

The cells were harvested from the scaffold by adding 500 µl of TrypLE™ Express Enzyme (1X), phenol red, for 10 mins. The recovered cells were centrifuged at 600x g for 5 minutes in a 5 ml PBS solution to obtain a cell pellet. The cell pellet was then suspended in 500 µl of PBS, and the suspension was added dropwise into 4.5ml of ice-cold 70% ethanol while gentle vortexing. Next, we incubated the cell containing 70% ethanol solution at 4°C for 1 hour to fix the cells. After that, fixed cells were washed in fresh PBS, and the cell pellet was resuspended in 500 µl of the propidium iodide (PI) staining buffer containing RNAse (Cell Signaling, #4087). The cell suspension was incubated in the dark at RT for 30 minutes and then analyzed by a BD Accuri C6 flow cytometer using the fluorescence emission 585/42 nm.

2.2.8. Scanning electron microscopy (SEM)

Scaffolds recovered at different time points from static and dynamic cultures were washed twice in PBS and fixed in 2.5% glutaraldehyde overnight at 4°C. Following this, the scaffolds were washed three times with PBS to remove the fixing reagent. Further, the samples were dehydrated with a series of ethanol concentrations (30%, 50%, 70%, 90%, and 100%) and dried using hexamethyldisilazane. The dried samples were coated with gold and mounted on SEM stubs to analyze under a scanning electron microscope (JEOL JSM-6490LV).

2.2.9. Immunofluorescence staining

Scaffolds from static and dynamic cultures were washed in PBS and fixed in 4% paraformaldehyde for 45 mins at room temperature. The samples were then PBS washed 3 times for 5 minutes each and permeabilized with 0.2% Triton-X 100 for 5 minutes. Next, the samples

were blocked with 0.2% fish skin gelatin blocking buffer (0.2% FSG and 0.02% Tween20 in PBS) for 1 hour at room temperature and then incubated with the primary antibody in blocking buffer overnight at 4°C. The details of primary antibodies and their dilutions are given in Table 2.1. All primary antibodies were further labeled with their corresponding secondary antibodies (Alexa Flour 488 (Green) or Alexa Flour 647 (Red)) at a dilution of 1:200 and incubated in the dark at RT for 45 mins. Finally, cell nuclei were counterstained with 4,6- diamidino-2-phenylindole (DAPI), and immunofluorescence images were taken under Zeiss Axio Observer Z1 LSM 700 confocal microscope.

Table 2.1. List of primary antibodies used during immunostaining experiments.

Primary antibody	Batch number	Dilution
RUNX2	ab23981	1:1000
OCN	ab13421	1:100
E-Cadherin	ab40772	1:500
Vimentin	ab8978	1:100

2.2.10. ALP activity

The ALP activity was determined according to the manufacturer's protocol (Biovision). Briefly, p-nitrophenyl phosphate (pNPP) standards were prepared using different concentrations ranging from 0-20 nmol. The samples were treated with lysate buffer (Biovision) followed by three freeze-thaw cycles. Next, 70 µl of each sample was mixed with 50 µl of pNPP solution and incubated for 60 min at RT in the dark. Finally, the reaction was stopped using 20 µl of 3N NaOH solution, and sample absorbance was measured at 405 nm. The data were normalized to total DNA content.

2.2.11. Gene expression studies

RNA was isolated using TRIzol reagent and purified using the Direct-zol RNA miniprep Kit (Zymo Research) following standard procedure. Then isolated RNA was reverse transcribed

to cDNA using M-MLV reverse transcriptase and random primers (Promega). SYBR Green PCR master mix was utilized for real-time PCR by using reaction conditions of 2 min at 50°C, 10 min at 95°C as holding stage and 40 cycles of 15 sec at 95°C and 1 min at 60°C for cycling stage. The expressions of ALP, RUNX2, OCN, E-cadherin, and vimentin were analyzed and normalized to the mean of the glyceraldehyde-3-phosphate dehydrogenase (GAPDH) gene expression. The relative fold change was calculated using the 2^-(ΔΔCT) relative comparative method. The details of primer sequences are provided in Table 2.2.

Table 2.2. The sequence of forward and reverse primers used for the RT-PCR experiments.

Gene	Forward primer	Reverse primer
GAPDH	5'-CAT CTT CTT TTG CGT CGC CA-3'	5'-TTA AAA GCA GCC CTG GTG ACC-3'
ALP	5'-TCA ACA CCA ACG TGG CTA AG -3'	5'-CAC AAT GCC CAC AGA TTT CC-3'
RUNX2	5'-GTC TCA CTG CCT CTC ACT TG-3'	5'-CAC ACA TCT CCT CCC TTC TG-3'
OCN	5'-GTG ACG AGT TGG CTG ACC-3'	5'-TGG AGA GGA GCA GAA CTG G-3'
E-Cadherin	5'- AAG TGA CCG ATG ATG AT -3'	5'-CTC TGT CCA TCT CAG CG-3'
Vimentin	5'-GAG AAC TTT GCC GTT GAA GC-3'	5'- TCC AGC AGC TTC CTG TAG GT-3'

2.2.12. Western blot

Cells were extracted from scaffolds and then harvested in RIPA buffer (Thermo Fisher) to generate cell lysates. Following this, the total protein concentration was estimated using the Bradford assay (Thermo Fisher). For E-cadherin and vimentin, proteins were resolved through SDS-10 % polyacrylamide gel. For FAK protein analysis, 100 µl cell lysates were immunoprecipitated overnight with 30 µl of G-Sepharose beads (pre-incubated with species-specific primary antibody). Beads were washed three times with PBS and loaded on SDS-10% polyacrylamide gel. The separated proteins were transferred to 0.2 µm PVDF membrane (Thermo

scientific) and blocked for 1 hour at RT with blocking buffer (5% bovine serum albumin (BSA), 0.05% Tween-20) (Alfa Aesar). Then, the membrane was incubated with primary antibodies at 4°C overnight. The membrane was washed with Tris-buffered saline, 0.1% Tween 20 (TBST), and incubated for 1 hour at RT with horseradish peroxidase (HRP)-conjugated secondary antibody at 1:5000 dilution. Finally, blots were visualized using enhanced chemiluminescence, and the densitometric analyses were carried out using Image J software (NIH, USA). First, we normalized the proteins of interest and controls to their β-actins. Next, controls were subtracted from proteins of interest to evaluate the actual protein levels of cancer cells. The details of primary antibodies of E-cadherin, vimentin, FAK, and p (Y397)-FAK is given in Table 2.3.

Table 2.3. List of primary antibodies used during western blot.

Primary antibody	Batch number	Dilution
E-Cadherin	ab40772	1:1000
Vimentin	ab8978	1:5000
FAK	ab131435	1:2000
p-FAK (Tyr397)	ab81298	1:1000

2.2.13. Statistical analysis

Data were analyzed using ANOVA, followed by Tukey's post hoc analysis using GraphPad Prism v7.04. Software. The data were presented as the mean value of triplicates ± standard deviation. Differences between the two groups were considered statistically significant when probability, $p<0.05$.

2.3. Results

2.3.1. Increased hMSCs proliferation and morphological variations in dynamic samples due to continuous flow perfusion

The hMSCs were cultured on scaffolds for 23 days under both static and dynamic conditions. The DNA quantification data showed a steady increase in DNA content in both

culturing conditions over time. However, the amount of DNA was significantly higher in dynamic samples than in static, as shown in figure 2.3(a). The day-10 data of dynamically cultivated samples showed an increase in DNA content, with some statistical significance (* $p<0.05$) w.r.t day-10 static samples indicating the onset of shear forces effect by perfusion flow on hMSCs proliferation. In contrast, day-23 dynamic samples exhibited a large increase in cell proliferation at statistically significant levels ($$ $p<0.01$). It is to be noted that the differences in proliferation rate are assumed to arise from differences in cell cycle distribution of cells cultured under different culturing conditions. Thus, we evaluated the cell cycles of hMSCs on day-10 and day-23 using flow cytometry. The results showed that hMSCs on day-23 exhibited a significant increase in G0/G1 ($^{\phi}p < 0.05$ and $$$ $p<0.001$ in static and dynamic cultures, respectively) and a decrease in G2/M phases ($^{\phi\phi}p < 0.05$ and $$$ $p<0.001$ in static and dynamic cultures, respectively) compared to their day-10 samples. We also observed a significant change in G0/G1 (42.22 ± 0.76 % in static and 51.10 ± 1.36 % in dynamic samples ** $p<0.01$) and G2/M phases (18.74 ± 1.72 % in static and 9.77 ± 1.19 %, in dynamic samples ** $p<0.01$) of day-23 static and dynamic cultures. In comparison, no significant change was observed in the S phase (39.02 ± 0.45 % in static and 39.00 ± 0.22 % in dynamic samples) (figure 2.3(d)). Next, we determined the morphological variations in hMSCs under dynamic conditions. We observed that hMSCs under static culture appeared to form cell agglutinates, whereas dynamic samples exhibited a directional alignment of cells with broad and flattened morphology (figure 2.3(b)).

2.3.2. Enhanced hMSCs osteogenic differentiation of dynamic samples assessed by changes in expression levels

It is well established that the assessment of the gene expression level of osteogenic markers such as Alkaline phosphatase (ALP), Runt-related transcription factor 2 (RUNX2), and

Osteocalcin (OCN) is a key factor in determining the osteogenic potential of hMSCs. We have previously reported that ALP and RUNX2 expressions are increased at day-4, day-8, and day-16 w.r.t day-1 in static culture and then downregulated over time [55]. In this study, we determined the gene expression of early and late-stage osteogenesis markers at day-10 and day-23, respectively w.r.t day-0 control, to evaluate the effect of static and dynamic conditions on hMSCs differentiation rate. Various studies have suggested the critical role of RUNX2, ALP, and OCN in hMSCs differentiation. It was shown that elevated expression levels of RUNX2 and ALP indicate the onset of hMSCs osteogenetic differentiation. In contrast, upregulation in OCN levels and downregulation in early-stage osteomimetic genes (RUNX2, ALP) are hallmarks of the cell maturation [65-68]. We observed a similar trend in our studies in both culturing conditions. However, the gene expression data in figures 2.3(e), 2.3(f), and 2.3(g) indicate that both early phase (RUNX2, ALP) and late phase (OCN) markers were significantly affected by the continuous flow perfusion. The hMSCs cultured under dynamic conditions exhibited elevated mRNA levels of ALP, RUNX2, and OCN on day 10, which is significantly high (***$p<0.001$, **$p<0.01$, and * $p<0.05$, respectively) compared to static samples. On day 23, we observed that the ALP mRNA level of dynamically cultured hMSCs was significantly lower ($ $p<0.05$) than the static sample, while no significant changes were observed in the RUNX2 level. On the contrary, OCN expression was significantly higher ($$$ $p<0.001$) compared to the static sample.

We further validated the gene expression results with additional experiments. The ALP enzyme expressed on the cell surface, entrapped in matrix vesicles during the early development of the bone, promotes bone mineralization by increasing the inorganic phosphate concentration [69]. Interestingly, ALP activity results correspond well to the gene expression results (figure 2.3(c)). Next, we performed immunostaining experiments to confirm RUNX2 and OCN protein

levels over time. We observed a noticeable decrease in the staining intensity of RUNX2 while a steady increase in OCN immunostaining on day-23 in both culturing conditions compared to day-10. On comparing dynamic and static immunostaining data of RUNX2 and OCN, we observed that the immunostaining results are in good agreement with gene expression results (figure 2.3 (h)).

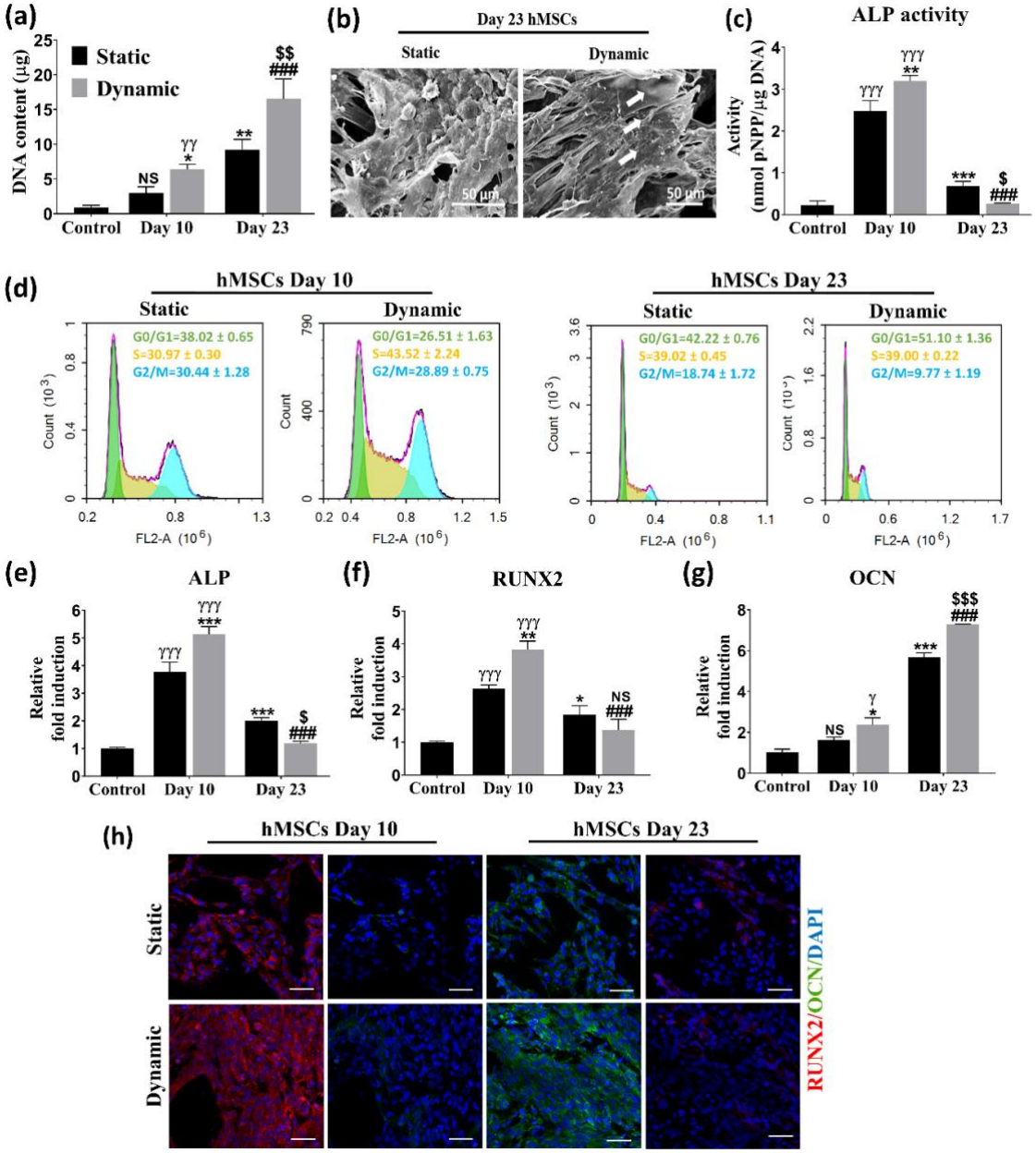

Figure 2.3. The proliferation and osteogenic differentiation of hMSCs grown on scaffolds under static vs. dynamic culture. (a) DNA content of static and dynamic samples on day-10 and day-23. (b) SEM showing hMSCs morphology and distribution on day-23. Arrows indicate the orientation of hMSCs. Scale bars: 50µm (c) ALP activity determined on day-10 and day-23. (d) Cell cycle analysis by flow cytometry representing G0/G1, S, and G2/M phases. (e) (f) (g) RT-PCR analysis (h) Immunostaining on day-10 and day-23. The high-intensity level shows upregulation of proteins and vice-versa. Scale bars: 50µm. $\gamma p < 0.05$, $\gamma\gamma p < 0.01$, and $\gamma\gamma\gamma p < 0.001$ indicate a significant difference between day-0 and day-10 static samples and between day-0 and day-10 dynamic samples. $*p < 0.05$, $**p < 0.01$, and $***p < 0.001$ indicate a significant difference between day-10 static and day-10 dynamic samples and between day-10 static and day-23 static samples. $\$ p < 0.05$, $\$\$ p < 0.01$, and $\$\$\$ p < 0.001$ indicate a significant difference between day-23 static and day-23 dynamic samples. $\# p < 0.05$, $\#\# p < 0.01$, and $\#\#\# p < 0.001$ indicate a significant difference between day-10 dynamic and day-23 dynamic samples. Error bars indicate standard deviation (SD).

2.3.3. Fluid-derived shear stress promotes morphological and mRNA alterations in MDAPCa2b and PC3 sequential cultures

In our previous studies, we endeavored to recapitulate two bone metastatic prostate tumor models, using sequential culturing of osteogenic differentiated hMSCs with two different prostate cancer cell lines. The MDAPCa2b and PC3 cells were grown on the bone mineralized nanoclay-polymer scaffold to evaluate the complex metastatic cascades of androgen-dependent and androgen-independent prostate cancer cell lines, respectively [52, 70]. It is evident that prostate cancer metastasizes to the bone niche through the mesenchymal to epithelial (MET) transition [71]. Studies suggest that during MET, vimentin, which is abundantly expressed in mesenchymal cells, downregulates, while E-cadherin plays a critical role in cell-cell adhesion in epithelial cells and upregulates [72, 73]. Our studies also confirmed the upregulation of E-cadherin and downregulation of vimentin mRNA after sequential culturing of PCa cells at day (23+5), day (23+10), and day (23+15) in static culture, indicating the occurrence of MET [52, 53]. However, to investigate the role of continuous fluid flow-induced shear stress on MET markers and prostate cancer cell morphology, we further analyzed gene/protein expressions of MET specific markers and correlated the results with SEM data. In this study, we evaluated the growth of PCa cells for an extended period; thus, we considered day (23+10) and day (23+20) as time points for comparison studies. We determined the gene expression of E-cadherin and vimentin at day (23+10) and day (23+20) of both sequential cultures (SC) under dynamic conditions and compared our results with the static data set. It is noteworthy to mention that we considered TCPS grown PC3 and MDAPCa2b cells as internal controls for hMSCs+PC3 SC and hMSCs+MDAPCa 2b SC, respectively. We noticed a significant (** $p<0.01$) increase in the E-cadherin expressions at day (23+10) in dynamic samples of hMSCs+MDAPCa2b SC and hMSCs+PC3 SC compared to their

static samples. Subsequently, on the day (23+20), we observed highly significant ($$$ $p<0.001$) upregulation in E-cadherin expressions in the dynamic samples of hMSCs+MDAPCa2b SC and hMSCs+PC3 SC in comparison to their static samples, indicating strong cell-cell interactions overtime under dynamic conditions (figure 2.4(a), 2.5(a)). In contrast, we did not find any change in vimentin expression in MDAPCa2b SC samples, but we observed significant changes ($$ $p<0.01$) in vimentin expression of the day (23+20) hMSCs+PC3 SC dynamic samples compared to their static samples (figure 2.5 (b)). Further, we validated our observations by evaluating their protein levels. As we observed significant changes in gene expression of E-cadherin and vimentin at day (23+20) in both SC, we decided to investigate their protein levels w.r.t hMSCs day (23+20) control to evaluate actual protein levels in PCa cells. We did not find any expression of E-cadherin in control samples; however, E-cadherin levels were significantly upregulated in dynamic samples of MDAPCa2b SC and PC3 SC compared to their static samples ($^{\phi\phi}p<0.01$ and $^{\phi}p<0.05$, respectively) (figure 2.4(c), 2.5(d)). On the contrary, vimentin levels were insignificantly changed in MDAPCa2b SC samples after deducting the contribution of control samples (figure 2.4(d)). Nonetheless, vimentin levels of PC3 SC dynamic samples showed a significant ($^{\phi\phi}p<0.01$) decrease compared to static samples after subtracting from their control samples (figure 2.5(e)). The blots and graphs with actual relative intensities of controls and SC samples normalized to β-actin. Next, we confirmed the immunostaining intensities of E-cadherin and vimentin at day (23+20) of both SC. We observed intense staining of E-cadherin in both SC dynamic samples compared to their static samples (figure 2.4(e), 2.5(f)). We also observed colonization of E-cadherin stained PC3 cells in hMSCs+PC3 SC dynamic samples, while E-cadherin stained PC3 cells in their static samples were loosely aggregated (figure 2.5(f)).

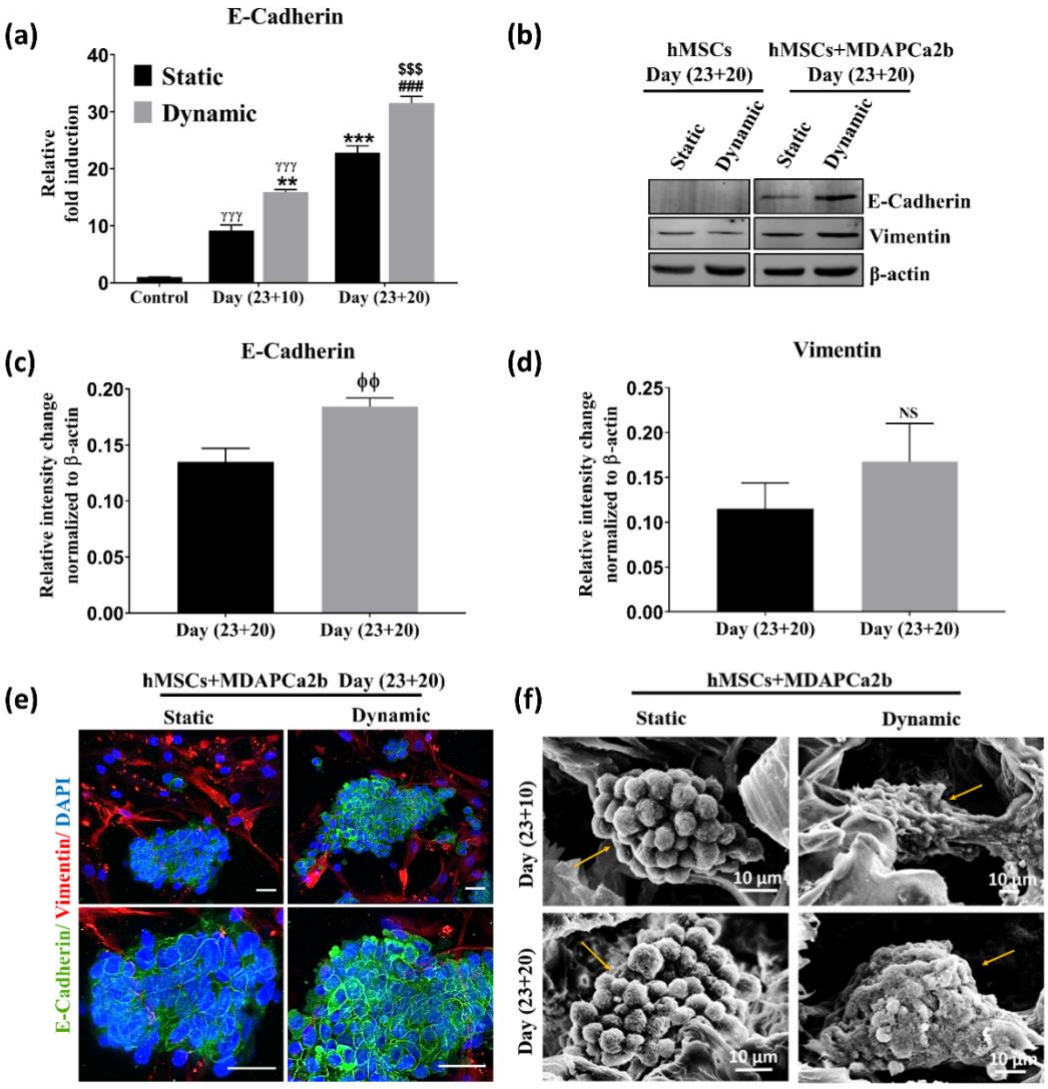

Figure 2.4. Biomarkers of MDAPCa2b prostate cancer cells representing mesenchymal to epithelial (MET) transition under static vs. dynamic culture. (a) RT-PCR analysis for E-Cadherin. $\gamma p < 0.05$, $\gamma\gamma p < 0.01$, and $\gamma\gamma\gamma p < 0.001$ indicate a significant difference between day-0 and day-10 static samples and between day-0 and day-10 dynamic samples. $^{**}p < 0.01$, and $^{***}p < 0.001$ indicate a significant difference between day (23+10) static and day (23+10) dynamic samples and between day (23+10) static and day (23+20) static samples, respectively. $\#\#\#p < 0.001$ indicates a significant difference between day (23+10) dynamic and day (23+20) dynamic samples. $\$\$\$p < 0.001$ indicates a significant difference between day (23+20) static and day (23+20) dynamic samples. Error bars indicate SD. (b) Protein expressions of E Cadherin and Vimentin were assessed by western blotting. (c-d) Quantification of E-Cadherin and Vimentin protein levels. $\phi p < 0.05$, $\phi\phi p < 0.01$, and $\phi\phi\phi p < 0.001$ indicate a significant difference between day (23+20) static and day (23+20) dynamic samples. (e) Representative immunofluorescence staining at day (23+20). Scale bars: 40µm (c) SEM micrographs of hMSCs+MDAPCa2b sequential culture. Arrows indicate a group of cells. Scale bars: 10µm

We also performed SEM analysis that showed the formation of tumoroid-like structures of MDAPCA2b prostate cancer cells under both culturing conditions. We observed that MDAPCa2b prostate cancer cells at day (23+10) under static conditions exhibited nearly round morphology that appeared to be fused to form a multilayered mass. On the day (23+20), we did not observe morphological variations; however, we found that the observed tumors are larger. On the other hand, dynamic MDAPCa2b prostate cancer cells appeared to form a highly compact morphology at day (23+10) that further grouped at day (23+20) into a cell mass with no distinct boundaries as shown in figure 2.4(f). Furthermore, we observed disorganized cell aggregates of PC3 prostate cancer cells in static culture on day (23+10) that appeared to form a complex network on the scaffold surface on day (23+20). In contrast, PC3 cancer cells under dynamic conditions exhibited cell colonization at day (23+10) and day (23+20), as shown in figure 2.5(g).

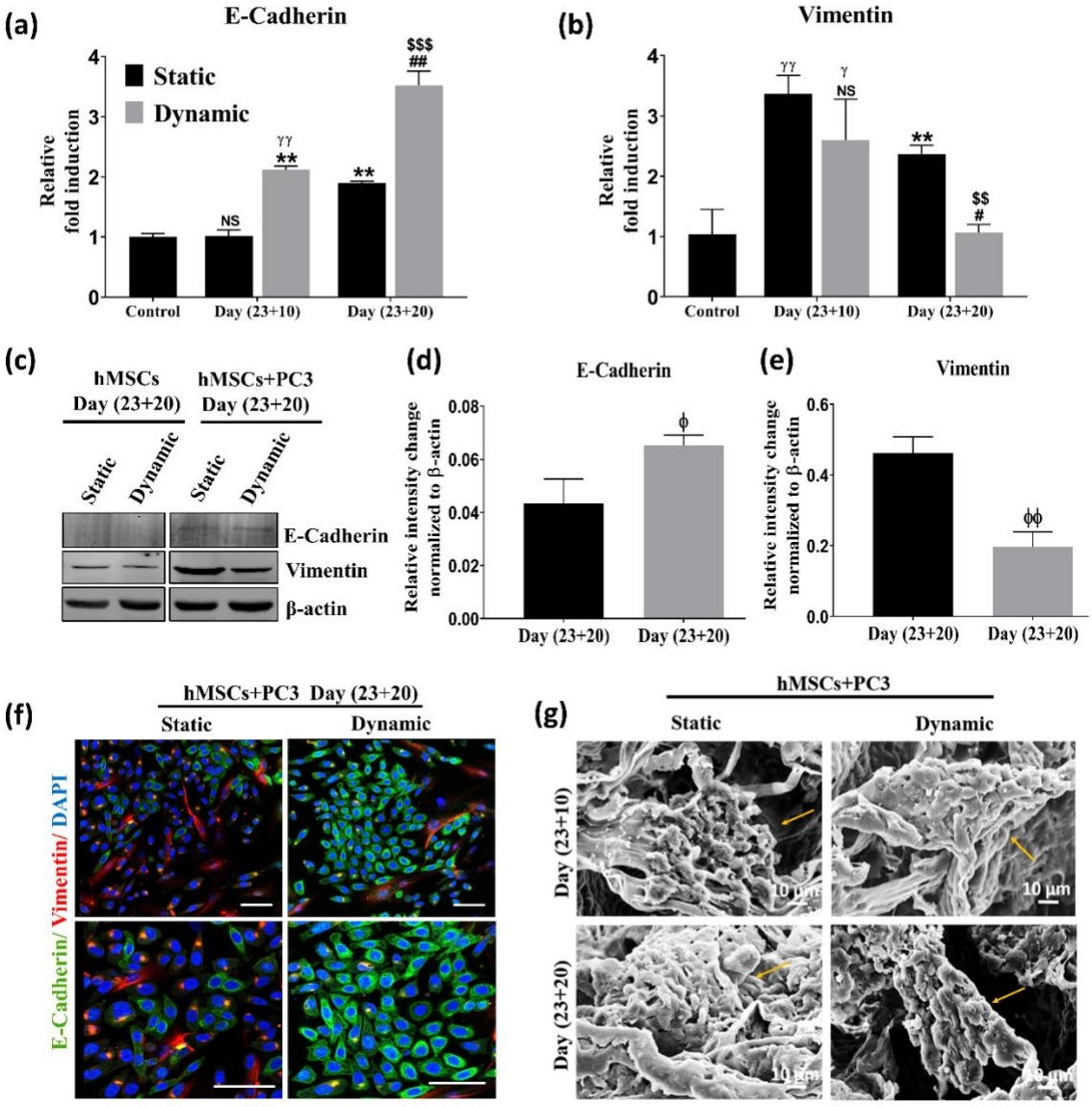

Figure 2.5. Biomarkers of PC3 prostate cancer cells representing mesenchymal to epithelial (MET) transition under static vs. dynamic culture. (a-b) RT-PCR analysis for E-cadherin and Vimentin gene expressions at day (23+10) and day (23+20). $^{\gamma}p< 0.05$, $^{\gamma\gamma}p < 0.01$, and $^{\gamma\gamma\gamma}p < 0.001$ indicate a significant difference between day-0 and day-10 static samples and between day-0 and day-10 dynamic samples. $^{**}p < 0.01$ indicates a significant difference between day (23+10) static and day (23+10) dynamic samples and between day (23+10) static and day (23+20) static samples. $^{\#\#}p < 0.01$ indicates a significant difference between day (23+10) dynamic and day (23+20) dynamic samples. $^{\$\$}p < 0.01$ and $^{\$\$\$}p < 0.001$ indicate a significant difference between day (23+20) static and day (23+20) dynamic samples. Error bars indicate SD. (c) Protein expressions of E Cadherin and Vimentin were assessed by western blotting. (d-e) Quantification of E-Cadherin and Vimentin protein levels of samples normalized to β-actin after control subtraction. $^{\phi}p < 0.05$, $^{\phi\phi}p < 0.01$, and $^{\phi\phi\phi}p < 0.001$ indicate a significant difference between day (23+20) static and day (23+20) dynamic samples (f) Representative immunofluorescence staining for MET biomarkers E-Cadherin (Green), Vimentin (Red) and DAPI for staining nucleus (Blue) at day (23+20). Low magnification images (top), high magnification images (bottom). Scale bars: 30µm (g) SEM micrographs of hMSCs+PC3 sequential culture at day (23+10) and (23+20) of static (left) and dynamic (right) samples. Arrows indicate a group of cells. Scale bars: 10µm.

2.3.4. FAK/E-cadherin crosstalk influences cancer cell morphology

Previously, we observed an increase in E-cadherin expression over time in both MDAPCa2b SC and PC3 SC, indicating increased cell-cell interaction. It is well-documented that integrins play a critical role in cell-matrix interaction and regulates via several focal adhesion (FA) proteins such as Focal Adhesion Kinase (FAK), vinculin, paxillin, p130 Cas, Elmo-DOCK complexes, and Rac proteins [74]. These focal adhesion proteins also regulate cell-cytoskeleton integrity via crosslinking with actin filaments. The other end of these cytoskeleton filaments is linked to adherent junctions [75]. Thus, it can be noted that established crosstalk exists between integrin-based focal adhesions and adherent junctions that maintain cell morphology. We hypothesized that under continuous fluid-derived shear stress, both adherent junction and integrins junction simultaneously experienced a force at their ends that triggers intracellular tension in the cytoskeleton filaments. To minimize such tension or to maintain tensional homeostasis, cells would undergo a change in their morphologies. To evaluate whether focal adhesion kinase was activated in dynamic conditions, we determined the expression of activated focal adhesion kinase relative to total focal adhesion kinase proteins of MDAPCa2b SC and PC3 SC at day (23+20) of both culturing conditions. Typically, activation of FAK is mediated via Y397 tyrosine-protein autophosphorylation that triggers the assembly of FA proteins around integrins to form focal adhesion complexes [76]. We observed an increase in protein expression of activated FAK protein (Y397) in both dynamic MDAPCa2b SC and PC3 SC samples compared to their static cultures (figure 2.6(b), 2.6(c)).

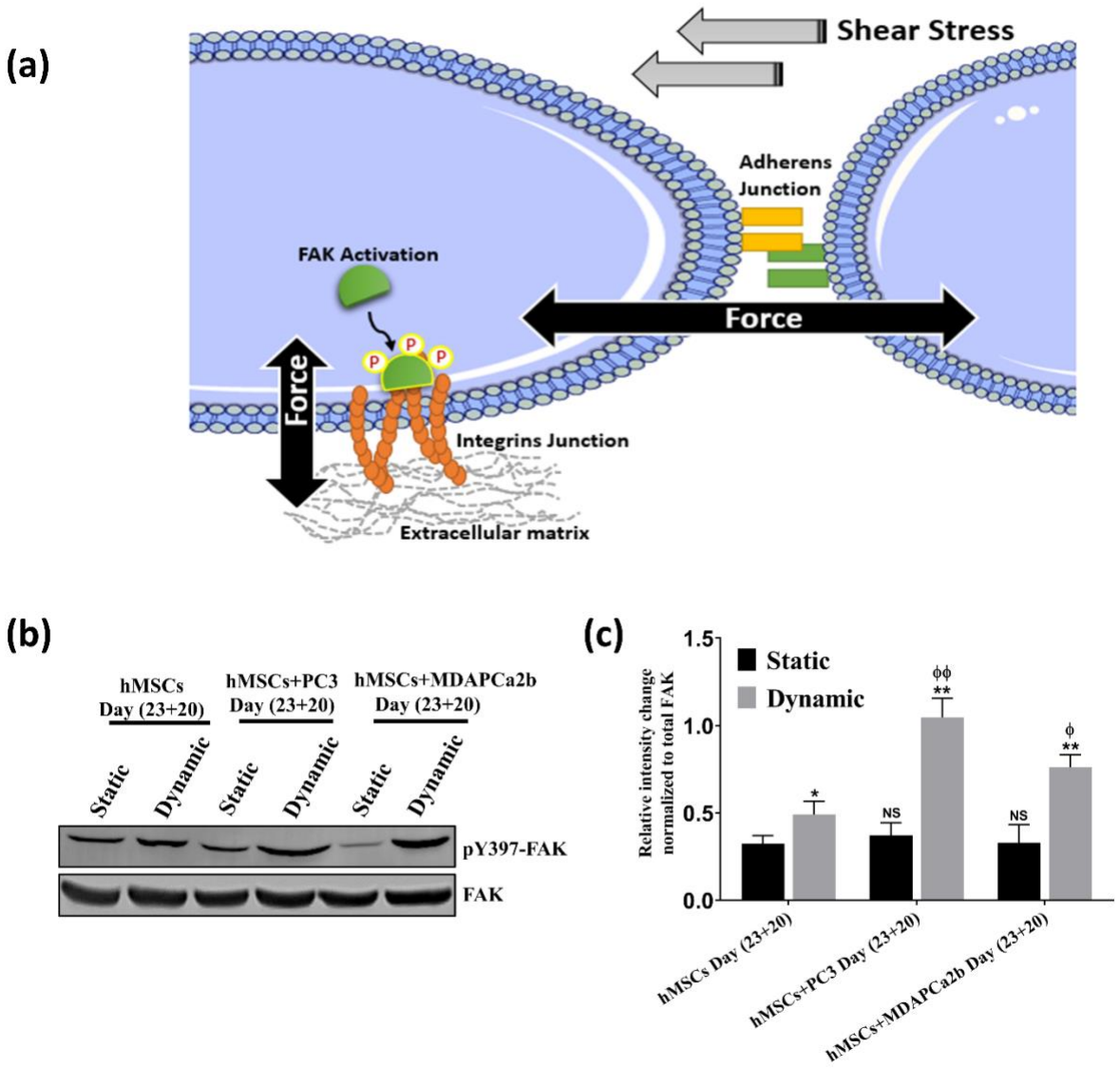

Figure 2.6. Morphological variations of prostate cancer cells mediated via shear stress derived forces on adhesion molecules. (a) Schematic showing cell-cell interaction via adherens junctions and cell-extracellular matrix interaction via integrins junction. Under fluid-derived shear stress, FAK activation (phosphorylation of pY397 domain of FAK) occurs in the cytoplasm that assembles integrins in proximity and binds them with focal adhesion complexes. Simultaneous pulling forces by adherens and integrins cause morphological changes. (b) Protein expression of pY397 FAK was assessed by western blotting. (c) Quantification of p-FAK protein expression relative to total FAK. $*p < 0.05$ and $**p < 0.01$ indicate a significant difference between day (23+20) static and day (23+20) dynamic samples. $^{\phi}p < 0.05$ and $^{\phi\phi}p < 0.01$ indicate a significant difference between day (23+20) hMSCs dynamic and day (23+20) hMSCs+PC3 dynamic samples, and between day (23+20) hMSCs dynamic and day (23+20) hMSCs+MDAPCa2b dynamic samples.

2.4. Discussion

Perfusion bioreactors have extensively been used for bone tissue engineering applications for more than a decade [77]. Recently, some researchers have employed the bioreactors in 3D *in vitro* cancer models [59, 78-81]. The major goal of a bioreactor is to provide a biochemical and biomechanical environment that improves mass transfer and induces shear stress to the cells. It is evident that fluid-derived shear stress affects cellular orientation and functions [82]. Previously, various custom-designed bioreactors have been reported that utilized expensive biocompatible materials for their designs [83]. Here, we employed a cost-effective and reproducible 3D printing technique to fabricate bioreactor chambers and their components.

The flow rate of media is always a critical parameter responsible for the extent of perfusion and the magnitude of fluid-induced shear stress. Moreover, it is a deciding factor for cell attachment and their growth on engineered constructs under dynamic culture. Some studies indicate increased extracellular matrix generation at a high flow rate [84], while others suggest a large number of cell detachment from the scaffold surface at the same flow rate [85]. Thus, the optimization of flow rate is necessary to provide the magnitude of shear stress relevant to cell adherence and their response. In our experiments, we selected a flow rate of 0.2 ml/min based on our preliminary studies and calculated an average velocity of 34.3 µm/s of the medium through the scaffold. Then we estimated wall shear stress (WSS) generated by the fluid flow considering scaffold pore size range of 10 µm to 300 µm. The resulting wall shear stresses ranged between 0.7 mPa and 21.4 mPa, similar to the magnitude calculated in other dynamic studies related to bone differentiation, covering a range of 5 mPa-100 mPa [86-90]. It is possible that WSS larger than 21.4 mPa causes a portion of cells to detach from the scaffold surface, and WSS smaller than 0.7 mPa does not induce the necessary physiological response in our scaffold system. Recently, a study

showed wall shear stress across different blood vessel types using a two-photon imaging approach that reduced in magnitude as target cell approached sinusoidal capillaries near bone marrow, which is 2.9 ± 2.7 dyne/cm^2 [29]. Thus, it could be assumed that the wall shear stress of interstitial fluid is likely less than 290 mPa.

Some studies have considered fluid-derived stress by the interstitial fluid as a critical factor for maintaining bone remodeling and bone growth [91]. In a healthy bone, remodeling homeostasis is always maintained between bone resorption and bone formation processes by osteoblast and osteoclast cells, respectively. However, cancer metastasis to the bone causes an imbalance in this process resulting in bone lesions [92]. Bone is considered the most preferred site for prostate cancer metastasis; however, it is still unclear what factors drive cancer cells towards the bone niche specifically. Various hypotheses have been made that suggest the involvement of chemokine signaling pathways such as CXCL12/CXCR7 in cancer cells homing to the bone [93]. However, the critical role of fluid-derived stress in prostate cancer progression at the metastatic site remains unclear. Keeping these facts in mind, we designed the experiments to shed light on the complex interactions between prostate cancer and bone cells at the metastatic stage and to examine the effect of shear stress on hMSCs and prostate cancer growth patterns under dynamic conditions. We have previously determined the effect of bone niche on prostate cancer progression; however, in this study, we elucidate specifically the effect of biophysical cues on prostate cancer bone metastasis.

We designed and fabricated a perfusion bioreactor integrated with 3D *in vitro* nanoclay based scaffolds to investigate the alteration of cell proliferation and differentiation rate of hMSCs gene and protein expressions, and cell morphologies of tissue-engineered bone and prostate cancer cells under dynamic conditions. First, we examined the role of shear stress on hMSCs proliferation

and osteogenic differentiation and compared the results with static culturing conditions. We observed that the DNA content of hMSCs cultured under dynamic conditions is almost doubled on day-23 compared to static results. Previous findings also reported improved hMSCs proliferation rate under dynamic culture and suggest the critical role of shear stress in increasing proliferation rate [94, 95]. It is well-understood that the functional role of interstitial fluid across bone is to transport nutrients to cells and carry their waste materials while stimulating cell signaling via the shear stress [91]. A perfusion bioreactor also provides a dynamic environment that delivers an increased amount of nutrients to the cells and persuades cells through fluid-driven shear stress. Thus, increased DNA content of dynamic samples can also be associated with improved nutrient supply. We also observed that hMSCs under dynamic conditions were uniformly dispersed all over the scaffold and oriented along the flow direction in contrast to static culture samples that were non-homogeneously distributed, indicating a positive response of fluid shear stress on dynamic samples. Other studies have also reported a uniform and directional dispersal of MC3T3 pre-osteoblasts at day-21 under bidirectional perfusion at 0.1ml/min [96]. Some studies also reported that due to the limited flow of nutrient media throughout the scaffold in static culture, a nutrient gradient is generated that may cause a non-homogeneous distribution of osteoblast cells [58]. However, to understand the critical role of fluid shear stress on hMSCs orientation, we evaluated p-FAK/FAK protein levels in hMSCs and observed that protein levels were significantly (*$p < 0.05$) increased in dynamic samples (figure 6 (c)). It is evident that p-FAK activation plays a critical role in maintaining elongated hMSCs morphology [97] (figure 6 (c)).

Next, we determined the cell cycle of hMSCs by flow cytometry under both culturing conditions to compare the growth phase change of hMSCs. We observed a significantly increased percentage of G0/G1 phases in both culturing conditions on day 23 compared to their day-10

samples indicating maturation of hMSCs to osteoblasts. Interestingly, on day-23, we also noticed a significant decrease in the percentage of G2/M phases in dynamic samples compared to day-23 static samples which can arise because a large number of hMSCs are likely to have already matured into osteoblasts resulting in a slowdown of the G2/M phase. A decrease in the G2/M phase during hMSCs differentiation has also been reported by others [98]. We further confirmed the osteogenic differentiation of hMSCs by evaluating expressions of three crucial factors, such as RUNX2, ALP, and OCN. We observed relatively more downregulation in gene expressions of early-stage biomarkers RUNX2 and ALP and upregulation of OCN, a late-stage marker of osteogenic differentiation in dynamic samples over time, indicating early maturation of hMSCs.

In the second part of the study, we evaluated the effect of dynamic culturing on significant biomarkers of mesenchymal to epithelial transition (MET). MET is a critical step of cancer progression during the metastatic stage that corresponds to a change in the phenotypic behavior of cells from mesenchymal to epithelial. Altered phenotypic behavior at the metastatic site gives cancer cells an ability to increase their survival and proliferation, further relying on two rate-limiting steps: metastatic milieu and shear-stress by interstitial fluid [99]. Previously, we have shown that complex MET cascade occurs in the nanoclay based scaffold models due to prostate cancer homing to hMSCs differentiated bone niche [53]. In the present study, we evaluate the additional effect of fluid-derived shear stress on MET biomarkers E-cadherin and vimentin. E-cadherin expresses on the epithelial cell surface that forms tight junctions with adjacent cells. A loss of E-cadherin expression results in epithelial to mesenchymal transition that is likely to re-express at the metastatic site [73, 100]. An upregulation in E-cadherin expression with low to nearly absent vimentin expression during co-culture of prostate cancer cells with hepatocytes was reported earlier under dynamic conditions [72]. We observed significantly higher E-cadherin

expression in dynamic samples of MDAPCa2b SC and PC3 SC. In contrast, lower or no change in vimentin expression was observed in PC3 SC and MDAPCa2b SC over time compared to their static samples. Immunostaining and SEM results indicated high cell-cell interactions in MDAPCA2b cells and large cell aggregates in PC3 cells and confirmed the upregulation of E-cadherin under dynamic conditions.

Thus, it is clear from our results that fluid-derived shear stress influences cell morphology, yet it is unclear why such alteration happens. Therefore, to delineate the underlying cause of change in morphology, we decided to determine the variations in cell adhesion proteins, which play an essential role in maintaining cell shape integrity underflow. Notably, intercellular and cell-ECM interactions are mediated by adherens junctions and integrins junctions, respectively. Several studies imply crosstalk between these junctions [101-103]. It is also understood that E-cadherin-based intercellular interactions are essential for the reorganization of cell-ECM forces to the periphery of epithelial cell clusters [75]. On the other hand, the importance of integrin-mediated adhesions in modulating intercellular adhesions is also known [104, 105]. Moreover, other studies also establish a connection between E-cadherin regulation via focal adhesion kinase (FAK) signaling in various cancer cells [106, 107]. However, it is still unclear how these adhesion proteins-mediated interactions alter multicellular morphogenesis during fluid-derived shear stress.

In the present study, we have shown that E-cadherin expression increases under fluid flow in both MDAPCa2b and PC3 SC. In addition, we demonstrated variations in phosphorylated focal adhesion kinase (FAK) expression. FAK is a non-receptor tyrosine kinase located in the cytoplasm that regulates several cellular signaling, including cell adhesion, colonization, invasion, and cell proliferation [108-114]. Herein, we demonstrate focal adhesion kinase (FAK) activation in assembling integrin molecules in proximity via a focal adhesion complex. We hypothesized that

under fluid-driven shear stress, both adherent junctions (cell-cell interaction) and integrin junctions (cell-matrix interaction) experience a constant pulling force, which might cause morphological changes (Figure 2.6 (a)). In our study, at the bone metastatic site, we report a significant increase in phosphorylated (Y397) FAK expression relative to their total FAK proteins in both sequential cultures under flow conditions (figure 2.6 (b)). Consistent with our observation of increased p-FAK expressions at low shear stress magnitude, numerous studies have reported increased p-FAK levels in cancer cells at low-level shear-stress. Recent studies of liver cancer stem cells and triple-negative breast cancer cells showed an increased FAK phosphorylation at low-level shear stress magnitude of 2 dynes/cm^2 [115] and 1dyne/cm^2 [116], respectively. However, at high shear stress levels of 12 dynes/cm^{2,} phospho-FAK protein levels were downregulated in triple-negative breast cancer cells [116].

2.5. Conclusion

We have successfully developed a 3D *in vitro* dynamic model to recapitulate bone metastatic prostate cancer behavior under dynamic conditions. We have explored the critical role of fluid-derived shear stress on modulations in cell response. Overall, our results indicate that shear stress promotes hMSCs proliferation, differentiation, and morphological variations. We report that fluid-derived shear stress has a massive impact on hMSC cell morphology. The hMSCs under static culture form cell agglutinates, whereas, under dynamic culture, the cells exhibited a directional alignment with broad and flattened morphology. The fluid flow enabled shear stress significantly influences MET biomarkers (E-cadherin and vimentin) and the cell shape of prostate cancer cells at the metastatic bone site. Our prior studies suggest variation in morphologies between two prostate cancer cell lines under static conditions, with MDAPCa2b cells forming tight dense tumoroids and PC3 cells forming loose aggregates [56]. In comparison, the application of

shear stress in the dynamic experiments largely impacted prostate cancer cell morphology. The dynamic MDAPCa2b prostate cancer cells formed highly compact morphology as early as a day (23+10), and the PC3, unlike the loose aggregates under static conditions, exhibited cell colonization at day (23+10).

Using the 3D metastasis testbed, we demonstrate FAK activation in assembling integrin molecules in proximity via a focal adhesion complex. Evaluation of cell adhesion proteins indicated that the cause of variation in cancer cell morphology under shear stresses arises from the constant force pulling due to increased E-cadherin and phosphorylated Focal adhesion kinase (FAK) proteins under the fluid flow enabled shear stress. Further investigations utilizing computational fluid dynamics will provide an enhanced view into establishing a correlation between fluid shear stress and metastasis progression.

3. HORIZONTAL FLOW BIOREACTOR FOR EVALUATING MIGRATION OF PROSTATE CANCER CELLS AT A LATER STAGE[2]

This chapter describes the significant role of fluid flow in the migration rate of prostate cancer cells at their extravasation stage. The contents of this chapter have been submitted for publication.

3.1. Introduction

Prostate cancer is the most frequently diagnosed cancer in men that tends to metastasize preferentially to the skeleton, leading to malignant bone lesions. Metastatic prostate cancer cells dysregulate the normal bone remodeling process by distressing bone tissue homeostasis. The 5-year survival rate for localized prostate cancer patients is significantly higher than the patients with prostate cancer disseminated to a distant organ [1]. To colonize the bone site, tumor cells invade the extracellular matrix (ECM) of the growing tumor at their primary site, intravasate into the blood circulation, and then extravasate from the blood vasculature to the bone ECM. *In vitro* models have been proved beneficial for studying cancer cell progression and developing novel anticancer drugs. In particular, 3D *in vitro* disease models mimic more closely the pathophysiological microenvironment due to close interaction between different cell types and release of factors responsible for the generation of ECM in a precise system [117, 118]. 3D *in vitro* models bridge the gap between 2D monoculture models, which do not possess *in vivo* structural complexity, and expensive *in vivo* models, often fail to recapitulate the late stage of cancers.

[2]This chapter was co-authored by Haneesh Jasuja, Sharad Jaswandkar, D.R. Katti, and K.S. Katti. Haneesh Jasuja had the primary responsibility for preparing samples, conducting all tests, and drafting this chapter. Kalpana Katti and Dinesh Katti directed the research orientation and revised this chapter.

Previously, we have developed 3D *in vitro* disease models of prostate [119, 120] and breast cancer [28, 55] bone metastasis using polymer-nanoclay based scaffolds that exhibit high porosity of 86.1% with pore sizes ranging between 10-30 μm to 100-300 μm and possess a compressive modulus of 2.495 MPa [60], required for hard tissue growth. We have also investigated the role of interstitial fluid in prostate cancer progression to the bone using a novel customized dynamic 3D *in vitro* model, a perfusion bioreactor [121]. However, understanding the metastatic cascade of cancer cells is essential to pave the way to discovering novel drugs for metastatic cancers. In particular, the extravasation stage, which is a critical process for cancer cells' invasion to the secondary site and subsequent development of metastatic tumors. Extravasation comprises various stages, including slowly rolling, adherence to the sinusoidal capillaries, and transmigration across the capillary's endothelium [29]. Recently, several groups have developed microfluidic platforms to recapitulate the extravasation microenvironment that majorly focuses on the effects of biomechanical cues on the tumor cell motility [122-125]. In addition, Boyden chamber-Transwell assays deliver a relatively simple and high throughput system for quantifying the percentage cell migration [126], yet do not fully recapitulate extravasation and migration behavior under physiological fluid flow conditions. While these models have provided useful insight into the migration behavior of cancer cells at their distant sites, they did not adequately address the effect of interstitial fluid flow on cancer cells' migration rate and their molecular mechanisms.

In the present study, we hypothesized that interstitial fluid flow acts as a driving force for cancer cell migration in the vicinity of cancer cells proximate to the capillary pores; thus, we developed a novel 3D *in vitro* dynamic model integrated with transwell inserts that fully recapitulates *in vivo* microenvironment representing the migration of cancer cells under interstitial fluid flow. Here, we demonstrate the migration of PC3 prostate cancer cells through transwell

insert under both dynamic and static culture conditions. Later, we investigated the molecular mechanism responsible for the migration of cancer cells under different culture conditions. This work suggests that αvβ3 integrins play distinct roles in response to mechanical cues and act as mechanosensory that transduce mechanical signals via αvβ3-MMP 9 signaling axis to promote flow-induced motility of prostate cancer cells.

3.2. Materials and methods

3.2.1. Scaffold preparation

PCL-*in situ* HAP clay scaffolds were prepared as per the protocol described previously [24, 50, 60-62]. In brief, we modified sodium montmorillonite (Na-MMT) clay with an amino acid modifier (5-aminovaleric acid) to increase the d-spacing between the clay sheets. Further, we mixed HAP and modified clay to biomineralize HAP into intercalated nano-clay sheets galleries. Then, we dissolved PCL and 10% *in situ* HAP Clay in 1, 4-dioxane and subjected the resultant solution to freeze-drying extraction to obtain PCL/in-situ HAP Clay scaffolds. We utilized cylindrical scaffolds with dimensions of 12 mm diameter and 3 mm thickness during experiments.

3.2.2. Horizontal flow bioreactor design

The horizontal bioreactor chambers are designed with computer-aided design (CAD) software (SolidWorks v.2018, Dassault Systems) and fabricated using crosslinked Polymethyl-methacrylate (PMMA) polymer by a Formlabs Form 2 3D Printer. The dimensions of the rectangular culture chamber are 50 mm x 30 mm x 32 mm, and each culture chamber supports one scaffold sample (Figure 3.1 A-E). A scaffold holder is designed to put the scaffolds deep into the culture chambers without flipping (Figure 3.1 I-L). Inlet and outlet of bioreactor chambers are connected to tubing (Peroxide-Cured Silicone, ID 1.42 mm, Ismatec) for continuous inflow and outflow of cell culture medium, respectively (Figure 3.1 F-H). Media containing borosilicate

bottles and flow regulating pump are coupled with bioreactor chambers via these tubing. Experiments were carried out at two different flow rates- 0.2 ml/min and 0.05 ml/min. A vent cap with a 0.2 µm gas permeable membrane is placed on the top of the chamber to cover the opening that facilitates gas exchange within the culture chamber and maintains a sterile environment (Figure 3.1 M-N). The whole assembly is placed inside the incubator (Figure 3.1 G-H).

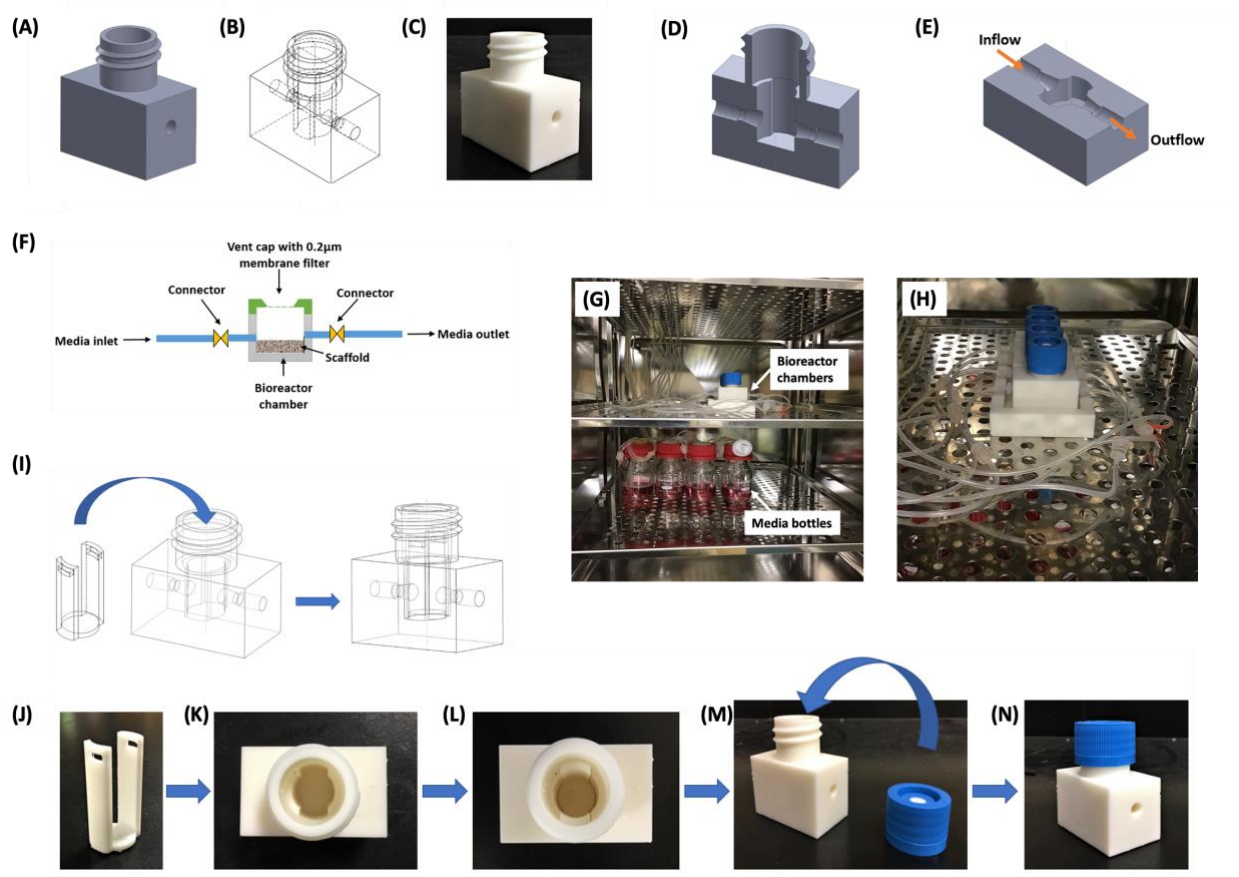

Figure 3.1. Bioreactor design. (A) full view. (B) symmetric view. (C) 3D printed bioreactor chamber. (D) side view. (E) top view. Arrow indicates inflow and outflow fluid directions. (F) Schematic representation of bioreactor and their components with flow directions. (G-H) Bioreactor assembly setup inside the incubator (37 °C, 5% CO2, and high moisture content). (G) Bioreactor chambers (top rack) connected to media bottles (bottom rack) via tubing. (H) Enlarged view of bioreactor chambers positioned inside the incubator. (I) Symmetric view of the chamber and holder showing steps of holder insertion into bioreactor chamber (J-N) Assembly of bioreactor chamber. (J) scaffold holder. (K) Top view of bioreactor chamber. (L) Top view of the bioreactor chamber inserted with scaffold holder. (M) Bioreactor chamber and vent cap. (N) Vent cap fitted bioreactor chamber.

3.2.3. Computational fluid dynamics (CFD) analysis

The bioreactor model and the transwell insert were designed using computer-aided design (CAD) software (SolidWorks v.2018, Dassault Systems). The theoretical analysis of the hydrodynamic performance of the bioreactor was conducted by computational fluid dynamics (CFD), using a SolidWorks flow simulation package. The SolidWorks Flow Simulation is a CAD-integrated Computational Fluid Dynamics (CFD) simulation software fully integrated with the part design environment [127]. It is based on a Cartesian meshing approach integrated directly into the native CAD system [127]. The software uses a discrete numerical technique based on the Finite Volume Method (FVM) to integrate with CFD solvers. The fluid medium in the bioreactor was assumed to be an incompressible fluid with a dynamic viscosity of 6.9×10^{-4} Pa·s and a density of 993.3 kg/m^3 (dynamic viscosity and density of water at 37°C). The scaffold geometry was considered solid with dimensions of 12 mm diameter and 3 mm thickness and assigned total porosity of 86.1%, determined experimentally [60]. The inlet flow rates of 0.05 ml/min and 0.2 ml/min were applied to the bioreactor model based on experiments performed. The other parameters used for the system are described in Table 3.1.

Table 3.1. CFD parameters and approximations applied for the bioreactor system.

Parameters	**Approximations**
Temperature (℃)	37
Pressure (Pa)	101325
Gravitational constant (m/s^2)	-9.81
Fluid	Water
Flow type	Laminar and Turbulent
Wall thermal condition	Adiabatic
Boundary conditions	Inlet and Outlet at a uniform flow rate
Mesh	Global mesh refinement: 4 Local mesh refinement: 5

3.2.4. Cell lines and cell culture

Human mesenchymal stem cells (hMSCs) (PT-2501) (Lonza) were maintained in a complete growth medium (MSCGM Bulletkit medium (Lonza, PT-3001)). Human prostate cancer cells- PC3 (ATCC® CRL-1435™) were purchased from American Type Culture Collection (ATCC) and maintained in a complete growth medium (Kaighn's Modification of Ham's F-12 Medium-ATCC, 30-2004, 10% Fetal Bovine Serum (ATCC, 30-2020), and 1% Pen-Strep antibiotic (Gibco)). The cell cultures were maintained at 37 °C and 5% CO_2 in a humidified incubator.

3.2.5. Cell seeding

We first sterilized the scaffolds under ultraviolet (UV) light for about 1 hour and then immersed the scaffolds into 70% ethanol solution for 12 hours. Further, we washed the scaffolds twice with 1X phosphate buffer saline (PBS). We seeded 1 x 10^5 PC3 cells on each scaffold for viability-related experiments and seeded 5 × 10^5 hMSCs on each scaffold for migration-related experiments. We cultured hMSCs on scaffolds for 23 days for their osteogenic differentiation and mineralized bone formation as described previously [28, 128], before employing them for migration experiments. We refreshed the media for the bioreactor samples every two days and static samples every other day.

3.2.6. DNA quantification

DNA quantification assay was performed to assess the proliferation rate of PC3 cells by measuring their DNA content using a kit (AccuBlue® Broad Range dsDNA Quantitation Kits). Standard solutions were prepared as per the manufacturer's protocol. For sample preparation, we followed the procedure described somewhere else [121]. Briefly, 10 µl of each standard and diluted sample was mixed with 200 µl of working solution and incubated for 30 min at room temperature

in the dark. The fluorescence was measured at Ex350 nm/ Em460 nm using a fluorescence microplate reader (BioTek).

3.2.7. Live dead assay

A live-dead assay was performed to evaluate the viability of PC3 cells under static and flow conditions. The scaffolds seeded with PC3 cells were introduced with both live (Calcein AM) and dead (Ethidium Homodimer III- EthD-III) stains at different time points (Day-4 and Day-8) using a standard protocol (Biotium, 30002-T). Briefly, the scaffolds were rinsed twice with PBS and were incubated in 2 µM calcein AM and 4 µM EthD-III in PBS for 30 minutes at room temperature. Next, the scaffolds were imaged under Zeiss Axio Observer Z1 LSM 700 confocal microscope using Ex/Em wavelengths described in the manufacturer's protocol.

3.2.8. Cell apoptosis by flow cytometry

The apoptosis analysis was carried out using the Propidium Iodide (PI)-AnnexinV double staining method as per the standard procedure (Biolegend). Briefly, samples were retrieved from different conditions on Day 4 and Day 8 and washed thoroughly with cold PBS. Cancer cells were harvested from each scaffold by treating them with 500 µl of TrypLE™ Express enzyme. Next, cancer cells were resuspended in Annexin binding buffer to a concentration of 1×10^6 cells/ml. Further, 100µl of cell suspension of each condition was treated with 5µl of Fluorescein isothiocyanate (FITC) conjugated Annexin V and 10µl of PI stains and incubated in the dark for 15 minutes at room temperature. The cell suspension of each sample was further diluted with 400 µl of Annexin binding buffer and analyzed using BD Accuri C6 Flow cytometer.

3.2.9. Gene expression by RT-qPCR

Scaffold samples containing PC3 cells were retrieved from different culture conditions on Day 8 to assess their apoptosis-related gene expressions. RNA was isolated using TRIzol reagent

and purified using Direct-zol RNA MiniPrep kit (Zymo Research). For migration-related gene expressions, PC3 cells were treated with TRIzol reagent after 24 hours of the migration experiment for their RNA isolation. Next, RNA was reverse transcribed to cDNA using random primers and M-MLV reverse transcriptase (Promega), and the mRNA expressions were quantified using SYBR green master mix. The qPCR reaction conditions used during each run include holding stage - 95°C, 5 minutes followed by cycling stage - 40 cycles of 95°C, 30 seconds and 60°C, 1 min. The expressions of various genes related to apoptosis and migration- TGFβ-1, Caspase-9, Bcl-2, p53, αv, β3, MMP-9, and CXCR4 were analyzed and normalized to the mean of β actin. The details of the primers are given in Table 3.2. The relative fold change was calculated using the 2^(-ΔΔCt) comparative method.

Table 3.2. The primer sequence used in the RT-PCR experiment.

Gene	Forward primer	Reverse primer
β actin	5'- GGC ATC GTG ATG GAC TCC-3'	5'- GCT GGA AGG TGG ACA GCG-3'
TGFβ-1	5'- AAG TTG GCA TGG TAG CCC TT-3'	5'- CCC TGG ACA CCA ACT ATT GC-3'
Caspase 9	5'- GAG GGA AGC CCA AGC TGT TC-3'	5'- GCC ACC TCA AAG CCA TGG T-3'
p53	5'- CGG GAT CCA TGG AGG AGC CGC AGT CAG AT-3'	5'- CCG CTC GAG TTT CTG GGA AGG GAC AGA AGA-3'
Bcl-2	5'- GGC TGG GAT GCC TTT GTG-3'	5'- CAG CCA GGA GAA ATC AAA CAG A-3'
αv	5'- GAA AAG AAT GAC ACG GTT GC -3'	5'- AGT GAT GAG ATG GTC CCG CT -3'
β3	5'- ACT GCC TGT GTG ACT CCG ACT -3'	5'- CGC GTG GTA CAG TTG CAG TAG-3'
MMP-9	5'-TGG GCT ACG TGA CCT ATG ACA T-3'	5'-GCC CAG CC ACC TCC ACT CCT C-3'
CXCR4	5'- GAT CAG CAT CGA CTC CTT CA-3'	5'- GGC TCC AAG GAA AGC ATA GA-3'

3.2.10. Transwell migration assay

For the transwell migration assay, we have customized the bioreactor assembly to fit better the transwell insert and accommodation of bone mimetic scaffold underneath the transwell insert. A total of $4x10^4$ PC3 cancer cells were seeded into each Transwell insert (Corning, Inc., Corning, NY, USA) of 8.0 μm pore size in 100μl PC3 media containing 2% FBS and allowed to adhere to the surface for 3 hours. Next, the media was replaced with 100μl serum (FBS) free media, and the inserts were moved into the bioreactor. The cells were allowed to migrate towards the lower chamber containing complete PC3 media (F-12 K with 10% FBS) and towards tissue-engineered bone with complete PC3 media (F-12 K with 10% FBS). After 24 hours of incubation, cells that remained on top of the filter were gently removed using cotton swabs. The percentage of cells migrated through the filter was measured using the Alamar Blue reagent assay (Invitrogen) following the manufacturer's protocol. The fluorescence intensity was measured using excitation 570 nm and emission 600 nm. PC3 cells seeded in the wells without inserts were considered positive control, and fluorescence emitted only by Alamar blue reagent was considered negative control or background signal. The percentage migration was calculated by using the formula.

$$\text{Percentage migration} = \frac{\text{Fluorescence of migrated cells} - \text{background signal}}{\text{Fluorescence of total cells without insert} - \text{background signal}} \; X \; 100$$

3.2.11. Western blot analysis

PC3 cells were harvested from transwell inserts and protein was extracted using RIPA lysis buffer. Next, total protein was estimated using the Bradford assay (Thermofisher). The proteins were separated using 10% (v/v) SDS-PAGE gels and transferred to a 0.2 μm PVDF membrane. The membrane was blocked for 1 hour at RT with a blocking buffer (5% bovine serum albumin, 0.05% Tween-20 -Alfa Aesar). Next, the membrane was incubated with a primary antibody overnight at 4°C. The primary antibodies used for the analysis were p-Smad2 (Cell signaling

#3108, 1:1000 dilution), Smad2 (Cell signaling #3102, 1:1000 dilution), p-Akt1 (Cell signaling #9271, 1:1000 dilution), and Akt (Cell signaling #9272, 1:1000 dilution). Further, the membrane was incubated for 1 hour at room temperature with a horseradish peroxidase-conjugated secondary antibody at 1:5000 dilution. The blots were scanned under a Chemiluminescence imaging system (Applied Biosystems).

3.2.12. Statistical analysis

GraphPad Prism v7.04 software was used to perform statistical analysis. The data were presented as mean ± standard deviation (SD). Data were analyzed using one-way, or two-way ANOVA followed by Tukey's post hoc analysis. The difference between the two groups was considered statistically significant for $p < 0.05$.

3.3. Results

3.3.1. Optimization of interstitial flow velocities and shear stress for optimum cell growth

The reported interstitial fluid velocities range *in vivo* is 0.1–4 μm/s [123, 124]. Here, we analyzed two different inlet flow rates- 0.05 ml/min (low flow rate) and 0.2 ml/min (high flow rate)- to attain physiological interstitial fluid velocity range and understand the correlation between fluid shear stress and cellular response. The simulated fluid flow on the scaffold surface analyzed by CFD -displayed heterogeneous fluid velocity and shear stress magnitudes. The velocity range attained at different flow rates was 5.0 μm/s (vel_{min}) and 50 μm/s (vel_{max}), and 0.5 μm/s (vel_{min}) and 5.0 μm/s (vel_{max}) corresponding to 0.2 ml/min and 0.05 mL/min, respectively. The fluid shear stress estimated for 0.2 ml/min ranged between 0.5 mPa and 3 mPa, while 0.05 mL/min ranged between 0.02 and 2 mPa. The color gradient indicates faster flow in the scaffold's center than the stagnant fluid layer near the wall (Figure 3.2 A-D). From CFD results, we concluded that the physiological velocity was achieved at a 0.05 ml/min flow rate. However, to understand the effect

of high flow rate on cellular response and to optimize flow rate experimentally, we performed a cell viability assay using both flow rates.

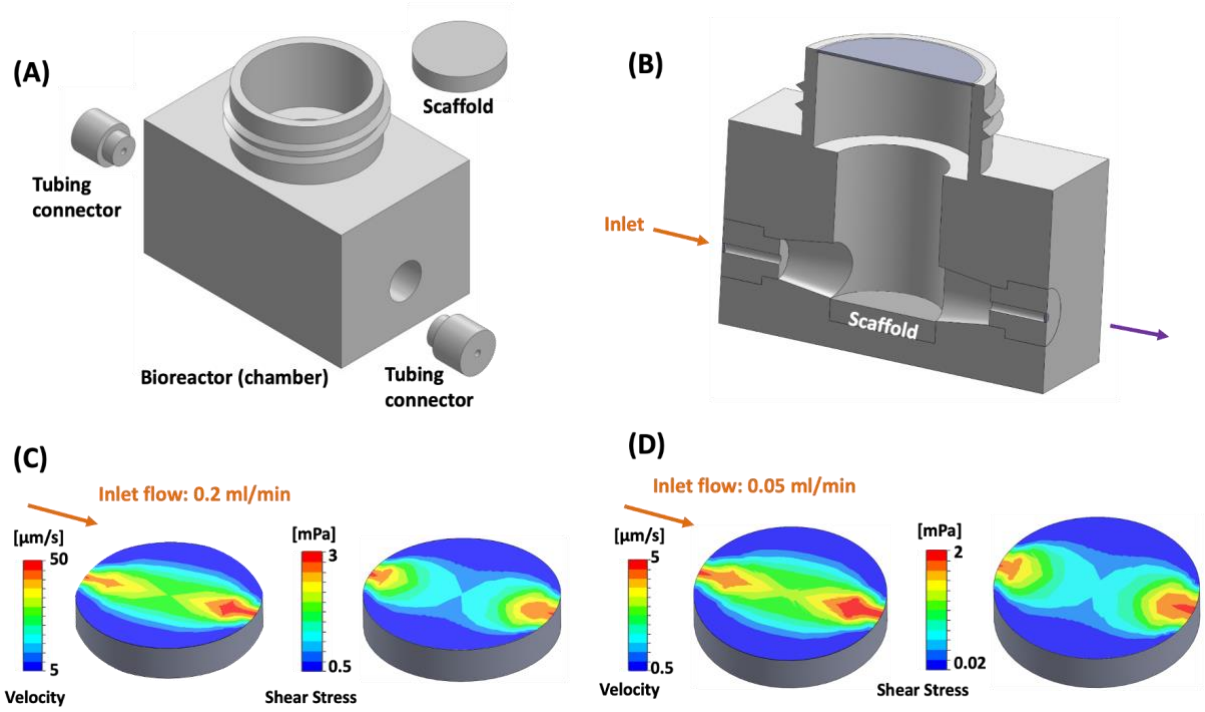

Figure 3.2. (A) Bioreactor assembly components. (B) The sectional view of bioreactor assembly. (C) Velocity and shear stress distribution on scaffold surface at inlet flow of 0.2 ml/min. (D) Velocity and shear stress distribution on scaffold surface at inlet flow of 0.05 ml/min. Arrows represent the direction of fluid flow.

3.3.2. High flow rate inhibits cell growth and induces apoptosis

To assess the viability of PC3 cells under static and different flow conditions, we measured their DNA content. We observed that the DNA content of PC3 cells on Day-4 was significantly higher under both 0.2 ml/min (*$p<0.05$) and 0.05 ml/min (**$p<0.01$) flow conditions compared to static culture. Similarly, on Day-8, we observed significantly higher DNA content of PC3 under 0.05 ml/min ($^{\$}<p<0.05$) compared to their static culture. However, the DNA content of PC3 cells under 0.2 ml/min flow rate was significantly decreased ($^{@}p<0.05$) compared to 0.05 ml/min flow rate conditions (Figure 3.3A). Live-dead staining assay revealed similar outcomes, representing a

reduced population of live cells under high flow rate conditions on Day-8 compared to low flow rate conditions (Figure 3.3B).

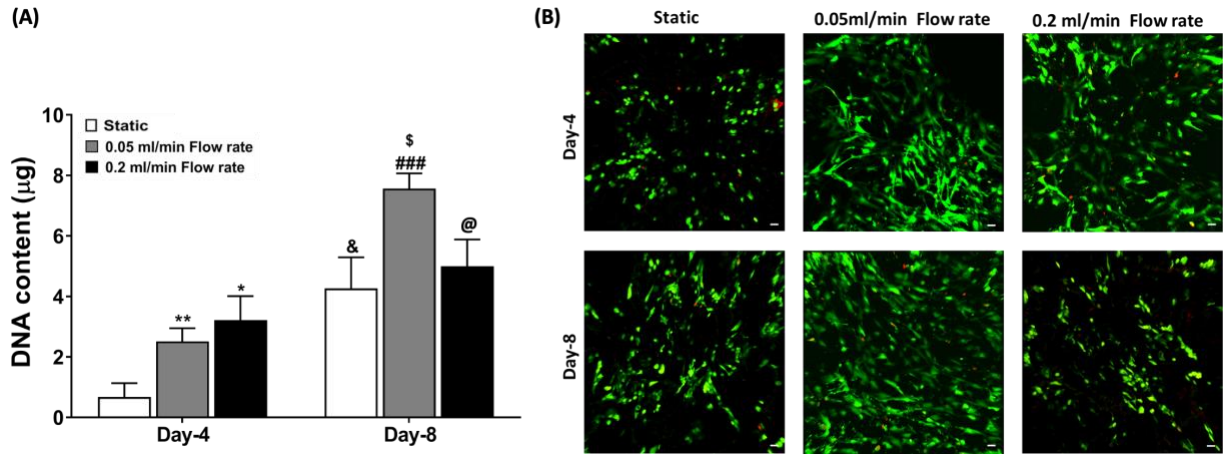

Figure 3.3. Cell viability was assessed on Day-4 and Day-8 using Static culture (control), 0.05 ml/min flow rate, and 0.2 ml/min flow rate. (A) DNA content. (B) live-dead assay. Green fluorescence represents live cells and red fluorescence represents dead cells. Scale bar 100µm *p<0.05 and **p<0.01indicates a significant difference between the static sample and different flow rate samples on Day-4. $^{\&}$p<0.05 indicates a significant difference between the static sample on Day-4 and Day-8. $^{\#\#\#}$p<0.001 indicates a significant difference between the 0.05 ml/min flow rate sample on Day-4 and Day-8. $^{\$}$p<0.05 indicates a significant difference between the static sample on Day-8 and the 0.05 ml/min flow rate sample on Day-8. $^{@}$p<0.05 indicates a significant difference between the 0.05 ml/min flow rate sample on Day-8 and the 0.2 ml/min flow rate sample on Day-8.

3.3.3. TGF-β1 induces apoptosis under a high flow rate

To investigate the possible reason for decreased cell growth of PC3 cells under high flow rate, we performed a cell apoptosis assay by flow cytometry. We did not observe significant changes in the apoptosis rate on Day-4 between 0.2 ml/min and 0.05 ml/min flow rates; however, on Day-8, we observed a significantly higher percentage of apoptotic cells (22.60 ± 0.55 %) cultured under a high flow rate compared to low flow rate conditions (11.01 ± 0.50 %), indicating 0.2 ml/min flow rate is not suitable for PC3 cells growth for a prolonged period (Figure 3.4 A-C).

Next, to investigate the molecular mechanism responsible for apoptotic induction of PC3 cells at Day-8 under a high flow rate, we examined apoptosis-related genes. We observed that mRNA levels of tumor suppressor gene, p53 (***$p<0.01$) and apoptotic gene, caspase-9 (**$p<0.01$) were significantly upregulated in PC3 cells under high flow rate while expressions of antiapoptotic gene, Bcl-2 (***$p<0.01$) were downregulated, suggesting apoptotic induction in PC3 cells under high flow rate. We also examined mRNA levels of TGF-β1, which is highly accountable for apoptotic induction in tumor cells [129]. We observed a significant upregulation in TGF-β1 mRNA levels (***$p<0.001$) under high flow rate compared to low flow rate conditions. It is also reported that TGF-β1 acts as both a tumor suppressor and tumor inducer, promoting cell apoptosis via the Smad-dependent pathway while suppressing apoptosis or enhancing cell survival via Smad independent-PI3K/Akt pathway [130]. Thus, we decided to investigate the feasibility of these two signaling pathways to understand the possibility of an increase in TFG-β1 mRNA levels at high flow rate conditions. We observed significantly high protein expression of p-Smad2 under high flow rate conditions compared to low flow rate conditions, indicating the tumor suppressor effect of TGF-β1 under high flow conditions. In addition, we observed a thick band of p-Akt under low flow conditions while a very thin p-Akt band under high flow rate conditions, suggesting that the survival of PC3 cells was decreased under high flow conditions (Figure 3.4 D-F).

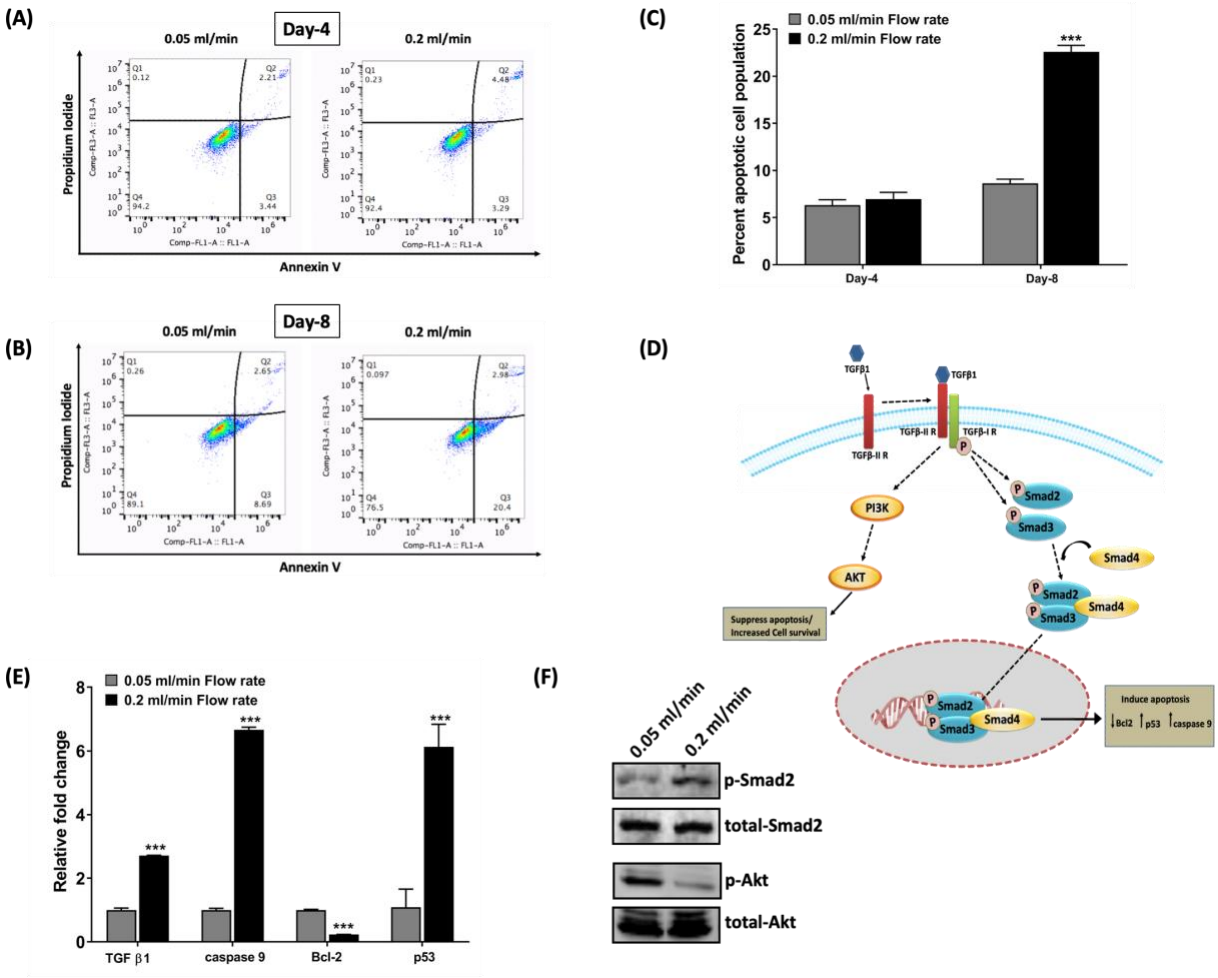

Figure 3.4. Cell apoptosis was assessed at 0.05 ml/min and 0.2 ml/min flow rates. (A-B) Representative dot plot presenting percent live, early, and late apoptotic cells following double staining with Annexin V and Propidium Iodide on Day-4 and Day-8. (C) The percentage of cell apoptosis was calculated on Day-4 and Day-8 by adding the percentage of early apoptotic and late apoptotic cells under different conditions. (D) Possible mechanism of TGF-β1 mediated tumor suppression and tumor induction. (E) Quantitative RT-PCR data for apoptosis-related genes on Day-8. (F) Protein expression of p-Smad2 and p-Akt was assessed by western blotting on Day-8. ***$p < 0.001$ indicates a significant difference between the samples at 0.05 ml/min and 0.2 ml/min flow rates.

3.3.4. Physiological interstitial fluid velocity induces a high migration rate of prostate cancer cells

To evaluate the migration of PC3 cells through transwell insert under flow conditions, we employed a 0.05 ml/min flow rate based on our CFD (Figure 3.2) and viability (Figure 3.3) results. From CFD analysis using transwell insert without scaffold (Figure 3.5 A-B), we demonstrated that

shear stress attained at the membrane of transwell insert ranged between 0.005 mPa and 0.08 mPa, which was nearly equivalent to the shear stress range (0.005 mPa - 0.1 mPa) at the membrane of transwell insert in the presence of scaffold, indicating that similar fluid derived shear stress acting on PC3 cells in the presence or absence of tissue-engineered bone.

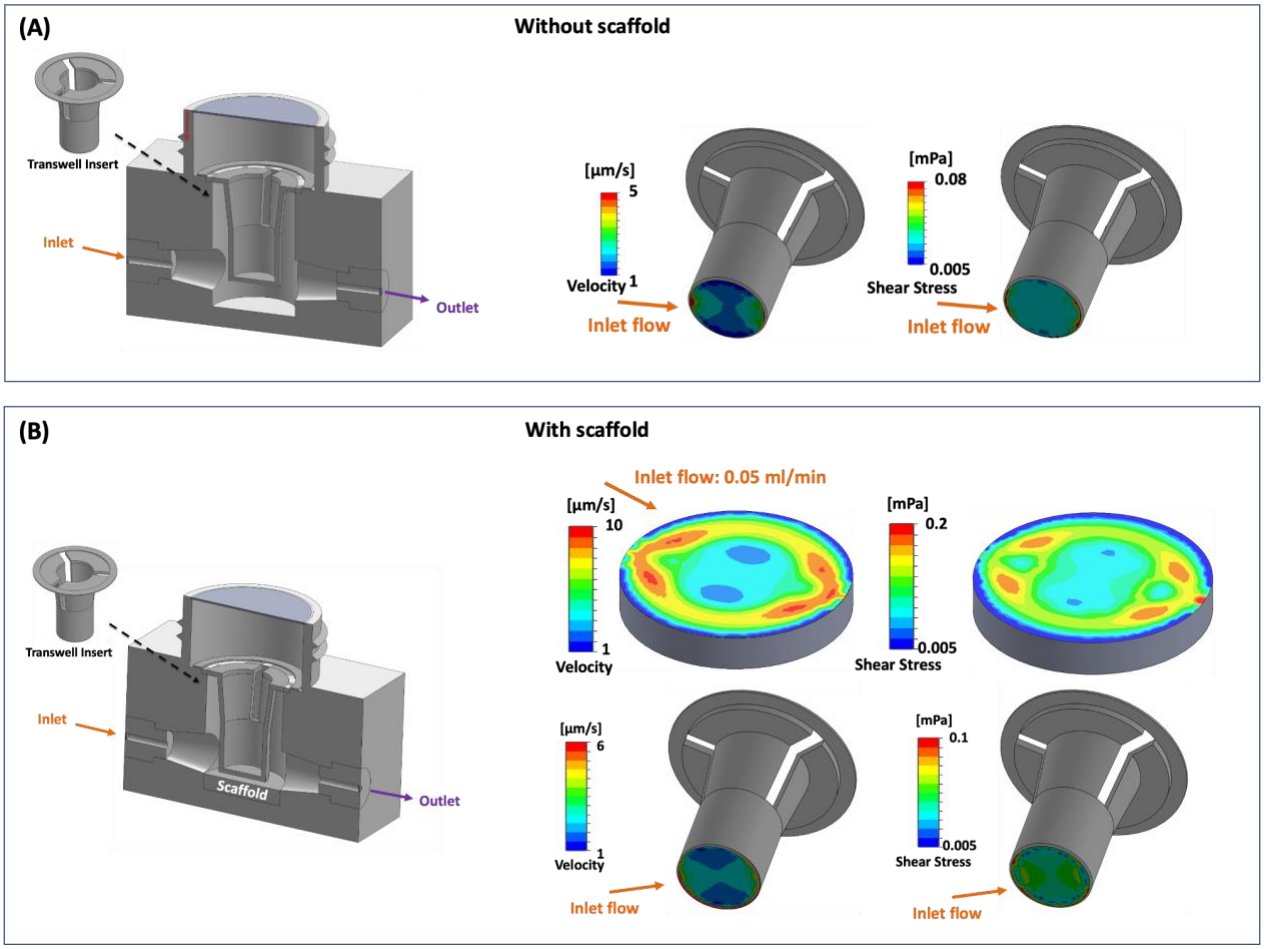

Figure 3.5. (A) Bioreactor assembly with transwell insert without scaffold (upper left), velocity and shear stress distribution on transwell membrane surface at inlet flow of 0.05 ml/min (upper right). (B) Bioreactor assembly with transwell insert and scaffold (lower left), velocity and shear stress distribution on the scaffold and transwell membrane surface at inlet flow of 0.05 ml/min (lower right). Arrows represent the direction of fluid flow.

First, we evaluated the migration rate of PC3 cells under static and dynamic conditions without placing a bone-containing scaffold underneath the transwell insert to understand the effect of continuous fluid flow on migration rate. After 24 hours of incubation, we observed that the

percentage migration of PC3 cells under fluid flow was increased by ~ 2-fold (28.64±5.61%) compared to cells under static condition (13.51±2.47%), indicating the effect of fluid flow on the migration rate of PC3 cells. Next, we evaluated the effect of flow conditions on cell migration rate in the presence of bone. We observed that overall percentage migration through the transwell insert was increased in the presence of tissue-engineered bone under both culturing conditions; however, under dynamic conditions, the percentage of cell migration (73.24±1.05%) was significantly higher ($^{\&}p<0.01$) than static culture (52.95±4.08%) (Figure 3.6 A-B). Thus, to investigate the molecular mechanism responsible for the observed change in percentage cell migration under flow conditions and in the presence of bone, we examined migration-related gene expressions under different culture conditions.

3.3.5. αvβ3 integrins activation via fluid flow promotes percentage cell migration

Fluid shear stress activates αvβ3 integrins that convert mechanical stimulation into chemical signals inside the cells and activate downstream signals [33, 131-133]. We observed that the mRNA levels of αv (***$p<0.001$) and β3 (***$p<0.001$) integrins in PC3 cells were significantly upregulated under dynamic conditions compared to static conditions. Next, we investigated MMP-9 gene expressions and observed that mRNA levels of MMP-9 were also significantly upregulated under dynamic conditions (*$p<0.05$) compared to static conditions in the absence of bone, indicating the effect of fluid shear stress on cancer cells migration. We also demonstrated mRNA levels of αv, β3, and MMP-9 in PC3 cells in the presence of tissue-engineered bone under both dynamic and static culture conditions. The results showed that mRNA levels of αv and β3 in PC3 cells in the presence of bone were not significantly different from without bone samples. However, expression levels of MMP-9 in PC3 cells in the presence of bone were significantly higher than in the absence of bone under dynamic conditions, indicating the role

of other factors in the overall increase in cell migration (Figure 3.6 C). Thus, to understand the reason behind upregulation in MMP-9 levels in the presence of bone, we planned to investigate other genes related to migration.

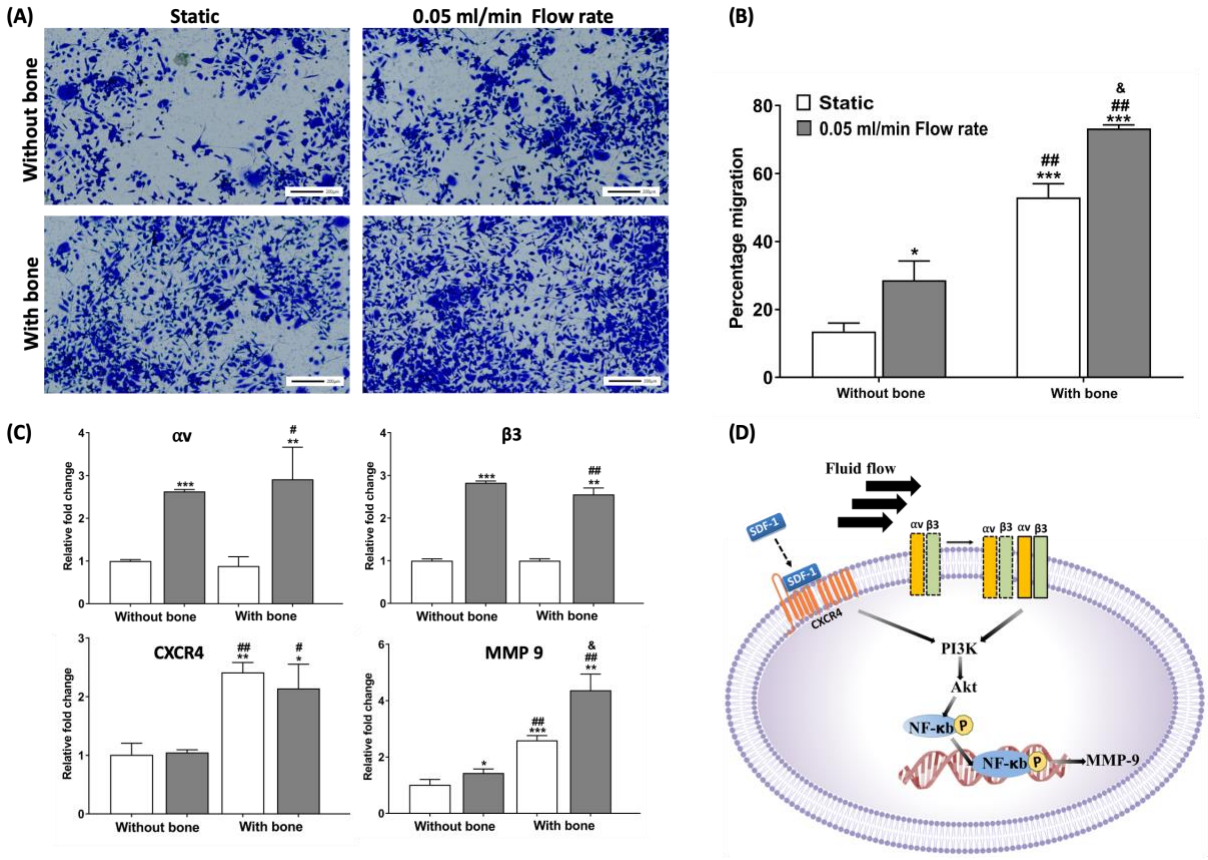

Figure 3.6. Transmembrane invasion assay showing migration of PC3 cancer cells through transwell inserts with and without bone under static and dynamic culture. (A) Migrated cells stained with crystal violet dye. (B) Percentage cell migration determined using Alamar Blue assay. (C) Gene expression of migration-related genes determined by RT-qPCR. (D) The proposed mechanism of CXCR4 and αvβ3 integrins mediated the increase in MMP-9 levels under dynamic conditions in the presence of bone. *$p<0.05$, **$p<0.01$, and ***$p < 0.001$ indicate a significant difference between the static sample without bone and other conditions. $^{\#}p<0.05$ and $^{\#\#}p<0.01$ indicate a significant difference between the dynamic sample without bone and other conditions. $^{\&}p<0.05$ indicates a significant difference between the static sample with bone and dynamic sample with bone.

3.3.6. CXCR4/CXCL12 interaction leads to increased percent cell migration in the presence of bone

CXCR4 is a crucial regulator of prostate cancer invasiveness and metastasis development [134, 135]. High CXCR4 expression in prostate cancer cells is associated with their propensity to metastasize to the bone, a tissue that expresses a high level of the chemokine CXCL12 [135, 136]. As our results showed upregulation in MMP-9 levels in the presence of bone, we hypothesized that CXCR4 activation led to an increase in MMP-9 levels. Thus, we investigated CXCR4 mRNA levels of PC3 cells in the presence and absence of bone under both conditions. We observed a significant increase in CXCR4 levels in the presence of bone under both conditions compared to the without bone scaffolds. We also noticed that CXCR4 mRNA levels were not significantly changed in the presence of bone under static and dynamic conditions, indicating that CXCR4 activation in PC3 cells is not influenced by flow conditions but by the bone (Figure 3.6 C). However, significant upregulation in MMP-9 levels in the presence of bone under dynamic conditions suggesting us a synergistic effect of CXCR4 and $\alpha v\beta 3$ integrins in increased migration rate (Figure 3.6 D).

3.4. Discussion

This study aims to investigate the role of interstitial fluid flow in prostate cancer cell migration and the underlying mechanism. Our previous study showed that interstitial fluid flow has a critical impact on the progression of prostate cancer cells at the bone site [121]. We observed that continuous interstitial fluid flow altered the morphology of prostate tumors and their gene levels. However, to understand the role of interstitial fluid flow on the migration of prostate cancer cells at their extravasation stage, we have designed a new bioreactor model. Extravasation is a critical step of cancer metastasis where cancer cells transmigrate from capillaries to a distant organ

[29]. Some recent studies have shown the crucial role of interstitial fluid flow in cancer cell motility at a distant organ, using microfluidic chip models [124, 125]. However, in the present study, we studied the role of interstitial fluid flow in promoting the migration of prostate cancer cells through transwell inserts. To recapitulate this scenario, we designed a bioreactor system that accommodates both- transwell inserts and tissue-engineered bone, allowing cancer cells to migrate towards bone under interstitial fluid flow. However, before performing this experiment, we optimized the flow rate for cell growth by evaluating their cell viability at different flow rates. We observed a decrease in DNA content of PC3 cells under high flow rate (0.2 ml/min) compared to low flow rate (0.05 ml/min) conditions over time, suggesting that high flow rate induces cell apoptosis (Figure 3.3 A). TGF-β1 has been well explored for its role in inducing cell apoptosis [129, 130, 137]. It is generally suggested that TGF-β1 induces cell apoptosis via canonical Smad signaling (Figure 3.4 D) where TGF-βRI and TGF-βRII form complex in the presence of TGF-β1 and activate Smad2 and Smad3, which in turn activates Smad4 and thereby mediating programmed cell death via activating pro-apoptotic genes such as caspase 9 [138]. TGF-β1 also promotes apoptosis by inhibiting expressions of the antiapoptotic gene, Bcl-2 [139]. We also explored the gene expression of TGF-β1 and other apoptosis-related genes. We observed that levels of Bcl2 were downregulated while levels of caspase 9 and p53 were upregulated under high flow rate conditions compared to static culture (Figure 3.4 E). PI3K/Akt signaling pathway is an essential pro-survival pathway that protects cells against apoptosis-inducing effects of TGF-β1[140, 141]. Thus, a shift in the balance between two different signaling pathways decides the fate of cells. In the present study, we observed upregulation in TGF-β1 in high flow rate conditions compared to low flow rates. We also demonstrated hyperactivation of Smad2 under high flow rate compared to

low flow conditions while a decrease in p-Akt levels, suggesting that a shift in balance occurs at high flow rate conditions, leading to cell apoptosis (Figure 3.4 F).

Based on these results, we decided to carry out migration studies at low flow rate conditions. αvβ3 integrins play a critical role in prostate cancer metastasis to bone. Several studies have confirmed αvβ3 integrins mediated adhesion and migration of cancer cells that activate downstream PI3K/Akt signaling, leading to increased cell migration [133, 142, 143]. In the present study, we evaluated the effect of fluid shear stress on αvβ3 integrins and MMP-9 levels. We observed that mRNA levels of MMP-9 and αvβ3 integrins were upregulated under flow conditions, suggesting the role of fluid shear stress on PC3 cell migration (Figure 3.4 C). However, we also noticed that the overall migration rates and MMP-9 levels of PC3 cells were higher in the presence of tissue-engineered bone, thus we investigated CXCR4 gene expressions (Figure 3.4 B-C). In addition, MMP-9 levels were higher under dynamic conditions compared to static conditions in the presence of bone.

CXCR4 is highly expressed in several malignant tumors, including prostate cancer, which confers a more aggressive behavior of cancer cells [144]. CXCL12 (SDF-1)/CXCR4 interactions play an essential role in prostate cancer migration and invasion to the bone by activating Akt1 and MMP-9 expressions [134, 135]. Previously, it was also reported that interstitial fluid flow increased glioma [36] and Hepatocellular Carcinoma Cell (HCC) [145] invasion via CXCR4 dependent signaling by increasing CXCR4 levels. However, we did not observe any significant change in CXCR4 levels in the presence of bone under static and dynamic conditions (Figure 3.4 C). Thus, our results conclude that a significant increase in percent cell migration rate and MMP-9 levels in the presence of bone under dynamic conditions is not solely regulated by CXCR4 but also results from the synergistic effect of αvβ3 integrins activation (Figure 3.4 D). Overall, our

results suggest that mechanical cues by fluid flow play a significant role in the migration of prostate cancer cells.

3.5. Conclusion

Our findings suggest that interstitial flow-induced shear stress could be a critical factor in regulating the migration of prostate cancer cells at their extravasation stage. In the present study, we observed that the fluid flow rate corresponding to the physiological velocity of the interstitial fluid is optimum for better cell growth compared to a high flow rate, where we observed suppression in the growth rate of PC3 cells due to induction in apoptosis. Thus, we investigated the effect of physiological fluid velocity on the migration rate of PC3 cells and demonstrated that fluid shear stress contributed to an increased migration rate of PC3 cells via increased expression of αvβ3 integrins that further activate downstream signaling leading to an increase in MMP-9 levels. It is well accepted that fluid flow-derived shear stress is a fundamental determinant of cell behavior regulating tumor biology. Thus, our results could be considered in controlling tumor progression and developing new inhibitors. The novel bioreactor we developed could be utilized for understanding the growth and migration of different cancer types in the future.

4. VALIDATION OF NANOCLAY-BASED NOVEL 3D *IN VITRO* BONE METASTATIC MODEL OF BREAST CANCER WITH PATIENT-DERIVED BREAST CANCER CELL LINES[3]

This chapter describes the validation of the 3D *in vitro* bone metastatic model using patient-derived breast cancer cell lines-NT013 and NT023. The contents of this chapter have been submitted for publication.

4.1. Introduction

Breast cancer is a leading cause of cancer-related deaths in women worldwide [1], causing fatal skeletal failure at their advanced stage [146]. Due to complex cellular heterogeneity within cancer cells [147] and the low success rate of novel drugs for metastasized breast cancer in clinical trials [148], effective treatment for advanced-stage breast cancer remains a challenge for researchers. While some preclinical models, such as two-dimensional (2D) monolayer cell culture models and *in vivo* mice models, have been utilized by researchers for pre-clinical cancer research, these models possess some limitations. 2D models poorly recapitulate *in vivo* complexity due to a lack of cell- microenvironment interactions, while *in vivo* models often failed to develop into metastatic disease [149]. Thus, there is a need to create new predictive preclinical models that better recapitulate human tumor biology at their advanced stage and can be used for high-throughput drug screening. Increasing evidence showed that three-dimensional (3D) disease models derived from patients' healthy and tumor tissue could better predict pathogenesis of cancer cells and provide a more accurate measurement of potential drugs than existing models because

[3]This chapter was co-authored by Haneesh Jasuja, Farid Solaymani Mohammadi, Jiha Kim, Anu Gaba, D.R. Katti, and K.S. Katti. Haneesh Jasuja had the primary responsibility for preparing samples, conducting all tests, and drafting this chapter. Kalpana Katti, Dinesh Katti, and Jiha Kim directed the research orientation and revised this chapter. Farid Solaymani Mohammadi isolated the cancer cells from the patient sample.

these models retain characteristic features of cancer cells derived from individual patient's cells [150]. Despite classifying breast cancer cells into three categories based on their cell surface receptors and their growth behavior, breast cancer patients within each category can have markedly different disease outcomes and therapeutic responses [151]. Thus, models derived from patients' cancer cells could help researchers better predict therapeutic responses.

3D spheroid models display tumor heterogeneity *in vitro* and can be used for drug screening studies [152]; however, to account for the effect of extracellular matrix (ECM) on tumor growth, there is a need for a novel model that could provide a platform for ECM formation by the cells. Thus, to address this issue, we developed a novel 3D *in vitro* bone metastatic scaffold-based model using a tissue-engineered approach, providing a platform for bone marrow-derived mesenchymal stem cell differentiation to bone cells and generating their ECM for breast cancer dissemination to better mimic breast cancer bone metastasis [55, 153]. Bone metastatic scaffolds possess high porosity (86.1%) with a pore size range between 100-300 μm and exhibit a high compressive modulus of 2.495 MPa, essential for hard tissue growth [60]. Previously, we utilized commercial human breast cancer cells- MCF-7 and MDAMB231 to develop this 3D *in vitro* breast cancer bone metastasis model [55] and investigated the role of the Wnt/β-catenin pathway in osteogenic differentiation of hMSCs on scaffold surface during breast cancer bone metastasis [28].

In the present study, we have validated our 3D *in vitro* bone metastatic model using patient-derived breast cancer cell lines. First, we demonstrated the role of bone cells and bone extracellular matrix (ECM) on the progression of patient-derived breast cancer cells to bone. Next, we investigated the role of cytokines released by different breast cancer cell types on the osteogenic differentiation of mesenchymal stem cells using the Wnt/β-catenin pathway.

4.2. Materials and methods

4.2.1. Preparation of polycaprolactone (PCL)-*in situ* hydroxyapatite (HAP) clay scaffolds

PCL-*in situ* HAPclay scaffolds were prepared as per the procedure described previously [24, 50, 60-62]. Briefly, PCL-*in situ* HAPclay scaffolds were prepared using the freeze-drying method by mixing 10% *in situ* HAPclay with PCL. HAP was biomineralized into intercalated nanosheets of montmorillonite (MMT) clay due to increased d-spacing between sheets by 5-aminovaleric acid modifiers**,** resulting in modification of Na-MMT clay to *in situ* HAPclay. Finally, 12mm diameter and 3mm thick cylindrical scaffolds were used for the experiments.

4.2.2. Cell lines and cell culture

Human mesenchymal stem cells (hMSCs) were purchased from Lonza (PT-2501) and cultured in MSCGM Bulletkit medium (Lonza, PT3001). Human breast cancer cell lines NT013 and NT023 were derived from the patient tissue samples obtained from Sanford Roger Maris Cancer Center, Fargo. The ethical committee approved the study, and before surgery, all patients provided written informed consent to allow any excess tissue to be used for research. Samples were transported to the research lab using a transportation medium containing DMEM, 1% of pen/strep mix (100×), gentamicin (10 mg/ml) and amphotericin B (250 µg/ml). Breast cancer cells were isolated using a cell isolation kit (Miltenyi biotec) following the manufacturer's protocol and co-cultured with irradiated 3T3-J2 feeder cells (Kerafast) (Figure 1 (A)). Finally, cells were maintained at 37°C and 5% CO_2 in high glucose DMEM containing 5 µg/ml insulin, 250 ng/ml amphotericin B, 10 µg/ml gentamicin, 0.1 nM cholera toxin, 0.125 ng/ml epidermal growth factor (EGF), 25 ng/ml hydrocortisone, ROCK inhibitor Y-27632 10 µM, 10% (v/v) FBS, 100 U/mL penicillin and 100 µg/mL streptomycin.

4.2.3. Cell seeding

Scaffolds were sterilized in 70% ethanol for 24 hours, further sterilized under UV light for 45 min, washed twice in phosphate-buffered saline (PBS), and finally immersed in a culture medium and incubated for 24 hours in a humidified 5% CO_2 incubator at 37 °C. hMSCs were seeded at a density of 1×10^5 cells per scaffold and cultured for 23 days to obtain bone ECM on the scaffold surface. Next, patient-derived breast cancer cells were seeded at a density of 1×10^5 cells per scaffold on the tissue-engineered bone and maintained in the breast cancer cells medium (Figure 2(A)). The media was changed every two days during both hMSCs and sequential culture of breast cancer cells on the scaffold surface.

4.2.4. Immunofluorescence staining

Both 8-well chambers (Thermo scientific) seeded, and scaffold seeded cells were washed twice in PBS and fixed in 4% paraformaldehyde (PFA) for 30 min. Next, cells were permeabilized with 0.2% TritonX-100 in PBS for 5 min, followed by blocking with blocking buffer (0.2% fish skin gelatin (FSG) with 0.02% Tween20) for 1 hour. Further, the cells were incubated with the primary antibody overnight at 4 °C. The primary antibodies were diluted in the blocking buffer using dilutions given in Table 4.1. Finally, cells were incubated with conjugated secondary antibodies corresponding to the species of used primary antibodies at 1:200 dilutions and incubated for 45 minutes at room temperature (RT). The nuclei were counterstained with 4,6- diamidino-2-phenylindole (DAPI), and immunofluorescence images were taken under a confocal microscope (Zeiss Axio Observer Z1 LSM 700).

Table 4.1. The details of primary antibodies used for immunofluorescence staining.

Primary Antibodies	Company	Catalog number	Dilutions
Progesterone	Cell signaling	8757S	1:800
Estrogen	Cell signaling	13258S	1:100
HER2	Cell signaling	2165S	1:100
E-Cadherin	Cell signaling	3195S	1:200
Vimentin	Abcam	ab8978	1:500
CK19	Abcam	ab52625	1:100
EpCAM	Abcam	ab71916	1:200

4.2.5. Gene expression by RT-qPCR

RNA was isolated from cells grown on TCPS (2D) and scaffolds using a Direct-zol RNA MiniPrep kit (Zymo Research) following the protocol described elsewhere [121]. Briefly, 1000 ng of RNA was reversed transcribed to cDNA using random primers and M-MLV reverse transcriptase (Promega) in a thermal cycler using a thermal profile- 70 °C for 5 minutes (Applied Biosystems). Next, the qPCR experiment was performed using a 7500 Fast Real-Time PCR instrument (Applied Biosystems) using a thermal profile with a holding stage (5 min at 95 °C) and a cycling stage (40 cycles of 30 s at 95 °C, and 1 min at 55 °C). The mRNA expressions of genes listed in Table 4.2 were quantified using their respective primers and normalized to the housekeeping gene glyceraldehyde-3-phosphate dehydrogenase (GAPDH). Finally, fold change in target gene expressions was calculated using the comparative Ct method ($2^{-\Delta\Delta Ct}$).

Table 4.2. The primer sequence used for the qRT-PCR experiment.

Gene	Forward Primer	Reverse Primer
GAPDH	5'-CAT CTT CTT TTG CGT CGC CA-3'	5'-TTA AAA GCA GCC CTG GTG ACC -3'
E-Cadherin	5'-AAG TGA CCG ATG ATG AT-3'	5'-CTC TGT CCA TCT CAG CG-3'
N-Cadherin	5'-AGG GTG GAC GTC ATT GTA GC-3'	5'-CTG TTG GGG TCT GTC AGG AT-3'
Wnt-5A	5′-TCT CAG CCC AAG CAA CAA GG-3′	5′-GCC AGC ATC ACA TCA CAA CAC-3′
β-catenin	5′-GGC AGC AAC AGT CTT ACC-3′	5′-TCC ACA TCC TCT TCC TCA-3′
VEGF	5'-GAC AAG AAA ATC CCT GTG GGC -3'	5'-AAC GCG AGT CTG TGT TTT TTG C -3'
OCN	5′-GTG ACG AGT TGG CTG ACC-3′	5′-TGG AGA GGA GCA GAA CTG G-3′

4.2.6. ELISA assays

Released DKK1 and ET-1 cytokines concentration was measured in serum-free cell culture media using high sensitivity ELISA kits of DKK1 (RayBiotech) and ET-1 (RayBiotech) according to the manufacturer's protocol. The cell-seeded scaffolds were kept in a serum-free medium for 48 hours before collecting the medium for sample preparation. Next, the medium was centrifuged at 350 x g for 10 minutes at 4 °C to remove cell debris, and supernatants were stored at −20 °C until analysis.

4.2.7. Statistical analysis

Data were presented as the mean value ± standard deviation. Statistical significance between two groups was determined by an unpaired Student's t-test or by one-way or two-way ANOVA followed by Tukey's post-test using GraphPad Prism v7.04 software. The level of significance was set at $p \leq 0.05$.

4.3. Results

4.3.1. Isolated patient-derived cancer cells retained their idiosyncratic characteristics

To identify that breast cancer cells isolated from patient tissue samples retained their tumor-associated features, we explored their characteristic proteins by immunostaining. Breast cancer cells are broadly classified into three categories- Hormone positive, triple-negative, and HER2 positive based on the expression of hormone receptors-estrogen (ER) and progesterone (PR) and human epidermal growth factor receptor 2 (HER2) [151]. After characterizing NT013 patient-derived cells, we observed that NT013 retained their hormone-positive characteristics by expressing ER. Interestingly, we also observed positive HER2 expression. However, other studies on NT013 patient tissue showed reduced HER2 levels (data not shown), suggesting that NT013 cells can be categorized into hormone-positive breast cancer cells. Next, we evaluated similar protein expression in NT023 cells and observed that NT023 cells do not express ER, PR, and HER2 receptors, retaining the triple-negative cells' characteristics.

Cytokeratin-19 (CK19) is also a suitable marker for identifying breast cancer cells [154, 155]. CK19 is an epithelial cell marker, and its expression was seen in more than 90% of breast cancer cases. It is also reported that luminal type hormonal positive cells exhibit higher positive rates of CK19 than triple-negative cells [155, 156]. We observed protein expression of CK19 in both cell lines; however, the expression was more intense in NT013 cells compared to NT023 cells. Next, we analyzed Epithelial to Mesenchymal transition (EMT) markers for NT013 and NT023 cells to identify their invasive nature. Epithelial cells can be identified by expressing the epithelial protein E-Cadherin on their cell surface. In contrast, mesenchymal cells can be identified by various protein expressions such as N-Cadherin, vimentin, and twist [42]. We observed that NT013 cells expressed both E-Cadherin and Vimentin protein expressions, while NT023 cells

mostly expressed high Vimentin levels, indicating that NT023 cells are more mesenchymal in nature compared to NT013 cells (Figure 4.1).

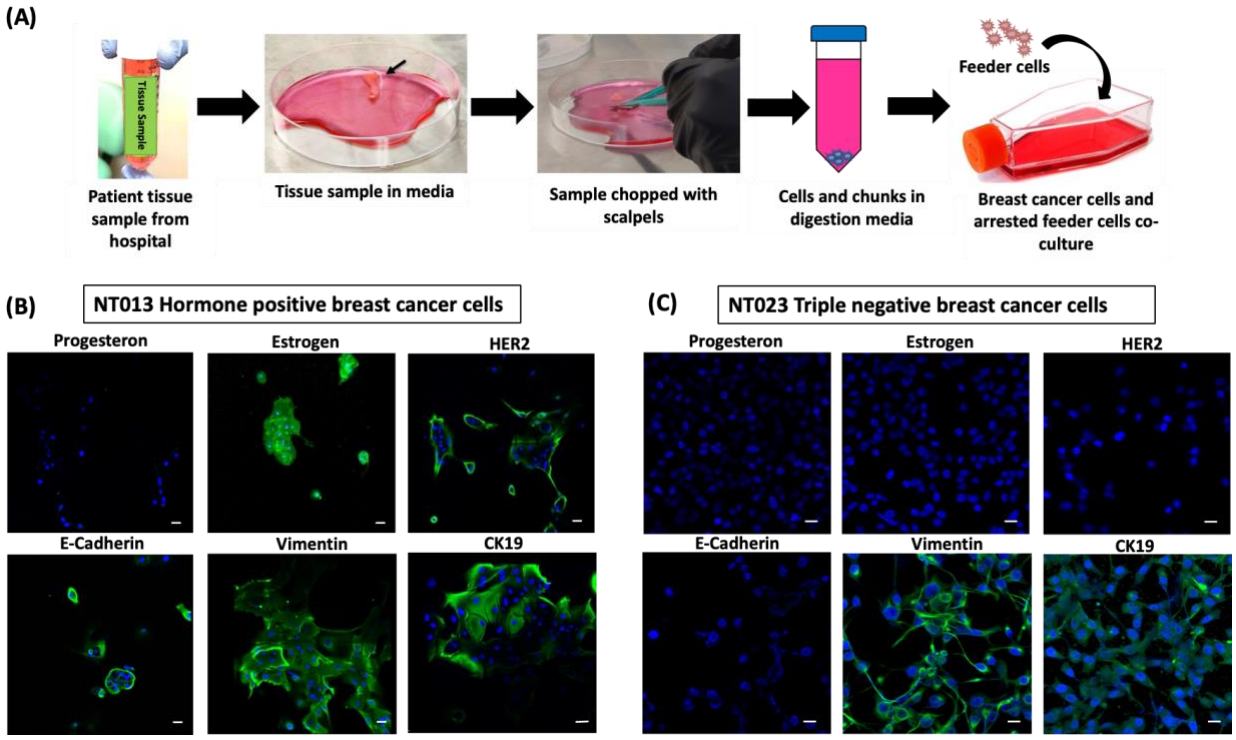

Figure 4.1. (A) Schematic showing isolation steps of breast cancer cells from the patient tissue sample. (B) Representative immunofluorescence microscope images of NT013 and NT023 cells cultured in 2D culture. Scale bar: 20 μm.

4.3.2. Bone microenvironment induced MET in breast cancer cells

EMT/MET processes represent the invasiveness of cancer cells where cancer cells leave their primary site and acquire migratory phenotype during EMT while MET potentiates cancer cells to regain their epithelial characteristics and adapt to the new environment at their secondary site [71, 120, 157]. To investigate the effect of the bone microenvironment on patient-derived breast cancer cells' invasiveness, we analyzed their mRNA levels related to EMT/MET biomarkers such as E-Cadherin and N-Cadherin and compared our results with cells grown on a 2D surface. E-cadherin is a cell surface protein that participates in forming homotypic junctions across epithelial cells [158]. The loss of E-cadherin, while the gain in N-cadherin levels is associated with

the EMT process of cancer cells [42] and vice-versa, is valid for the MET process [120]. Previously, we observed that the commercial breast cells - MCF-7 and MDAMB231 undergo mesenchymal to epithelial transition due to upregulation of E-Cadherin, and downregulation of vimentin and twist levels in the presence of bone. Likewise, we observed increased E-cadherin levels in NT013 (~ 2-fold) and NT023 (~ 4-fold) breast cancer cells grown in a bone microenvironment compared to their respective 2D cell cultures. We also observed downregulation in N-cadherin levels in NT013 cells while the insignificant change in N-cadherin levels in NT023 cells, indicating that both NT013 and NT023 cells acquired more epithelial characteristics in the bone microenvironment (Figure 4.2).

4.3.3. Bone microenvironment induces aggressiveness and angiogenesis in patient-derived cells

Wnt5a is an important member of the Wnt pathway and acts as either tumor-suppressive or tumor-promoting in different cancer types [159]. Lower levels of Wnt-5A expression are significantly associated with poor prognosis and more aggressive behavior of triple-negative breast cancer [160, 161]. Similarly, β-catenin is highly expressed in breast cancer patients [162] and is significantly associated with a poor clinical outcome in the invasive breast cancer [163]. To evaluate the aggressive behavior of breast cancer cells in the presence of bone, we quantified their Wnt-5A and β-catenin levels. Our results showed significant downregulation in Wnt-5A levels in NT023 growing on the bone compared to 2D culture while we didn't observe any significant change in Wnt-5A in NT013 cells. However, we observed significant upregulation in β-catenin levels in both NT023 and NT013 cells, indicating increased aggressiveness in the presence of bone.

VEGF is a well-known marker of angiogenesis, highly expressed in many solid tumors resulting in a poor prognosis of the disease [164] We observed upregulation in the VEGF mRNA

levels in both NT013 and NT023 cells grown on bone compared to their 2D cultures, respectively, indicating increased angiogenesis in both cell types in the presence of bone (Figure 4.2).

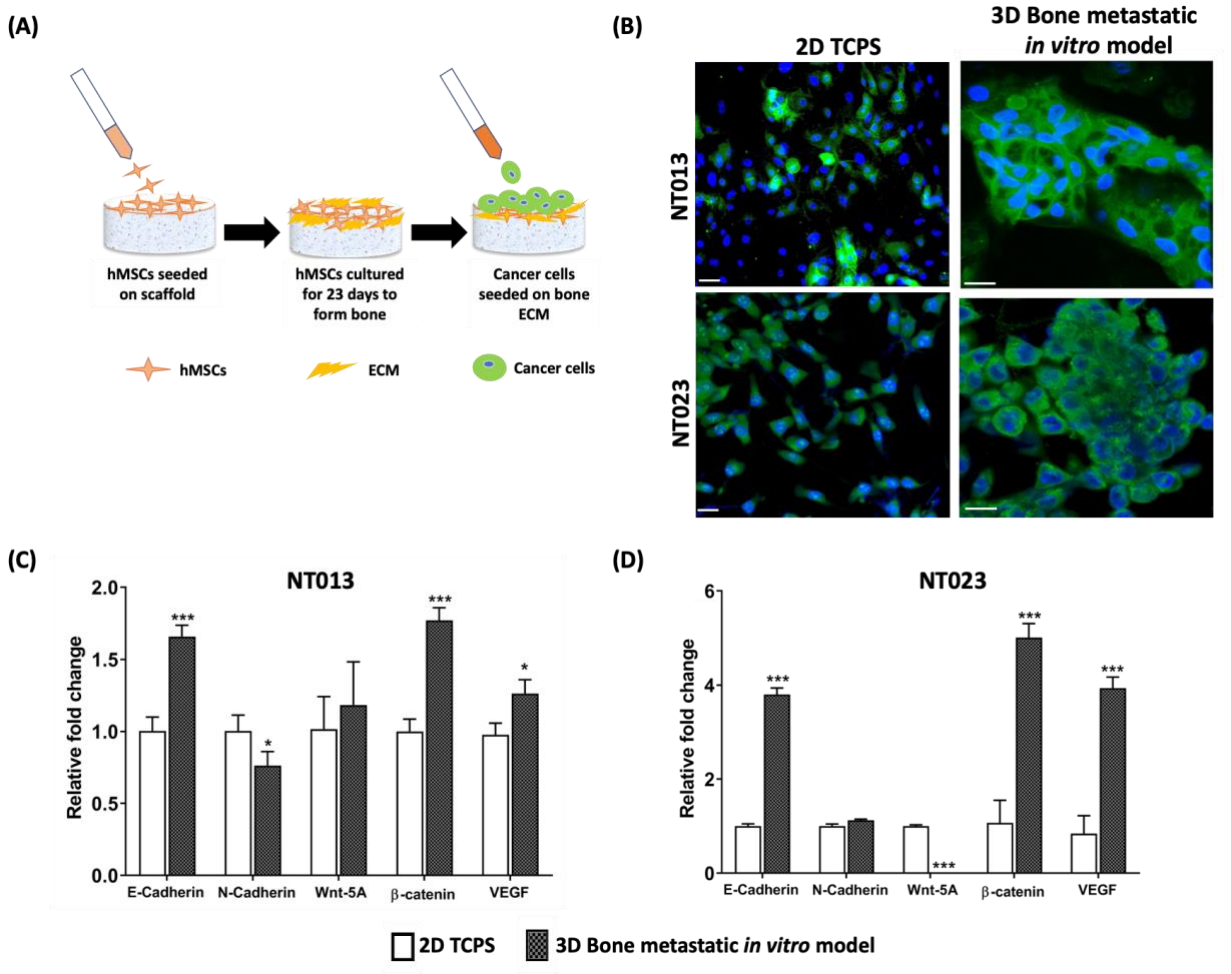

Figure 4.2. (A) Schematic showing steps of sequential culture. (B) Tumor morphology was determined by staining with EpCAM. Scale bar: 20 μm (C) Quantified gene expressions of E-Cadherin, N-Cadherin, Wnt-5A, β-catenin, and VEGF in NT013 cells under different conditions. (D) Quantified gene expressions of E-Cadherin, N-Cadherin, Wnt-5A, β-catenin, and VEGF in NT023 cells under different conditions.

4.3.4. Tumor formation by patient-derived cell lines on bone niche

To investigate the morphology of cancer cells on bone mimetic scaffolds after MET, we stained the cells with cancer-specific protein, EpCAM, and compared our results with cells grown on 2D surfaces. EpCAM is a transmembrane protein, overexpressed significantly in breast cancer tissues [165]. We observed that both NT013 and NT023 cell lines formed tumors on bone-mimetic

scaffolds. In contrast, cancer cells in their monoculture did not form any tumors. We also noticed that NT013 cells formed compact tumors on the bone microenvironment, exhibiting distinguishable cellular boundaries with strong cell-cell interactions, while NT023 cancer cells grouped into clusters instead of making compact tumors. Previously, we observed that hormone-positive MCF-7 cells formed dense tumoroids on bone scaffolds like NT013 breast cancer cells. In contrast, triple-negative MDA-MB 231 cells formed loose aggregates different from NT023 cells, indicating that inherent characteristic differences among two different triple-negative cells could alter their tumor-forming ability after interacting with the bone microenvironment.

4.3.5. DKK-1 and ET-1 factors released by breast cancer cells regulate the osteogenic Wnt/β-Catenin pathway

ET-1 and DKK1 are ideal markers to predict bone metastasis in breast cancer patients that induce osteoblastic or osteolytic lesions, respectively, resulting in the poor mechanical stability of the bone [166, 167]. It is reported that serum DKK1 levels were higher in patients with breast cancer metastasized to the bone than in other metastatic sites [168]. Previously, we observed that MCF-7 cells grown on bone, released high levels of ET-1 in serum-free media whereas MDAMB231 cells released high levels of DKK- 1, leading to stimulation and inhibition of osteogenesis, respectively, via the Wnt/β-catenin pathway. To investigate the effect of NT013 and NT023 released cytokines on bone health via Wnt signaling, we first quantified ET-1 and DKK-1 levels in the sequential culture of NT013 and NT023 and observed that NT013 cells released high levels of ET-1 while NT023 cells released high DKK-1 levels in-line with MCF-7 and MDAMB231 cells, respectively. Next, to determine that ET-1 and DKK-1 released by patient-derived cells are involved in the regulation of the Wnt/β-catenin signaling mediated bone osteogenesis, we analyzed the expressions of Wnt-related genes of MSCs on Day (23+10)

maintained under different mediums. We observed upregulation in both Wnt 5a and β-catenin expressions in hMSCs cultured with conditioned media of sequentially cultured NT013 cells containing high ET-1 levels. In contrast, hMSCs cultured with conditioned media of sequentially cultured NT023 cells containing high DKK-1 levels showed downregulation of Wnt 5a and β-catenin levels compared to control MSCs samples. We also assessed the expression of a late-stage osteogenic marker, OCN in hMSCs cultured under different conditioned media w.r.t to control sample. We noticed an increase in mRNA levels of OCN in hMSCs cultured with conditioned media of sequentially cultured NT013 cells while downregulation in OCN levels in hMSCs cultured with CM of sequentially cultured NT023 cells. Overall, the results suggested that NT013 cells stimulate Wnt/ β-catenin signaling in hMSCs while NT023 cells abrogate the Wnt/ β-catenin pathway, promoting and inhibiting osteogenesis, respectively (Figure 4.3).

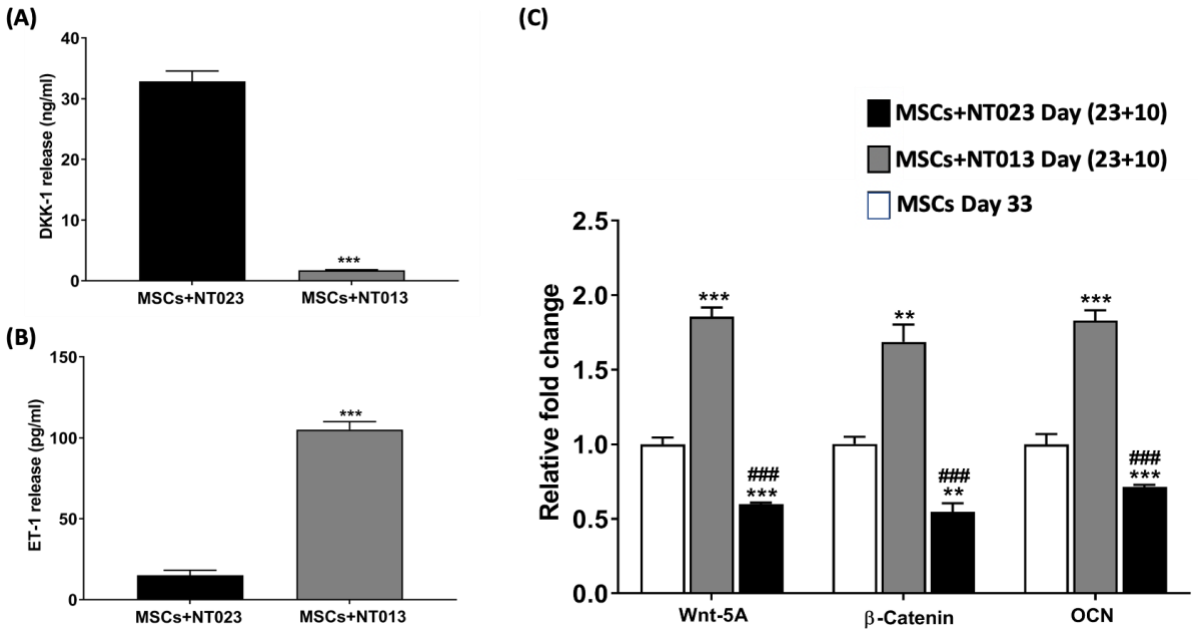

Figure 4.3. Breast cancer-released cytokines DKK-1 and ET-1 regulate Wnt/β-catenin pathway. (A) Quantified serum levels of DKK-1 and (B) ET-1 measured by ELISA ***$p < 0.001$ indicate significant difference between MSCs+NT023 and MSC+NT013 Day (23 + 10). (C) Quantified gene expressions of Wnt-5a, β-catenin, and OCN. **$p < 0.01$ and ***$p < 0.001$ indicate significant difference between MSCs cultured with MSC+NT013 Day (23 + 10) conditioned media and control MSCs Day-33. $^{###}p < 0.001$ indicate significant difference between MSCs cultured with MSC+NT023 Day (23 + 10) conditioned media and control MSCs Day-33.

4.4. Discussion

In the past decade, hundreds of 3D *in vitro* models have been developed to recapitulate the breast cancer bone metastasis disease conditions [117]. However, existing breast cancer bone metastatic models mimicked late-stage breast cancer by co-culturing breast cancer cells with osteoblast that do not resemble the ideal conditions of breast cancer metastasis to bone *in-vivo* [19, 169, 170]. In contrast, our 3D *in vitro* breast cancer bone metastatic model is an accurate picture of the late stage of breast cancer metastasis to the bone where hMSCs differentiated on nano clay-based scaffold along with calcium deposition [128] and collagen formation [60] to generate bone-like ECM to create a remodeling bone microenvironment for breast cancer metastasis. Previously, we have successfully developed a 3D *in vitro* bone metastatic model using commercial breast cancer cell lines-MCF-7 and MDAMB231[55]. Our results showed that MCF-7 and MDAMB231 breast cancer cells underwent MET and formed tumors in the bone microenvironment. Moreover, their interaction with bone cells induces the release of cytokines that further influence bone growth via the Wnt/β catenin pathway [153]. In the present study, we have validated our 3D *in vitro* breast cancer bone metastatic model using patient-derived breast cancer cells. NT013 breast cancer cells were characterized as hormone-positive cell lines while NT023 breast cancer cells were triple-negative. In line with our previous results, we observed the occurrence of MET in both patient-derived breast cell lines in the presence of bone due to upregulation in E-Cadherin while downregulation in N-cadherin levels. However, we also noticed a difference in fold change E-Cadherin levels in NT013 and NT023 breast cancer cells grown in the bone microenvironment. The possible reason for an extreme difference in fold change of E-Cadherin levels can be attributed to inherent low levels of E-Cadherin expression in NT023 that upregulated substantially in the presence of bone microenvironment. In contrast, NT013 cells inherently exhibit a high E-cadherin

expression; thus, fold change was not so high. MDAMB231 cells also express low E-Cadherin levels inherently [171]. Previously we observed that MDAMB231 cells formed loose aggregates on the bone microenvironment because fold change in upregulated E-cadherin levels was not so high [153] while NT023 cells formed clustered tumors on the bone microenvironment, suggesting that due to the extreme increase in E-cadherin levels in NT023 cells on the bone stimulate them to form tumors due to strong cell-cell interactions.

Wnt/β catenin pathway has been well-known for regulating bone formation *in vivo* and osteoblast differentiation *in vitro* [172, 173]. Our results showed that excessive release of ET-1 by NT013 cells and DKK-1 release by NT023 cells stimulated and abrogated the Wnt/β catenin pathway, respectively. Our results are in good agreement with our previous studies [153] and reported literature [166, 167]. We have also demonstrated upregulation in OCN levels in the presence of ET-1, resulting in osteoblastic metastases by NT013 cells while downregulation in OCN levels due to the inhibitory effect of DKK-1 on osteoblast differentiation, in line with our results with commercial cell line [153] and reported studies on bone formation *in vivo* [167, 174-176].

Taken together, our result from the present study complies well with our previous studies thus, validating our 3D *in vitro* bone metastatic model. This novel 3D *in vitro* disease model of breast cancer provides a unique microenvironment for the physiological cell-cell and cell-ECM interactions, thus, useful for better predicting the pathogenesis of cancer cells and more accurate measurement of potential drugs.

4.5. Conclusion

A better understanding of complex interactions between breast cancer cells and the bone microenvironment is of paramount importance for improving the outcome of late-stage breast

cancer patients. One of the utmost challenges associated with poor prognosis is the lack of reliable models for studying breast cancer at its advanced stage. The present study validated our 3D *in vitro* bone metastatic model using patient-derived breast cancer cell lines, previously developed using commercial cell lines. We demonstrated that patient-derived breast cancer cells retained their idiosyncratic characteristics after isolating using the most efficient method for cancer cell isolation from solid tumors. The model was able to mimic the MET process of breast cancer metastasis and revealed mixed bone lesions with breast cancer cell lines of different characteristics, mimicking bone lesions observed in breast cancer patients in their late stages. The developed 3D *in vitro* breast cancer models using patient-derived cells could recapitulate the metastatic ability of breast cancer cells to bone, thus could be utilized as a viable tool for future breast cancer studies and novel drug screening.

5. VALIDATING THE EFFECT OF FLUID-DERIVED SHEAR STRESS ON CELLULAR RESPONSE IN PERFUSION BIOREACTOR BY COMPUTATIONAL FLUID DYNAMICS (CFD) ANALYSIS[4]

This chapter describes the correlation between experiments conducted in the perfusion bioreactor and computational fluid dynamics. The contents of this chapter have been submitted for publication.

5.1. Introduction

Prostate cancer is the most common cancer in men with a high malignancy rate. The American cancer society has estimated 191,930 new cases of prostate cancer and 33,330 deaths due to prostate cancer in 2020 [37]. Among them, about 80 percent of advanced prostate cancer patients are believed to develop bone metastases. The metastasized prostate cancer cells mainly spread to the axial skeleton, such as the spine and pelvic bones, leading to skeletal-related defects [92]. Previous studies suggest a strong connection between mechanical cues generated by interstitial fluid flow around the bone with alteration in the bone remodeling process and increased migration of cancer cells [91].

Various studies have been reported to determine fluid-derived shear stress and its responses *in vitro*. For instance, recent studies have demonstrated enhanced extracellular matrix generation by osteoblast cells with an increased flow rate from 0.3 ml/min to 3 ml/min on fiber mesh titanium scaffolds [89]. In another study, researchers observed substantial cell death of MC3T3-E1 osteoblast-like cells at a flow rate of 1.0 ml/min that was grown on decellularized trabecular bone scaffolds.

[4]This chapter was co-authored by Haneesh Jasuja, Lahcen Akerkouch, D.R. Katti, K.S. Katti and Trung Bao Le. Haneesh Jasuja had the primary responsibility for preparing samples, conducting all tests and drafting this chapter. Trung Bao Le, Kalpana Katti, and Dinesh Katti directed the research orientation and revised this chapter. Lahcen Akerkouch performed the CFD analysis

On the contrary, cell viability was observed to increase at a lower flow rate [177]. Thus, it is apparent that there are some other critical factors (such as scaffold pore size, and interconnectivity) rather than flow rate alone that may influence the rate of shear stress. Here, computational fluid dynamics (CFD) may act as a beneficial tool to gain a better insight into the influence of mechanical forces generated by the fluid flow on the cellular response.

In the present study, we aimed to predict the rate of shear stress generated by fluid flow at different regions of a scaffold using CFD analysis that influences human mesenchymal stem cells and prostate cancer response in terms of growth rate and orientation compared to static culture.

5.2. Materials and methods

5.2.1. Preparation of the PCL/in-situ HAP clay scaffolds

The scaffolds were prepared as per the protocol described in our prior studies. Briefly, sodium montmorillonite (Na-MMT) clay was modified with 5-aminovaleric acid modifiers to increase the d-spacing between clay sheets. Next, hydroxyapatite (HAP) was intercalated into the galleries of modified clay to form in situ, HAP Clay. The scaffolds were prepared using the freeze-drying method by mixing polycaprolactone (PCL) polymer and 10 wt% in-situ HAP Clay. The scaffold dimensions used during experiments were 12 mm in diameter and 3 mm in thickness.

5.2.2. Bioreactor setup

The bioreactor chambers and their components were designed using Solid Works software and fabricated using Formlabs Form 2, 3D Printer, described in detail in our previous work [121]. Briefly, the chambers were connected to the flow-regulated pump and media bottles by silicone tubing (Peroxide-Cured Silicone, ID 1.42 mm, Ismatec). The flow rate was maintained at 0.2 mL/min during the experiments. The bioreactor chambers and media bottles were placed inside

the incubator to maintain optimum conditions for cell survival (37 C, 5% CO_2, high moisture) (Figure 5.1).

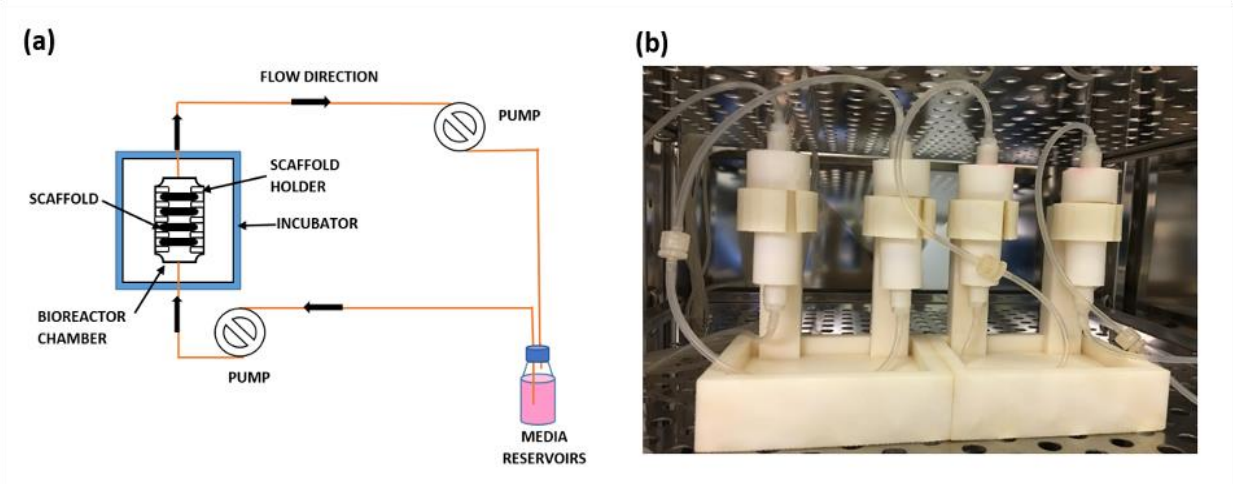

Figure 5.1. (a) Schematic showing bioreactor components and the direction of media flow through the bioreactor chambers. (b) Bioreactor setup inside the incubator.

5.2.3. Cell culture and seeding

Human mesenchymal stem cells (hMSCs) (Lonza, PT-2501) were cultured in an MSCGM Bullet kit medium (Lonza, PT-3001). $5x10^5$ hMSCs were seeded on each scaffold and maintained under static and dynamic conditions for a period of 23 days. Media was changed every 2 days for static cultures and every 3 days for dynamic cultures. Human prostate cancer (PCa) cell line MDAPCa2b (ATCC® CRL-2422TM) was cultured in media comprised of 80% BRFF-HPC1 (AthenaES, 0403), 20% fetal bovine serum (FBS) (ATCC, 30-2020), and 1% Penicillin–Streptomycin (Gibco). After 23 days, $1x\ 10^5$ PCa cells were seeded on each tissue-engineered bone scaffold and maintained under static and dynamic conditions. hMSCs and PCa media were utilized in a 1:1 ratio after the PCa cells seeding step.

5.2.4. Live-dead assay and DAPI staining

The viability of hMSCs was examined by live/dead staining (Biotium, 30002-T). The scaffolds containing hMSCs at different time points (Day-0, Day-10, and Day-23) under both

conditions were rinsed twice with PBS. Next, the scaffolds were incubated in a solution containing 2 μM calcein AM and 4 μM Ethidium Homodimer III (EthD-III) in PBS for 30 min at room temperature for staining live cells and dead cells, respectively as per the manufacturer's protocol. The scaffolds were imaged under Zeiss Axio Observer Z1 LSM 700 confocal microscope using Ex/Em wavelengths described in the manufacturer's protocol.

To assess the distribution of hMSCs on the scaffold surface, all four scaffold samples were retrieved from the bioreactor chamber and the cells were fixed using a 4% paraformaldehyde solution. Next, the cells were counterstained with 4,6- diamidino-2-phenylindole (DAPI), and images were taken under a Zeiss Axio Observer Z1 LSM 700 confocal microscope.

5.2.5. Micro-CT sample preparation and imaging

Scaffold samples were scanned for micro-CT imaging under for micro-CT scanner (GE Phoenix vltomel xs X-ray computed tomography system) with an 80 kV X-ray energy source and 350 μA current intensity with a molybdenum target. Scans were performed at multiple detector exposure times of 200 ms, 500 ms, 1000 ms, and 2000 ms, and the final image was reconstructed using a 500 ms detector timing. Sample magnification was carried out with a voxel size of 15.51 μm. The volume of interest selected for the scaffold was 12 mm in diameter and 3 mm in thickness.

5.2.6. Scanning electron microscopy (SEM)

The samples containing hMSCs and sequentially cultured PCa cells were retrieved from both culturing conditions on day 23 and day (23+10), respectively, and washed twice with PBS. Further, the cells on scaffolds were fixed with 2.5% glutaraldehyde overnight at 4°C. Next, the cells were dehydrated with ethanol series (30%, 50%, 70%, 90%, and 100%), and scaffolds were dried using hexamethyldisilazane. The dried scaffolds were sputter-coated with gold and mounted on SEM stubs for scanning under a scanning electron microscope (JEOL JSM-6490LV).

5.3. Results

5.3.1. Uniform cell distribution in all four scaffolds under flow conditions

To evaluate the orientation and viability of hMSCs under dynamic and static conditions, we stained the cells with live-dead staining and observed that almost all the cells were alive over a period of 23 days. In addition, we observed that hMSCs under dynamic conditions gained some directional orientation compared to hMSCs under a static culture where cells were randomly distributed on the scaffold surface (Figure 5.2 (c-d)). Next, to evaluate the distribution of cells on all four scaffolds in the perfusion bioreactor, we stained the nuclei of hMSCs with DAPI and observed that hMSCs were uniformly dispersed in all four scaffolds (Figure 5.2 (a-b)). Based on these results, we decided to choose one scaffold for CFD analysis.

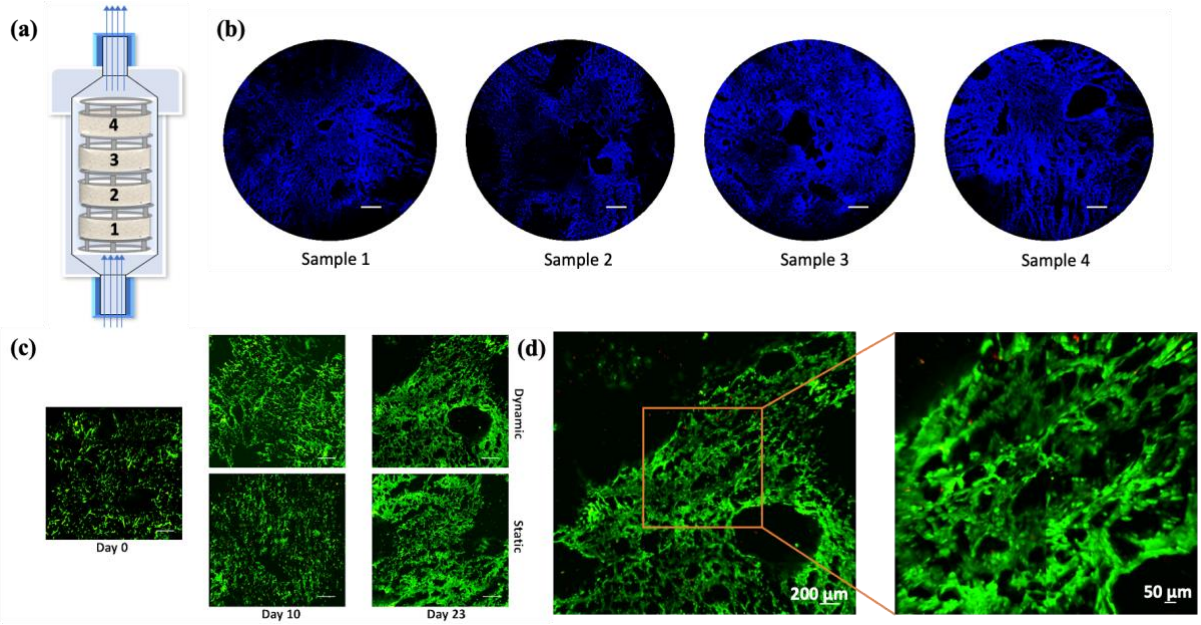

Figure 5.2. (a) The schematic showing the flow direction of media through a bioreactor accommodates four scaffold samples. (b) DAPI Stained human mesenchymal stem cells (hMSCs) nucleus representing the distribution of cells on nano clay-based scaffold grown under dynamic conditions on day 23. Scale: 1 mm (c) Live dead assay represents the viability of hMSCs over 23 days under static and dynamic conditions. Scale: 400 µm. (d) partial close-up view of hMSCs grown on the scaffold on day-23.

Next, we scanned the scaffold to obtain its micro-CT image. The micro-CT image of the scaffold in Figure 5.3 showed that the scaffold possesses interconnected porosities necessary for fluid flow through scaffolds. Previously, our research group also calculated scaffold's porosity and found that nanoclay-based scaffolds are highly porous in nature (86.1%).

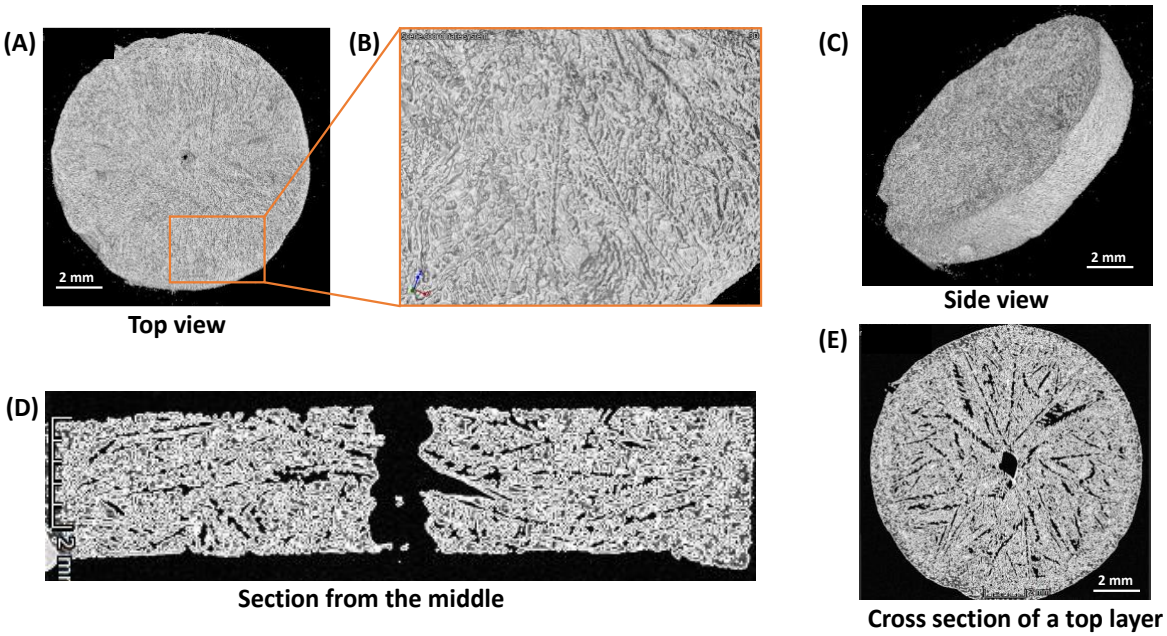

Figure 5.3. Micro-CT of the scaffold. (A-B) Top view of scaffold and partial close-up view. (C) Side view of the scaffold. (D) Section of the scaffold from the middle. (E) Cross-section of a top layer of the scaffold.

5.4. Discussion

Previously, we developed a 3D *in vitro* dynamic model using a 3D printing technique, where the cancer cells were seeded on the bone mimetic scaffolds in the perfusion bioreactor to recapitulate late stage of prostate cancer progression at the bone site under interstitial fluid flow[3]. We observed a significant change in the growth, orientation, and gene expression of both mesenchymal stem cells and prostate cancer cells cultured under fluid flow conditions compared to static culture (Figures 5.4 & 5.5). However, to understand the correlation between velocity distribution of the fluid flow inside the scaffold and to evaluate the magnitude of fluid derived shear stress affecting characteristic changes in cell orientation and gene expression, we performed

a series of CFD simulations using a full-scale 3D surface mesh of the realistic scaffold using its micro-CT scans.

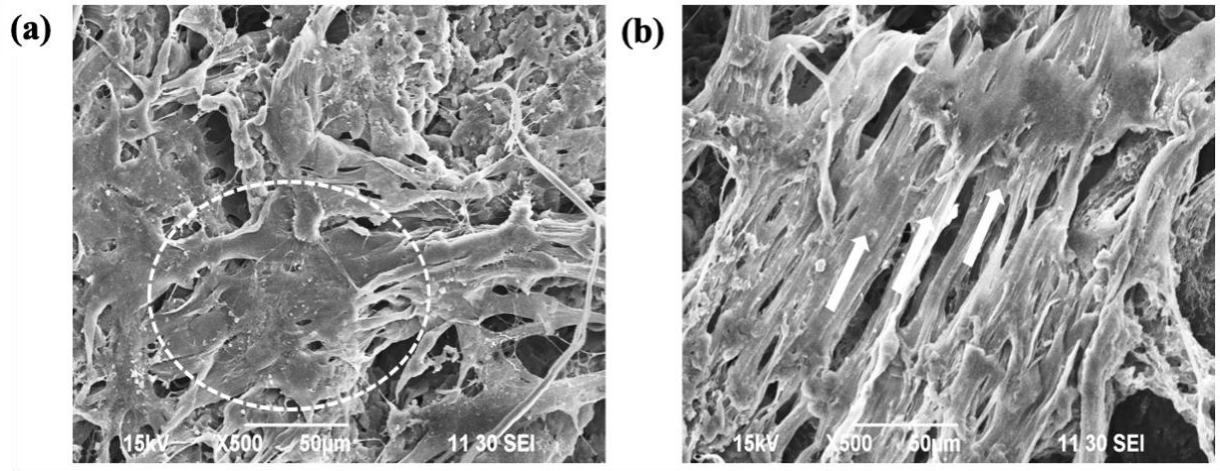

Figure 5.4. (a) SEM data represents the random distribution of hMSCs under static culture on day 23. (b) SEM data represents the directional alignment of hMSCs under dynamic culture on day 23.

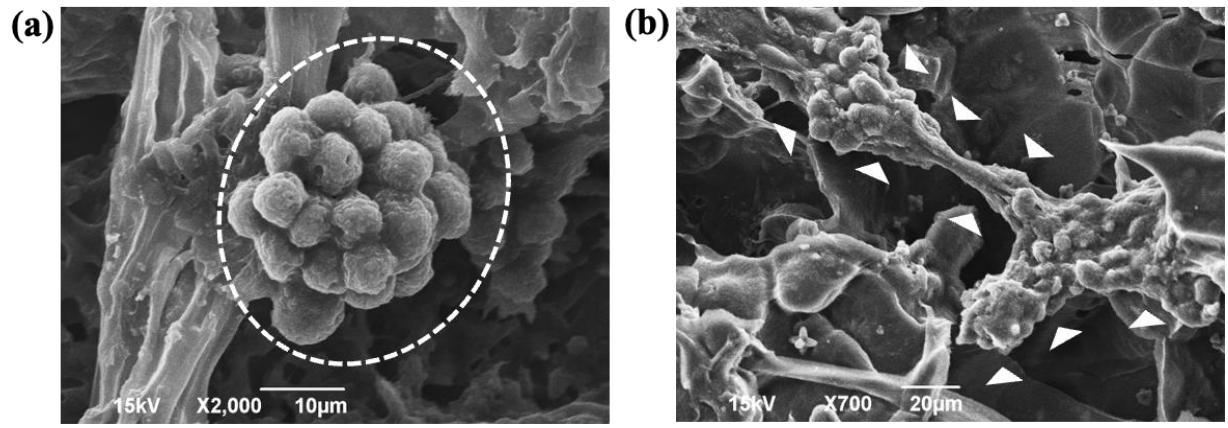

Figure 5.5. SEM data of hMSCs + MDAPCa2b sequential culture at day (23 + 10) represents morphological variations of prostate cancer cells. (a) under static culture. (b) under dynamic culture. Arrow indicates the location of tumor cells in the micrograph.

5.5. Conclusion

In the present study, we have investigated the shear stress distribution and its magnitude within scaffold in the perfusion bioreactor using CFD analysis that influences cellular response. It is collaborative work, so we have presented the experimental part performed by our group.

6. SUMMARY AND CONCLUSIONS

In this dissertation, we have reported the successful development of two different 3D *in vitro* dynamic models to recapitulate bone metastatic prostate cancer behavior under dynamic conditions. First, we developed a perfusion bioreactor to investigate the critical role of fluid-derived shear stress on the growth and differentiation of hMSCs and prostate cancer progression to bone. Overall, our results indicate that shear stress promotes hMSCs proliferation, differentiation, and morphological variations. We report that fluid-derived shear stress has a massive impact on hMSC cell morphology. The hMSCs under static culture form cell agglutinates, whereas, under dynamic culture, the cells exhibited a directional alignment with broad and flattened morphology. The fluid flow enabled shear stress significantly influences MET biomarkers (E-cadherin and vimentin) and the cell shape of prostate cancer cells at the metastatic bone site. Our prior studies suggest variation in morphologies between two prostate cancer cell lines under static conditions, with MDAPCa2b cells forming tight dense tumoroids and PC3 cells forming loose aggregates [56]. In comparison, the application of shear stress in the dynamic experiments largely impacted prostate cancer cell morphology. The dynamic MDAPCa2b prostate cancer cells formed highly compact morphology as early as a day (23+10), and the PC3, unlike the loose aggregates under static conditions, exhibited cell colonization at day (23+10). Using the 3D metastasis testbed, we demonstrate FAK activation in assembling integrin molecules in proximity via a focal adhesion complex. Evaluation of cell adhesion proteins indicated that the cause of variation in cancer cell morphology under shear stresses arises from the constant force pulling due to increased E-cadherin and phosphorylated Focal adhesion kinase (FAK) proteins under the fluid flow enabled shear stress.

To better understand the migration behavior of prostate cancer at their extravasation stage and the critical role of fluid shear stress influencing migration rate we developed a horizontal bioreactor integrated with a transwell insert. Our findings suggest that interstitial flow-induced shear stress could be a critical factor in regulating the migration of prostate cancer cells at their extravasation stage. In the present study, we observed that the fluid flow rate corresponding to the physiological velocity of the interstitial fluid is optimum for better cell growth compared to a high flow rate, where we observed suppression in the growth rate of PC3 cells due to induction in apoptosis. Thus, we investigated the effect of physiological fluid velocity on the migration rate of PC3 cells and demonstrated that fluid shear stress contributed to an increased migration rate of PC3 cells via increased expression of αvβ3 integrins that further activate downstream signaling leading to an increase in MMP-9 levels. It is well accepted that fluid flow-derived shear stress is a fundamental determinant of cell behavior regulating tumor biology. Thus, our results could be considered in controlling tumor progression and developing new inhibitors. The novel bioreactors we developed could be utilized for understanding the growth and migration of different cancer types in the future.

In this dissertation, we also validated our 3D *in vitro* bone metastatic breast cancer model with patient-derived cells to better understand complex interactions between breast cancer cells and the bone microenvironment for improving the outcome of late-stage breast cancer patients. We demonstrated that patient-derived breast cancer cells retained their idiosyncratic characteristics after isolating using the most efficient method for cancer cell isolation from solid tumors. The model was able to mimic the MET process of breast cancer metastasis and revealed mixed bone lesions with breast cancer cell lines of different characteristics, mimicking bone lesions observed in breast cancer patients in their late stages. The developed 3D *in vitro* breast cancer models using

patient-derived cells could recapitulate the metastatic ability of breast cancer cells to bone, thus could be utilized as a viable tool for future breast cancer studies and novel drug screening.

In this dissertation, we also investigated the role of shear stress in perfusion bioreactor using utilizing computational fluid dynamics (CFD) to establish a correlation between fluid shear stress and metastasis progression. The CFD analysis was performed by our collaborator group however, for understanding the better correlation between experiments and CFD, we performed some experiments using a perfusion bioreactor.

7. FUTURE DIRECTION

This dissertation has reported the advancement in prostate and breast cancer bone metastatic 3D models developed by our research group using a tissue-engineering approach that recapitulates metastasis of prostate and breast cancer to bone at their advanced stages. This 3D *in vitro* cancer testbed serves as a platform for better crosstalk between bone and metastasized cancer. In this dissertation, we have introduced a dynamic condition for cells by developing a bioreactor system that allows continuous media flow that closely resembles interstitial fluid flow *in vivo.* Thus, we advance our model into a complex system where cells experience fluid shear stress by continuous fluid flow.

- In Chapters 2 and 3, we have reported the development of two bioreactor models to understand the effect of fluid shear stress on the progression of prostate cancer at the bone site. These studies helped us understand the role of fluid shear stress on the phenotypic switch of prostate cancer cells and their enhanced migration rate. Mimicking the initial stages of prostate cancer growth by co-culturing normal prostate cells and prostate cancer cells onto a 3D testbed and connecting the initial stage with the metastatic stage via bioreactor might further help us understand the cascade of prostate cancer metastasis, including the complex EMT-MET process.
- Circulating tumor cells (CTCs) are also well-known for their role in the progression of all cancers. It is suggested that patients with a persistent increase in CTCs in their blood exhibited less overall survival. Thus, CTCs are also known as the gold standard for monitoring disease progression and act as a predictor for poor outcomes. In this dissertation, we have reported a novel design of bioreactor called “horizontal bioreactor,” and bridging primary and secondary sites via bioreactor will also help us

understand the role of fluid shear stress on the behavioral changes in CTCs. CTCs can be isolated from the continuously circulating media in this novel bioreactor system. Evaluating CTCs RNA by qPCR under dynamic conditions might help us understand the possible reason behind their polarity towards secondary sites.

- Real-time monitoring is an advanced approach to monitoring cancer growth over a more extended period by quantifying the cytokines released during their progression. Previously, we evaluated the levels of released cytokines by cancer cells in the media under static conditions using ELISA. However, released cytokines by cancer cells also start circulating in the media under dynamic conditions. Thus, sampling out media every day and quantifying the cytokine levels might help us monitor the cancer growth resembling *in vivo* tumor growth monitoring from blood tests. At the same time, testing different drugs during real-time monitoring might also help us predict possible therapeutics to treat cancer during its progression.
- This dissertation has reported mimicking the last stage of prostate and breast cancer bone metastasis using sequential culturing of mesenchymal stem cells and cancer cells in a 3D testbed under dynamic culture. Though our system exhibits sufficient complexity that closely resembles the *in vivo* system, complexity can be further increased by introducing critical components that play crucial roles in regulating metastatic progressions, such as immunological, hematopoietic, and vascular components.
- In this dissertation, we have reported the isolation of breast cancer cells from the patient tissue and evaluated their phenotypic switch in the presence of mesenchymal stem cells obtained from the Lonza company. However, incorporating patient-derived bone cells

in this 3D testbed would create a metastatic bone site that closely mimics the patient's bone. This might help us better understand the critical interaction between bone cells and breast cancer cells specific to the patient and predict possible outcomes.

REFERENCES

[1] Siegel R L, Miller K D, Fuchs H E and Jemal A 2021 Cancer statistics, 2021 *CA: a cancer journal for clinicians* **71** 7-33

[2] Gandaglia G, Abdollah F, Schiffmann J, Trudeau V, Shariat S F, Kim S P, Perrotte P, Montorsi F, Briganti A and Trinh Q D 2014 Distribution of metastatic sites in patients with prostate cancer: a population-based analysis *The Prostate* **74** 210-6

[3] Gandaglia G, Karakiewicz P I, Briganti A, Passoni N M, Schiffmann J, Trudeau V, Graefen M, Montorsi F and Sun M 2015 Impact of the site of metastases on survival in patients with metastatic prostate cancer *European urology* **68** 325-34

[4] Paget S 1889 The distribution of secondary growths in cancer of the breast *The Lancet* **133** 571-3

[5] Ewing J 1928 A treatise on tumors *Neoplastic disease*

[6] Bubendorf L, Schöpfer A, Wagner U, Sauter G, Moch H, Willi N, Gasser T C and Mihatsch M J 2000 Metastatic patterns of prostate cancer: an autopsy study of 1,589 patients *Human pathology* **31** 578-83

[7] Wolanczyk M J, Fakhrian K and Adamietz I A 2016 Radiotherapy, bisphosphonates and surgical stabilization of complete or impending pathologic fractures in patients with metastatic bone disease *Journal of Cancer* **7** 121

[8] Drake M T, Clarke B L and Khosla S 2008 Bisphosphonates: mechanism of action and role in clinical practice. In: *Mayo Clinic Proceedings*: Elsevier) pp 1032-45

[9] Jackson C, Freeman A L, Szlamka Z and Spiegelhalter D J 2021 The adverse effects of bisphosphonates in breast cancer: A systematic review and network meta-analysis *PloS one* **16** e0246441

[10] Prommer E 2015 Palliative oncology: denosumab *American Journal of Hospice and Palliative Medicine®* **32** 568-72

[11] Bolla M, Collette L, Blank L, Warde P, Dubois J B, Mirimanoff R-O, Storme G, Bernier J, Kuten A and Sternberg C 2002 Long-term results with immediate androgen suppression and external irradiation in patients with locally advanced prostate cancer (an EORTC study): a phase III randomised trial *The Lancet* **360** 103-8

[12] Simos D, Addison C L, Kuchuk I, Hutton B, Mazzarello S and Clemons M 2013 Bone-targeted agents for the management of breast cancer patients with bone metastases *Journal of clinical medicine* **2** 67-88

[13] Beer T M, Armstrong A J, Rathkopf D E, Loriot Y, Sternberg C N, Higano C S, Iversen P, Bhattacharya S, Carles J and Chowdhury S 2014 Enzalutamide in metastatic prostate cancer before chemotherapy *New England Journal of Medicine* **371** 424-33

[14] Gilligan T and Kantoff P W 2002 Chemotherapy for prostate cancer *Urology* **60** 94-100

[15] Fitzgerald K A, Guo J, Raftery R M, Castaño I M, Curtin C M, Gooding M, Darcy R, O'Brien F J and O'Driscoll C M 2016 Nanoparticle-mediated siRNA delivery assessed in a 3D co-culture model simulating prostate cancer bone metastasis *International journal of pharmaceutics* **511** 1058-69

[16] Fang X, Sivanandane S, Gyabaah K and Balaji K 2013 Novel 3D co-cultural model for epithelial-stromal cells interaction in prostate cancer. AACR)

[17] Florczyk S J, Liu G, Kievit F M, Lewis A M, Wu J D and Zhang M 2012 3D porous chitosan–alginate scaffolds: a new matrix for studying prostate cancer cell–lymphocyte interactions in vitro *Advanced healthcare materials* **1** 590-9

[18] Kwon H, Kim H J, Rice W L, Subramanian B, Park S H, Georgakoudi I and Kaplan D L 2010 Development of an in vitro model to study the impact of BMP-2 on metastasis to bone *Journal of Tissue Engineering and Regenerative Medicine* **4** 590-9
[19] Talukdar S and Kundu S C 2013 Engineered 3D silk-based metastasis models: Interactions between human breast adenocarcinoma, mesenchymal stem cells and osteoblast-like cells *Advanced functional materials* **23** 5249-60
[20] Subia B, Dey T, Sharma S and Kundu S C 2015 Target specific delivery of anticancer drug in silk fibroin based 3D distribution model of bone–breast cancer cells *ACS applied materials & interfaces* **7** 2269-79
[21] Zhu W, Holmes B, Glazer R I and Zhang L G 2016 3D printed nanocomposite matrix for the study of breast cancer bone metastasis *Nanomedicine: Nanotechnology, Biology and Medicine* **12** 69-79
[22] Sandri G, Bonferoni M, Rossi S, Ferrari F, Aguzzi C, Viseras C and Caramella C 2016 *Wound Healing Biomaterials*: Elsevier) pp 385-402
[23] Sikdar D, Pradhan S M, Katti D R, Katti K S and Mohanty B 2008 Altered phase model for polymer clay nanocomposites *Langmuir* **24** 5599-607
[24] Ambre A, Katti K S and Katti D R 2011 In situ mineralized hydroxyapatite on amino acid modified nanoclays as novel bone biomaterials *Materials Science and Engineering: C* **31** 1017-29
[25] Ambre A H, Katti D R and Katti K S 2015 Biomineralized hydroxyapatite nanoclay composite scaffolds with polycaprolactone for stem cell-based bone tissue engineering *Journal of Biomedical Materials Research Part A* **103** 2077-101
[26] Sharma A, Payne S, Katti K S and Katti D R 2015 Evaluating molecular interactions in polycaprolactone-biomineralized hydroxyapatite nanocomposites using steered molecular dynamics *Jom* **67** 733-43
[27] Katti K S, Ambre A H, Payne S and Katti D R 2015 Vesicular delivery of crystalline calcium minerals to ECM in biomineralized nanoclay composites *Materials Research Express* **2**
[28] Kar S, Jasuja H, Katti D R and Katti K S 2019 Wnt/β-Catenin Signaling Pathway Regulates Osteogenesis for Breast Cancer Bone Metastasis: Experiments in an In Vitro Nanoclay Scaffold Cancer Testbed *ACS Biomaterials Science & Engineering*
[29] Bixel M G, Kusumbe A P, Ramasamy S K, Sivaraj K K, Butz S, Vestweber D and Adams R H 2017 Flow dynamics and HSPC homing in bone marrow microvessels *Cell reports* **18** 1804-16
[30] Gromov P, Gromova I, Olsen C J, Timmermans-Wielenga V, Talman M-L, Serizawa R R and Moreira J M 2013 Tumor interstitial fluid—A treasure trove of cancer biomarkers *Biochimica et Biophysica Acta (BBA)-Proteins and Proteomics* **1834** 2259-70
[31] Boucher Y, Baxter L T and Jain R K 1990 Interstitial pressure gradients in tissue-isolated and subcutaneous tumors: implications for therapy *Cancer research* **50** 4478-84
[32] Avraham-Chakim L, Elad D, Zaretsky U, Kloog Y, Jaffa A and Grisaru D 2013 Fluid-flow induced wall shear stress and epithelial ovarian cancer peritoneal spreading *PloS one* **8** e60965
[33] Chang S-F, Chang C A, Lee D-Y, Lee P-L, Yeh Y-M, Yeh C-R, Cheng C-K, Chien S and Chiu J-J 2008 Tumor cell cycle arrest induced by shear stress: Roles of integrins and Smad *Proceedings of the National Academy of Sciences* **105** 3927-32

[34] Shields J D, Fleury M E, Yong C, Tomei A A, Randolph G J and Swartz M A 2007 Autologous chemotaxis as a mechanism of tumor cell homing to lymphatics via interstitial flow and autocrine CCR7 signaling *Cancer cell* **11** 526-38
[35] Shieh A C, Rozansky H A, Hinz B and Swartz M A 2011 Tumor cell invasion is promoted by interstitial flow-induced matrix priming by stromal fibroblasts *Cancer research* **71** 790-800
[36] Munson J M, Bellamkonda R V and Swartz M A 2013 Interstitial flow in a 3D microenvironment increases glioma invasion by a CXCR4-dependent mechanism *Cancer research* **73** 1536-46
[37] Siegel R L, Miller K D and Jemal A 2020 Cancer statistics, 2020 *CA: A Cancer Journal for Clinicians* **70** 7-30
[38] Howlader N, Noone AM, Krapcho M, Miller D, Brest A, Yu M, Ruhl J, Tatalovich Z, Mariotto A, Lewis DR, Chen HS, Feuer EJ and KA C 2019 SEER cancer statistics review, 1975–2016. 2018 *Bethesda, MD: National Cancer Institute*
[39] Paget S 1889 The distribution of secondary growths in cancer of the breast *Lancet* 571-3
[40] Saad F, Sternberg C N, Mulders P F A, Niepel D and Tombal B F 2018 The role of bisphosphonates or denosumab in light of the availability of new therapies for prostate cancer *Cancer treatment reviews* **68** 25-37
[41] Edmondson R, Broglie J J, Adcock A F and Yang L 2014 Three-dimensional cell culture systems and their applications in drug discovery and cell-based biosensors *Assay and drug development technologies* **12** 207-18
[42] Fontana F, Raimondi M, Marzagalli M, Sommariva M, Limonta P and Gagliano N 2019 Epithelial-to-mesenchymal transition markers and CD44 isoforms are differently expressed in 2D and 3D cell cultures of prostate cancer cells *Cells* **8** 143
[43] Talukdar S, Mandal M, Hutmacher D W, Russell P J, Soekmadji C and Kundu S C 2011 Engineered silk fibroin protein 3D matrices for in vitro tumor model *Biomaterials* **32** 2149-59
[44] McGovern J A, Shafiee A, Wagner F, Lahr C A, Landgraf M, Meinert C, Williams E D, Russell P J, Clements J A and Loessner D 2018 Humanization of the prostate microenvironment reduces homing of PC3 prostate cancer cells to human tissue-engineered bone *Cancers* **10** 438
[45] Holzapfel B M, Wagner F, Loessner D, Holzapfel N P, Thibaudeau L, Crawford R, Ling M-T, Clements J A, Russell P J and Hutmacher D W 2014 Species-specific homing mechanisms of human prostate cancer metastasis in tissue engineered bone *Biomaterials* **35** 4108-15
[46] Lescarbeau R M, Seib F P, Prewitz M, Werner C and Kaplan D L 2012 In vitro model of metastasis to bone marrow mediates prostate cancer castration resistant growth through paracrine and extracellular matrix factors *PloS one* **7**
[47] Antunes J, Gaspar V M, Ferreira L, Monteiro M, Henrique R, Jerónimo C and Mano J F 2019 In-air production of 3D co-culture tumor spheroid hydrogels for expedited drug screening *Acta biomaterialia* **94** 392-409
[48] Xu K, Ganapathy K, Andl T, Wang Z, Copland J A, Chakrabarti R and Florczyk S J 2019 3D porous chitosan-alginate scaffold stiffness promotes differential responses in prostate cancer cell lines *Biomaterials* **217** 119311

[49] Ambre A H, Katti K S and Katti D R 2010 Nanoclay Based Composite Scaffolds for Bone Tissue Engineering Applications *Journal of Nanotechnology in Engineering and Medicine* **1** 031013-9
[50] Ambre A H, Katti D R and Katti K S 2013 Nanoclays mediate stem cell differentiation and mineralized ECM formation on biopolymer scaffolds *Journal of Biomedical Materials Research Part A* **101** 2644-60
[51] Katti K S, Molla M D S, Karandish F, Haldar M K, Mallik S and Katti D R 2016 Sequential culture on biomimetic nanoclay scaffolds forms three-dimensional tumoroids *Journal of Biomedical Materials Research Part A* **104** 1591-602
[52] Molla M D S, Katti D R and Katti K S 2019 An in vitro model of prostate cancer bone metastasis for highly metastatic and non-metastatic prostate cancer using nanoclay bone-mimetic scaffolds *MRS Advances* **4** 1207-13
[53] Molla S, Katti D R and Katti K S 2018 In vitro design of mesenchymal to epithelial transition of prostate cancer metastasis using 3D nanoclay bone-mimetic scaffolds *Journal of Tissue Engineering and Regenerative Medicine* **12** 727-37
[54] Kar S, Katti D R and Katti K S 2019 Fourier transform infrared spectroscopy based spectral biomarkers of metastasized breast cancer progression *Spectrochimica Acta Part a-Molecular and Biomolecular Spectroscopy* **208** 85-96
[55] Kar S, Molla M D S, Katti D R and Katti K S 2019 Tissue-engineered nanoclay-based 3D in vitro breast cancer model for studying breast cancer metastasis to bone *Journal of tissue engineering and regenerative medicine* **13** 119-30
[56] Molla M D S, Katti D R, Iswara J, Venkatesan R, Paulmurugan R and Katti K S 2019 Prostate Cancer Phenotype Influences Bone Mineralization at Metastasis: A Study Using an In Vitro Prostate Cancer Metastasis Testbed *JBMR Plus* **n/a**
[57] Robling A G and Turner C H 2009 Mechanical signaling for bone modeling and remodeling *Critical reviews in eukaryotic gene expression* **19** 319
[58] Yu X, Botchwey E A, Levine E M, Pollack S R and Laurencin C T 2004 Bioreactor-based bone tissue engineering: the influence of dynamic flow on osteoblast phenotypic expression and matrix mineralization *Proceedings of the National Academy of Sciences* **101** 11203-8
[59] Santoro M, Lamhamedi-Cherradi S-E, Menegaz B A, Ludwig J A and Mikos A G 2015 Flow perfusion effects on three-dimensional culture and drug sensitivity of Ewing sarcoma *Proceedings of the National Academy of Sciences* **112** 10304-9
[60] Ambre A H, Katti D R and Katti K S 2015 Biomineralized hydroxyapatite nanoclay composite scaffolds with polycaprolactone for stem cell-based bone tissue engineering *Journal of Biomedical Materials Research Part A* **103** 2077-101
[61] Ambre A H, Katti K S and Katti D R 2010 Nanoclay based composite scaffolds for bone tissue engineering applications *Journal of Nanotechnology in Engineering and Medicine* **1**
[62] Katti K S, Ambre A H, Peterka N and Katti D R 2010 Use of unnatural amino acids for design of novel organomodified clays as components of nanocomposite biomaterials *Philosophical Transactions of the Royal Society A: Mathematical, Physical and Engineering Sciences* **368** 1963-80
[63] Goldstein A S, Juarez T M, Helmke C D, Gustin M C and Mikos A G 2001 Effect of convection on osteoblastic cell growth and function in biodegradable polymer foam scaffolds *Biomaterials* **22** 1279-88

[64] Hyler A R, Baudoin N C, Brown M S, Stremler M A, Cimini D, Davalos R V and Schmelz E M 2018 Fluid shear stress impacts ovarian cancer cell viability, subcellular organization, and promotes genomic instability *PLoS One* **13** e0194170
[65] Komori T 2002 Runx2, a multifunctional transcription factor in skeletal development *Journal of cellular biochemistry* **87** 1-8
[66] Komori T 2009 *Osteoimmunology*: Springer) pp 43-9
[67] Thibault R A, Scott Baggett L, Mikos A G and Kasper F K 2010 Osteogenic differentiation of mesenchymal stem cells on pregenerated extracellular matrix scaffolds in the absence of osteogenic cell culture supplements *Tissue Eng Part A* **16** 431-40
[68] Huang W, Yang S, Shao J and Li Y-P 2007 Signaling and transcriptional regulation in osteoblast commitment and differentiation *Frontiers in bioscience: a journal and virtual library* **12** 3068
[69] Penido M G M G and Alon U S 2012 Phosphate homeostasis and its role in bone health *Pediatric nephrology* **27** 2039-48
[70] Katti K S, Molla M D S, Karandish F, Haldar M K, Mallik S and Katti D R 2016 Sequential culture on biomimetic nanoclay scaffolds forms three-dimensional tumoroids *Journal of Biomedical Materials Research Part A* **104** 1591-602
[71] Chaffer C L, Brennan J P, Slavin J L, Blick T, Thompson E W and Williams E D 2006 Mesenchymal-to-epithelial transition facilitates bladder cancer metastasis: role of fibroblast growth factor receptor-2 *Cancer research* **66** 11271-8
[72] Yates C C, Shepard C R, Stolz D B and Wells A 2007 Co-culturing human prostate carcinoma cells with hepatocytes leads to increased expression of E-cadherin *British journal of cancer* **96** 1246-52
[73] Rubin M A, Mucci N R, Figurski J, Fecko A, Pienta K J and Day M L 2001 E-cadherin expression in prostate cancer: a broad survey using high-density tissue microarray technology *Human pathology* **32** 690-7
[74] Zaidel-Bar R, Kam Z and Geiger B 2005 Polarized downregulation of the paxillin-p130CAS-Rac1 pathway induced by shear flow *Journal of cell science* **118** 3997-4007
[75] Mertz A F, Che Y, Banerjee S, Goldstein J M, Rosowski K A, Revilla S F, Niessen C M, Marchetti M C, Dufresne E R and Horsley V 2013 Cadherin-based intercellular adhesions organize epithelial cell–matrix traction forces *Proceedings of the National Academy of Sciences* **110** 842-7
[76] Parsons J T 2003 Focal adhesion kinase: the first ten years *Journal of cell science* **116** 1409-16
[77] Sladkova M and De Peppo G M 2014 Bioreactor systems for human bone tissue engineering *Processes* **2** 494-525
[78] Mishra D K, Thrall M J, Baird B N, Ott H C, Blackmon S H, Kurie J M and Kim M P 2012 Human lung cancer cells grown on acellular rat lung matrix create perfusable tumor nodules *The Annals of thoracic surgery* **93** 1075-81
[79] Bartusik D, Tomanek B, Siluk D, Kaliszan R and Fallone G 2009 The application of 19F magnetic resonance ex vivo imaging of three-dimensional cultured breast cancer cells to study the effect of δ-tocopherol *Analytical biochemistry* **387** 315-7
[80] Trachtenberg J E, Santoro M, Williams Iii C, Piard C M, Smith B T, Placone J K, Menegaz B A, Molina E R, Lamhamedi-Cherradi S-E and Ludwig J A 2018 Effects of shear stress gradients on ewing sarcoma cells using 3D printed scaffolds and flow perfusion *ACS Biomaterials Science & Engineering* **4** 347-56

[81] Trouard T P, Harkins K D, Divijak J L, Gillies R J and Galons J P 2008 Ischemia-induced changes of intracellular water diffusion in rat glioma cell cultures *Magnetic Resonance in Medicine: An Official Journal of the International Society for Magnetic Resonance in Medicine* **60** 258-64
[82] Levesque M J and Nerem R M 1985 The elongation and orientation of cultured endothelial cells in response to shear stress
[83] Nettleship I 2014 *Tissue Engineering Using Ceramics and Polymers*: Elsevier) pp 224-51
[84] Massai D, Isu G, Madeddu D, Cerino G, Falco A, Frati C, Gallo D, Deriu M A, Labate G F D U and Quaini F 2016 A versatile bioreactor for dynamic suspension cell culture. Application to the culture of cancer cell spheroids *PloS one* **11**
[85] Sinlapabodin S, Amornsudthiwat P, Damrongsakkul S and Kanokpanont S 2016 An axial distribution of seeding, proliferation, and osteogenic differentiation of MC3T3-E1 cells and rat bone marrow-derived mesenchymal stem cells across a 3D Thai silk fibroin/gelatin/hydroxyapatite scaffold in a perfusion bioreactor *Materials Science and Engineering: C* **58** 960-70
[86] Sikavitsas V I, Bancroft G N, Lemoine J J, Liebschner M A K, Dauner M and Mikos A G 2005 Flow perfusion enhances the calcified matrix deposition of marrow stromal cells in biodegradable nonwoven fiber mesh scaffolds *Annals of biomedical engineering* **33** 63-70
[87] Fröhlich M, Grayson W L, Marolt D, Gimble J M, Kregar-Velikonja N and Vunjak-Novakovic G 2010 Bone grafts engineered from human adipose-derived stem cells in perfusion bioreactor culture *Tissue Engineering Part A* **16** 179-89
[88] Grayson W L, Marolt D, Bhumiratana S, Fröhlich M, Guo X E and Vunjak-Novakovic G 2011 Optimizing the medium perfusion rate in bone tissue engineering bioreactors *Biotechnology and bioengineering* **108** 1159-70
[89] Bancroft G N, Sikavitsas V I, van den Dolder J, Sheffield T L, Ambrose C G, Jansen J A and Mikos A G 2002 Fluid flow increases mineralized matrix deposition in 3D perfusion culture of marrow stromal osteoblasts in a dose-dependent manner *Proceedings of the National Academy of Sciences* **99** 12600-5
[90] McCoy R J, Jungreuthmayer C and O'Brien F J 2012 Influence of flow rate and scaffold pore size on cell behavior during mechanical stimulation in a flow perfusion bioreactor *Biotechnology and bioengineering* **109** 1583-94
[91] Hillsley M V and Frangos J A 1994 Bone tissue engineering: the role of interstitial fluid flow *Biotechnology and bioengineering* **43** 573-81
[92] Mishra A, Shiozawa Y, Pienta K J and Taichman R S 2011 Homing of cancer cells to the bone *Cancer Microenvironment* **4** 221-35
[93] Wang J, Shiozawa Y, Wang J, Wang Y, Jung Y, Pienta K J, Mehra R, Loberg R and Taichman R S 2008 The role of CXCR7/RDC1 as a chemokine receptor for CXCL12/SDF-1 in prostate cancer *Journal of Biological Chemistry* **283** 4283-94
[94] Bjerre L, Bünger C E, Kassem M and Mygind T 2008 Flow perfusion culture of human mesenchymal stem cells on silicate-substituted tricalcium phosphate scaffolds *Biomaterials* **29** 2616-27
[95] Stiehler M, Bunger C, Baatrup A, Lind M, Kassem M and Mygind T 2009 Effect of dynamic 3-D culture on proliferation, distribution, and osteogenic differentiation of human mesenchymal stem cells *J Biomed Mater Res A* **89** 96-107

[96] Beşkardeş I G, Aydın G, Bektaş Ş, Cengiz A and Gümüşderelioğlu M 2018 A systematic study for optimal cell seeding and culture conditions in a perfusion mode bone-tissue bioreactor *Biochemical engineering journal* **132** 100-11
[97] Riehl B D, Lee J S, Ha L and Lim J Y 2015 Fluid-flow-induced mesenchymal stem cell migration: role of focal adhesion kinase and RhoA kinase sensors *Journal of the Royal Society Interface* **12** 20141351
[98] Moses J C, Nandi S K and Mandal B B 2018 Multifunctional cell instructive silk-bioactive glass composite reinforced scaffolds toward osteoinductive, proangiogenic, and resorbable bone grafts *Advanced healthcare materials* **7** 1701418
[99] Malandrino A, Kamm R D and Moeendarbary E 2018 In vitro modeling of mechanics in cancer metastasis *ACS biomaterials science & engineering* **4** 294-301
[100] Kowalski P J, Rubin M A and Kleer C G 2003 E-cadherin expression in primary carcinomas of the breast and its distant metastases *Breast cancer research* **5** R217
[101] Tsai J and Kam L 2009 Rigidity-dependent cross talk between integrin and cadherin signaling *Biophysical Journal* **96** L39-L41
[102] McCain M L, Lee H, Aratyn-Schaus Y, Kléber A G and Parker K K 2012 Cooperative coupling of cell-matrix and cell–cell adhesions in cardiac muscle *Proceedings of the National Academy of Sciences* **109** 9881-6
[103] Weber G F, Bjerke M A and DeSimone D W 2011 Integrins and cadherins join forces to form adhesive networks *Journal of cell science* **124** 1183-93
[104] Tseng Q, Duchemin-Pelletier E, Deshiere A, Balland M, Guillou H, Filhol O and Théry M 2012 Spatial organization of the extracellular matrix regulates cell–cell junction positioning *Proceedings of the National Academy of Sciences* **109** 1506-11
[105] Martinez-Rico C, Pincet F, Thiery J-P and Dufour S 2010 Integrins stimulate E-cadherin-mediated intercellular adhesion by regulating Src-kinase activation and actomyosin contractility *Journal of cell science* **123** 712-22
[106] Alt-Holland A, Sowalsky A G, Szwec-Levin Y, Shamis Y, Hatch H, Feig L A and Garlick J A 2011 Suppression of E-cadherin function drives the early stages of Ras-induced squamous cell carcinoma through upregulation of FAK and Src *Journal of Investigative Dermatology* **131** 2306-15
[107] Pei G, Lan Y, Chen D, Ji L and Hua Z-c 2017 FAK regulates E-cadherin expression via p-SrcY416/p-ERK1/2/p-Stat3Y705 and PPARγ/miR-125b/Stat3 signaling pathway in B16F10 melanoma cells *Oncotarget* **8** 13898
[108] Taliaferro-Smith L, Oberlick E, Liu T, McGlothen T, Alcaide T, Tobin R, Donnelly S, Commander R, Kline E and Nagaraju G P 2015 FAK activation is required for IGF1R-mediated regulation of EMT, migration, and invasion in mesenchymal triple negative breast cancer cells *Oncotarget* **6** 4757
[109] Tai Y-L, Chen L-C and Shen T-L 2015 Emerging roles of focal adhesion kinase in cancer *BioMed research international* **2015**
[110] Hsia D A, Mitra S K, Hauck C R, Streblow D N, Nelson J A, Ilic D, Huang S, Li E, Nemerow G R and Leng J 2003 Differential regulation of cell motility and invasion by FAK *The Journal of cell biology* **160** 753-67
[111] Owens L V, Xu L, Dent G A, Yang X, Sturge G C, Craven R J and Cance W G 1996 Focal adhesion kinase as a marker of invasive potential in differentiated human thyroid cancer *Annals of Surgical Oncology* **3** 100-5

[112] Golubovskaya V M, Ylagan L, Miller A, Hughes M, Wilson J, Wang D, Brese E, Bshara W, Edge S and Morrison C 2014 High focal adhesion kinase expression in breast carcinoma is associated with lymphovascular invasion and triple-negative phenotype *BMC cancer* **14** 769
[113] Aboubakar Nana F, Hoton D, Ambroise J, Lecocq M, Vanderputten M, Sibille Y, Vanaudenaerde B, Pilette C, Bouzin C and Ocak S 2019 Increased Expression and Activation of FAK in Small-Cell Lung Cancer Compared to Non-Small-Cell Lung Cancer *Cancers* **11** 1526
[114] Frame M C, Patel H, Serrels B, Lietha D and Eck M J 2010 The FERM domain: organizing the structure and function of FAK *Nature reviews Molecular cell biology* **11** 802-14
[115] Sun J, Luo Q, Liu L and Song G 2018 Low-level shear stress promotes migration of liver cancer stem cells via the FAK-ERK1/2 signalling pathway *Cancer letters* **427** 1-8
[116] Pan M-R, Hou M-F, Ou-Yang F, Wu C-C, Chang S-J, Hung W-C, Yip H-K and Luo C-W 2019 FAK is required for tumor metastasis-related fluid microenvironment in triple-negative breast cancer *Journal of clinical medicine* **8** 38
[117] Katti K S, Jasuja H, Kar S and Katti D R 2020 Nanostructured biomaterials for in vitro models of bone metastasis cancer *Current Opinion in Biomedical Engineering* 100254
[118] Fischbach C, Chen R, Matsumoto T, Schmelzle T, Brugge J S, Polverini P J and Mooney D J 2007 Engineering tumors with 3D scaffolds *Nature methods* **4** 855-60
[119] Molla M D S, Katti D R, Iswara J, Venkatesan R, Paulmurugan R and Katti K S 2020 Prostate cancer phenotype influences bone mineralization at metastasis: a study using an in vitro prostate cancer metastasis testbed *JBMR plus* **4** e10256
[120] Molla M D S, Katti D R and Katti K S 2018 In vitro design of mesenchymal to epithelial transition of prostate cancer metastasis using 3D nanoclay bone-mimetic scaffolds *Journal of tissue engineering and regenerative medicine* **12** 727-37
[121] Jasuja H, Kar S, Katti D R and Katti K S 2021 Perfusion bioreactor enabled fluid-derived shear stress conditions for novel bone metastatic prostate cancer testbed *Biofabrication* **13** 035004
[122] Shin Y, Han S, Jeon J S, Yamamoto K, Zervantonakis I K, Sudo R, Kamm R D and Chung S 2012 Microfluidic assay for simultaneous culture of multiple cell types on surfaces or within hydrogels *Nature protocols* **7** 1247-59
[123] Zhang Q, Liu T and Qin J 2012 A microfluidic-based device for study of transendothelial invasion of tumor aggregates in realtime *Lab on a chip* **12** 2837-42
[124] Marturano-Kruik A, Nava M M, Yeager K, Chramiec A, Hao L, Robinson S, Guo E, Raimondi M T and Vunjak-Novakovic G 2018 Human bone perivascular niche-on-a-chip for studying metastatic colonization *Proceedings of the National Academy of Sciences* **115** 1256-61
[125] Hajal C, Ibrahim L, Serrano J C, Offeddu G S and Kamm R D 2021 The effects of luminal and trans-endothelial fluid flows on the extravasation and tissue invasion of tumor cells in a 3D in vitro microvascular platform *Biomaterials* **265** 120470
[126] Hendrix M J, Seftor E A, Seftor R E and Fidler I J 1987 A simple quantitative assay for studying the invasive potential of high and low human metastatic variants *Cancer letters* **38** 137-47
[127] Sobachkin A and Dumnov G 2013 Numerical basis of CAD-embedded CFD. In: *NAFEMS World Congress*, pp 9-12

[128] Katti K S, Ambre A H, Payne S and Katti D R 2015 Vesicular delivery of crystalline calcium minerals to ECM in biomineralized nanoclay composites *Materials Research Express* **2** 045401
[129] Ramesh S, Wildey G M and Howe P H 2009 Transforming growth factor β (TGFβ)-induced apoptosis: the rise and fall of Bim *Cell Cycle* **8** 11-7
[130] Wakefield L M and Roberts A B 2002 TGF-β signaling: positive and negative effects on tumorigenesis *Current opinion in genetics & development* **12** 22-9
[131] Urbich C, Walter D H, Zeiher A M and Dimmeler S 2000 Laminar shear stress upregulates integrin expression: role in endothelial cell adhesion and apoptosis *Circulation research* **87** 683-9
[132] Chen K-D, Li Y-S, Kim M, Li S, Yuan S, Chien S and Shyy J Y 1999 Mechanotransduction in response to shear stress: roles of receptor tyrosine kinases, integrins, and Shc *Journal of Biological Chemistry* **274** 18393-400
[133] Zhao F, Li L, Guan L, Yang H, Wu C and Liu Y 2014 Roles for GP IIb/IIIa and αvβ3 integrins in MDA-MB-231 cell invasion and shear flow-induced cancer cell mechanotransduction *Cancer letters* **344** 62-73
[134] Chinni S R, Sivalogan S, Dong Z, Filho J C T, Deng X, Bonfil R D and Cher M L 2006 CXCL12/CXCR4 signaling activates Akt-1 and MMP-9 expression in prostate cancer cells: the role of bone microenvironment-associated CXCL12 *The Prostate* **66** 32-48
[135] Conley-LaComb M K, Semaan L, Singareddy R, Li Y, Heath E I, Kim S, Cher M L and Chinni S R 2016 Pharmacological targeting of CXCL12/CXCR4 signaling in prostate cancer bone metastasis *Molecular cancer* **15** 1-13
[136] Sun Y X, Wang J, Shelburne C E, Lopatin D E, Chinnaiyan A M, Rubin M A, Pienta K J and Taichman R S 2003 Expression of CXCR4 and CXCL12 (SDF-1) in human prostate cancers (PCa) in vivo *Journal of cellular biochemistry* **89** 462-73
[137] Neel J-C, Humbert L and Lebrun J-J 2012 The dual role of TGFβ in human cancer: from tumor suppression to cancer metastasis *International Scholarly Research Notices* **2012**
[138] Ohgushi M, Kuroki S, Fukamachi H, O'Reilly L A, Kuida K, Strasser A and Yonehara S 2005 Transforming growth factor β-dependent sequential activation of Smad, Bim, and caspase-9 mediates physiological apoptosis in gastric epithelial cells *Molecular and cellular biology* **25** 10017-28
[139] Motyl T, Grzelkowska K, Zimowska W, Skierski J, Waręski P, Płoszaj T and Trzeciak L 1998 Expression of bcl-2 and bax in TGF-β1-induced apoptosis of L1210 leukemic cells *European journal of cell biology* **75** 367-74
[140] Chen R-H, Su Y-H, Chuang R L and Chang T-Y 1998 Suppression of transforming growth factor-β-induced apoptosis through a phosphatidylinositol 3-kinase/Akt-dependent pathway *Oncogene* **17** 1959-68
[141] Song K, Wang H, Krebs T L and Danielpour D 2006 Novel roles of Akt and mTOR in suppressing TGF-β/ALK5-mediated Smad3 activation *The EMBO journal* **25** 58-69
[142] Zheng D-Q, Woodard A S, Tallini G and Languino L R 2000 Substrate specificity of αvβ3integrin-mediated cell migration and phosphatidylinositol 3-kinase/AKT pathway activation *Journal of Biological Chemistry* **275** 24565-74
[143] Zheng D-Q, Woodard A S, Fornaro M, Tallini G and Languino L R 1999 Prostatic carcinoma cell migration via αvβ3integrin is modulated by a focal adhesion kinase pathway *Cancer research* **59** 1655-64

[144] Sun X, Cheng G, Hao M, Zheng J, Zhou X, Zhang J, Taichman R S, Pienta K J and Wang J 2010 CXCL12/CXCR4/CXCR7 chemokine axis and cancer progression *Cancer and Metastasis Reviews* **29** 709-22
[145] Shah A D, Bouchard M J and Shieh A C 2015 Interstitial fluid flow increases hepatocellular carcinoma cell invasion through CXCR4/CXCL12 and MEK/ERK signaling *PLoS One* **10** e0142337
[146] Kennecke H, Yerushalmi R, Woods R, Cheang M C U, Voduc D, Speers C H, Nielsen T O and Gelmon K 2010 Metastatic behavior of breast cancer subtypes *Journal of clinical oncology* **28** 3271-7
[147] Heppner G H and Miller B E 1983 Tumor heterogeneity: biological implications and therapeutic consequences *Cancer and Metastasis Reviews* **2** 5-23
[148] Hay M, Thomas D W, Craighead J L, Economides C and Rosenthal J 2014 Clinical development success rates for investigational drugs *Nature biotechnology* **32** 40-51
[149] Pampaloni F, Reynaud E G and Stelzer E H 2007 The third dimension bridges the gap between cell culture and live tissue *Nature reviews Molecular cell biology* **8** 839-45
[150] Langhans S A 2018 Three-dimensional in vitro cell culture models in drug discovery and drug repositioning *Frontiers in pharmacology* **9** 6
[151] Holliday D L and Speirs V 2011 Choosing the right cell line for breast cancer research *Breast cancer research* **13** 1-7
[152] Kondo J, Endo H, Okuyama H, Ishikawa O, Iishi H, Tsujii M, Ohue M and Inoue M 2011 Retaining cell–cell contact enables preparation and culture of spheroids composed of pure primary cancer cells from colorectal cancer *Proceedings of the National Academy of Sciences* **108** 6235-40
[153] Kar S, Jasuja H, Katti D R and Katti K S 2019 Wnt/β-Catenin Signaling Pathway Regulates Osteogenesis for Breast Cancer Bone Metastasis: Experiments in an In Vitro Nanoclay Scaffold Cancer Testbed *ACS Biomaterials Science & Engineering* **6** 2600-11
[154] Shao M-M, Chan S K, Alex M, Lam C C, Tsang J Y, Lui P C, Law B K, Tan P-H and Gary M T 2012 Keratin expression in breast cancers *Virchows Archiv* **461** 313-22
[155] Fujisue M, Nishimura R, Okumura Y, Tashima R, Nishiyama Y, Osako T, Toyozumi Y and Arima N 2013 Clinical significance of CK19 negative breast cancer *Cancers* **5** 1-11
[156] Parikh R R, Yang Q, Higgins S A and Haffty B G 2008 Outcomes in young women with breast cancer of triple-negative phenotype: the prognostic significance of CK19 expression *International Journal of Radiation Oncology* Biology* Physics* **70** 35-42
[157] Roche J 2018 The epithelial-to-mesenchymal transition in cancer. Multidisciplinary Digital Publishing Institute)
[158] Hirano S, Nose A, Hatta K, Kawakami A and Takeichi M 1987 Calcium-dependent cell-cell adhesion molecules (cadherins): subclass specificities and possible involvement of actin bundles *The Journal of cell biology* **105** 2501-10
[159] McDonald S and Silver A 2009 The opposing roles of Wnt-5a in cancer *British journal of cancer* **101** 209-14
[160] Zhong Z, Shan M, Wang J, Liu T, Shi Q and Pang D 2016 Decreased Wnt5a expression is a poor prognostic factor in triple-negative breast cancer *Medical science monitor: international medical journal of experimental and clinical research* **22** 1
[161] Leris A, Roberts T, Jiang W G, Newbold R and Mokbel K 2005 WNT5A expression in human breast cancer *Anticancer research* **25** 731-4

[162] Wang Z, Zhang H, Hou J, Niu J, Ma Z, Zhao H and Liu C 2015 Clinical implications of β-catenin protein expression in breast cancer *International journal of clinical and experimental pathology* **8** 14989
[163] Li S, Li S, Sun Y and Li L 2014 The expression of β-catenin in different subtypes of breast cancer and its clinical significance *Tumor Biology* **35** 7693-8
[164] Aldridge S, Lennard T, Williams J and Birch M 2005 Vascular endothelial growth factor receptors in osteoclast differentiation and function *Biochemical and biophysical research communications* **335** 793-8
[165] Osta W A, Chen Y, Mikhitarian K, Mitas M, Salem M, Hannun Y A, Cole D J and Gillanders W E 2004 EpCAM is overexpressed in breast cancer and is a potential target for breast cancer gene therapy *Cancer research* **64** 5818-24
[166] Guise T A, Yin J J and Mohammad K S 2003 Role of endothelin-1 in osteoblastic bone metastases *Cancer: Interdisciplinary International Journal of the American Cancer Society* **97** 779-84
[167] Bu G, Lu W, Liu C C, Selander K, Yoneda T, Hall C, Keller E T and Li Y 2008 Breast cancer-derived Dickkopf1 inhibits osteoblast differentiation and osteoprotegerin expression: implication for breast cancer osteolytic bone metastases *International journal of cancer* **123** 1034-42
[168] Voorzanger-Rousselot N, Goehrig D, Journe F, Doriath V, Body J-J, Clézardin P and Garnero P 2007 Increased Dickkopf-1 expression in breast cancer bone metastases *British journal of cancer* **97** 964-70
[169] Pathi S P, Kowalczewski C, Tadipatri R and Fischbach C 2010 A novel 3-D mineralized tumor model to study breast cancer bone metastasis *PLoS One* **5** e8849
[170] Balachander G M, Balaji S A, Rangarajan A and Chatterjee K 2015 Enhanced metastatic potential in a 3D tissue scaffold toward a comprehensive in vitro model for breast cancer metastasis *ACS applied materials & interfaces* **7** 27810-22
[171] Chao Y L, Shepard C R and Wells A 2010 Breast carcinoma cells re-express E-cadherin during mesenchymal to epithelial reverting transition *Molecular cancer* **9** 1-18
[172] Chen Y, Whetstone H C, Lin A C, Nadesan P, Wei Q, Poon R and Alman B A 2007 Beta-catenin signaling plays a disparate role in different phases of fracture repair: implications for therapy to improve bone healing *PLoS medicine* **4** e249
[173] Bain G, Müller T, Wang X and Papkoff J 2003 Activated β-catenin induces osteoblast differentiation of C3H10T1/2 cells and participates in BMP2 mediated signal transduction *Biochemical and biophysical research communications* **301** 84-91
[174] Clines K L and Clines G A 2018 DKK1 and Kremen expression predicts the osteoblastic response to bone metastasis *Translational oncology* **11** 873-82
[175] Chen Y and Alman B A 2009 Wnt pathway, an essential role in bone regeneration *Journal of cellular biochemistry* **106** 353-62
[176] Chen Y, Shi H Y, Stock S R, Stern P H and Zhang M 2011 Regulation of breast cancer-induced bone lesions by β-catenin protein signaling *Journal of Biological Chemistry* **286** 42575-84
[177] Cartmell S H, Porter B D, García A J and Guldberg R E 2003 Effects of medium perfusion rate on cell-seeded three-dimensional bone constructs in vitro *Tissue engineering* **9** 1197-203